5-2023

PDA/PTFE Solid Lubricant Coating for 60NiTi Applications

Charles Richey Miller
University of Arkansas, Fayetteville

PDA/PTFE Solid Lubricant Coating for 60NiTi Applications

A dissertation submitted in partial fulfillment
of the requirements for the degree of
Doctor of Philosophy in Engineering

by

Charles Miller
University of Arkansas
Bachelor of Science in Mechanical Engineering, 2017

May 2023
University of Arkansas

This dissertation is approved for recommendation to the Graduate Council.

_____
Min Zou, Ph.D.
Dissertation Director

_____
Jingyi Chen, Ph.D.
Committee Member

_____
David Huitink, Ph.D.
Committee Member

_____
Xiangbo Meng, Ph.D.
Committee Member

_____
Arun Nair, Ph.D.
Committee Member

_____
Feng Wang, Ph.D.
Committee Member

ABSTRACT

The intermetallic alloy 60NiTi has a unique combination of high hardness and low elastic modulus, which makes it highly resistant to dents. Additionally, 60NiTi is extremely corrosion resistant and chemically inert. These properties make 60NiTi a desirable material for challenging mechanical component applications with high contact stresses and in harsh environments. However, lubrication issues have hindered the use of 60NiTi because it has poor tribological performance if it is not properly lubricated.

The mechanical properties of hardened 60NiTi and its microconstituents were studied by nanoindentation. This study showed that the bulk properties of 60NiTi are driven by the properties of the NiTi + Ni_4Ti_3 region. The large Ni_3Ti precipitates were found to have significantly higher hardness. This discovery inspired new theories for the wear behavior of 60NiTi.

Despite its high hardness and extraordinary hardness-to-elasticity ratio, 60NiTi has poor tribological performance in unlubricated sliding. Since oil-based lubrication cannot be used in many applications, there is need for a suitable solid lubricant coating that can be applied to 60NiTi. A polytetrafluoroethylene (PTFE)-based solid lubricant coating that uses a polydopamine (PDA) adhesive underlayer was developed and evaluated for use on 60NiTi.

PDA/PTFE coating was evaluated on 60NiTi substrate by linear-reciprocating wear tests against a Si_3N_4 ball. The coating reduced friction and protected the substrate surface from adhesive and abrasive wear during accelerated testing. The durability of the coating was

drastically improved by grinding and polishing the substrate surface to produce a valley-dominant surface. The valleys of the substrate surface provided mechanical interlocking of the PDA/PTFE coating.

Nanoindenter scratch tests and scanning electron microscopy imaging of the scratches provided a detailed understanding of the microstructural behavior and failure mechanisms of the coating. Additionally, incorporating graphite particles in the PTFE layer was shown to further enhance the coating performance. The coating was found to compact under repetitious sliding under normal loads to form a less-porous structure with enhanced cohesion. The valley-dominant substrate surface reduced tensile stresses in the coating, and the graphite particles added to the PTFE layer enhanced the coating cohesion. The combined effect was better resistance to coating tears that could lead to global coating delamination.

Lastly, methods were developed to apply and test the PDA/PTFE coating as a ball bearing lubricant. A custom bearing tester was designed and built to study the effectiveness of the coating in ball bearing applications. The balls and races of hybrid R8 bearings were coated with PDA/PTFE or PDA/PTFE+GPs, and the bearing tests showed promising results.

This work advanced the understanding of the unique mechanical properties of 60NiTi and developed PDA/PTFE solid lubricant coatings that are suitable solid lubricants for 60NiTi. Additionally, the microstructural behavior and failure mechanisms of PDA/PTFE-based coatings are better understood. The results are promising solutions for lubricating 60NiTi in challenging mechanical component applications.

ACKNOWLEDGEMENTS

Thank you to my faculty advisor and mentor, Dr. Min Zou. It was a true privilege to work for her and to be part of the Nanomechanics and Tribology Lab (NMTL) that she directs. She shared invaluable knowledge, experience, and feedback with me. The way that she leads, supports, and manages her team enables a thriving environment for research, which was instrumental in my personal and professional development. She was a constant guide and support throughout my graduate studies, and she set an incredible example to aspire to.

Thank you to my advising committee, Dr. Jingyi Chen, Dr. David Huitink, Dr. Xiangbo Meng, Dr. Arun Nair, and Dr. Feng Wang. The feedback and expertise that they provided was extremely helpful. I am grateful for each committee members' specialized knowledge and skills. Their wealth and diversity of knowledge taught me to view research problems from various perspectives.

Thank you to my technical contacts and collaborators, Dr. Christopher DellaCorte, Dr. Adam Howard, Dr. Brad Miller, and Dr. Feng Wang for the knowledge and guidance that they shared. It was extremely helpful to learn from their work and to receive their feedback.

Thank you to my co-workers throughout my time with the NMTL, Adedoyin Abe, Raissa Araujo Borges, Dr. Dipankar Choudhury, Dr. Sujan Ghosh, Josh Goss, Nathan Harris, Julia Hoskins, Firuze Soltani-Kordshuli, Dr. Shelby Maddox, Dr. Mahyar Afshar-Mohajer, Colin Phelan, Steven Sonntag, and Jason Steck. It was a joy to work with and learn from them.

Thank you to my parents, Michele and Richey Miller, for the love and support they provided for over 20 years of education. They taught me to love others and work passionately. They have always encouraged me to pursue my countless interests. To my sisters, Bethany and Kailey, thank you for your love and friendship. It has been inspirational to watch each of them pursue excellence in their respective fields.

Lastly, and most of all, thank you to my wife, Valeria. The love, care, and encouragement that she provided throughout my doctoral studies were tremendous blessings. She brings light and joy to my life, and I am forever grateful for her.

TABLE OF CONTENTS

LIST OF TABLES

LIST OF FIGURES

LIST OF PUBLISHED PAPERS

C. Miller, C. DellaCorte, and M. Zou, "Nanomechanical properties of hardened 60NiTi," *Materials Science and Engineering: A*, vol. 800, p. 140284, 2021. (Included as Chapter 2 of this dissertation)

C. Miller, D. Choudhury, and M. Zou, "The Effects of surface roughness on the durability of polydopamine/PTFE solid lubricant coatings on NiTiNOL 60," *Tribology Transactions*, vol. 62, no. 5, pp. 919–929, 2019. (Included as Chapter 3 of this dissertation)

C. Miller and M. Zou, "Microscale friction and deformation behavior of polydopamine/polytetrafluoroethylene-coated 60NiTi from nanoscratch tests," *Thin Solid Films*, vol. 743, p. 139079, 2022. (Included as Chapter 4 of this dissertation)

C. Miller and M. Zou, "Repetitive nanoindenter scratch testing of polydopamine/polytetrafluoroethylene-based thin coatings," *Surf Coat Technol*, vol. 451, p. 129042, 2022. (Included as Chapter 5 of this dissertation)

CHAPTER 1

INTRODUCTION

Disclaimer

Portions of this chapter were previously published as:

C. Miller, C. DellaCorte, and M. Zou, "Nanomechanical properties of hardened 60NiTi," *Materials Science and Engineering: A*, vol. 800, p. 140284, 2021.

C. Miller, D. Choudhury, and M. Zou, "The Effects of surface roughness on the durability of polydopamine/PTFE solid lubricant coatings on NiTiNOL 60," *Tribology Transactions*, vol. 62, no. 5, pp. 919–929, 2019.

C. Miller and M. Zou, "Microscale friction and deformation behavior of polydopamine/polytetrafluoroethylene-coated 60NiTi from nanoscratch tests," *Thin Solid Films*, vol. 743, p. 139079, 2022.

C. Miller and M. Zou, "Repetitive nanoindenter scratch testing of polydopamine/polytetrafluoroethylene-based thin coatings," *Surf Coat Technol*, vol. 451, p. 129042, 2022.

NiTiNOL 60, or 60NiTi, is a prime candidate material for demanding mechanical component applications due to its unique properties [1]. This intermetallic alloy has high hardness yet low elastic modulus, which enables it to sustain heavy loads without permanent deformation [2–4]. Additionally, 60NiTi is nearly corrosion-proof, and it is chemically inert, electrically conductive, and non-magnetic [5–6]. This combination of properties has attracted substantial attention to 60NiTi as a candidate bearing and gear material for components operating in harsh environments such as the distillation assembly of the water recovery system on the International Space Station [1,5,7]. However, in unlubricated contact, 60NiTi exhibits a high coefficient of friction (COF) and high wear rate due to adhesive and abrasive wear mechanisms [2,6]. 60NiTi has been shown to respond well to oil-lubrication [8], but the use of

liquid lubricants may be precluded by operating conditions with high temperature, vacuum, or contamination risks [9]. In such cases, polytetrafluoroethylene (PTFE) can be applied as a solid lubricant coating, and polydopamine (PDA) can be used as an adhesive layer for the coating [10–12]. 60NiTi coated with a PDA adhesive layer and a thin PTFE solid lubricant coating is denoted as 60NiTi/PDA/PTFE. This dissertation pursues the application of 60NiTi/PDA/PTFE by studying the mechanical and tribological behavior of 60NiTi, applying and evaluating PDA/PTFE as a solid lubricant coating on 60NiTi, improving the coating performance by modifying the substrate roughness and incorporating graphite particles to the PTFE layer, and applying and testing PDA/PTFE coating on ball bearings.

1.1 Objective and Scope

The objective of this dissertation is to further the understanding of the tribological behavior and mechanical properties of 60NiTi and to develop PTFE-based solid lubricant coatings for use with 60NiTi in bearing and gear applications. This introductory chapter (Chapter 1) serves to define the problem, provide background information and a review of the relevant literature, and layout the research that was performed. Chapters 2-5 are a compilation of four peer-reviewed articles that were published in pursuit of the main objective. These chapters address the specific goals to:

- Further the understanding of the tribological behavior and mechanical properties of 60NiTi through nanoindentation (Chapter 2)
- Develop procedures for coating 60NiTi with PDA/PTFE solid lubricant and analyze the effects of substrate surface roughness on coating durability (Chapter 3)

- Analyze the microscale friction and deformation behavior of 60NiTi/PDA/PTFE through nanoindenter scratch testing at various loads (Chapter 4)
- Explain the remarkably enhanced performance of 60NiTi/PDA/PTFE coatings when the substrate is rough and graphite particles are added to the PTFE layer (Chapter 5)

These four articles are compiled in this dissertation because while they function independently to address the specific goals bulleted above, collaboratively, they combine to satisfy the overarching objective of this work. Additionally, the variety of equipment and methods used across these articles makes it favorable for this information to be discussed specifically in each chapter.

A particular application of interest for 60NiTi/PDA/PTFE is for ball bearings in the Water Recovery System of the International Space Station. However, there are no existing reports of PDA/PTFE being applied to ball bearings. Chapter 6 presents methods that were developed to deposit PDA/PTFE coating on ball bearing components and a custom-built bearing tester that was designed, built, and used to assess the effectiveness of PDA/PTFE-coated ball bearings. Although this work is ongoing, the current progress was included in this dissertation because it reinforces the significance of the developments from Chapters 2-5 and it has great importance for the recommended future work. The recommendations for future work follow concluding remarks that summarize the entire dissertation in Chapter 7.

1.2 Background and Literature Review

1.2.1 60NiTi

Nickel-titanium alloys were first developed by W.J. Buehler in the Naval Ordinance Laboratory (NOL) in the 1950s, hence the name NiTiNOL (Ni-Ti NOL) [13–14]. Neither metal nor ceramic, NiTiNOL 60, or 60NiTi (60 wt % Ni, 40 wt % Ti), is a weakly ordered intermetallic compound with peculiar properties compared to traditional engineering materials. 60NiTi exhibits a unique combination of high hardness and low Young's modulus [4,6,15–17]. The material can be heat treated to reach a hardness of 56 to 62 on the Rockwell C scale while maintaining a low Young's Modulus around 90 GPa [3,18–22]. These characteristics, alongside being corrosion resistant, chemically inert, electrically conductive, and non-magnetic, make 60NiTi an enticing candidate for bearing applications [5,7–8,23–26]. The high hardness inhibits dents from forming and the low modulus reduces the contact pressure compared to traditional bearing materials. However, after its development, difficulties in machining and working with 60NiTi largely prevented its adoption for mechanical components [15].

In the last few decades, advancements in the manufacturing and processing of 60NiTi have reinvigorated the interest in this material. Powder metallurgy enables near net-shape parts to be produced and ceramic cutting tools and electrode discharge machining (EDM) allow 60NiTi to be processed more easily [15].

The manufacturing and processing advancements of 60NiTi have prompted interest from the National Aeronautics and Space Administration (NASA) in utilizing 60NiTi for material problems in critical applications [3]. For example, 60NiTi bearings are being developed to

replace bearings that experience corrosion and wear issues in the water recovery system of the International Space Station [5]. To pursue these applications, NASA has performed extensive studies of the loadbearing, tribological, and time-temperature-transition (TTT) behavior of 60NiTi [4,19,22,27–31].

60NiTi has been shown to achieve the highest hardness among the binary NiTi compounds after heat treatment at 1050 °C [22]. The high hardness is caused by precipitation hardening through the rapid formation of nanoscale Ni_4Ti_3 precipitates upon cooling from a solution-annealed condition. The Ni_4Ti_3 phase is metastable and will eventually decompose to larger, Ni-rich phases if the alloy is not quenched after being solutionized [15]. Without proper quenching, a significant drop in hardness will occur from the precipitation of the metastable Ni_3Ti_2 and stable Ni_3Ti phases [27].

The hardening behavior of 60NiTi has been studied using Vickers and Rockwell hardness testers and mechanical testing systems [1–3,21,24,32]. Stanford et. al used Vickers microindentation hardness testing to evaluate the hardness of twenty-six binary and ternary NiTiNOL compounds that underwent various heat treatment processes [21]. They also characterized the second phase vol % that developed in these compounds after heat treatment. Neupane et al. used a multi-function tribometer/nano-mechanical system to indent 60NiTi with a Berkovich indenter at a load range from 40-450 mN [2]. However, the existing literature lacks a study of the load-displacement behavior of 60NiTi in the μN to mN load range and with displacements on the order of nanometers, which is important for understanding the elastic behavior of 60NiTi in addition to its hardness.

In addition to the mechanical property and microstructure characterizations of 60NiTi, the tribological behavior of this material has been a recent area of research interest. The high hardness to elasticity ratio for 60NiTi suggests that it should exhibit high wear resistance [33]. However, 60NiTi has been observed to have poor tribological performance in unlubricated contact. Under these conditions, 60NiTi has a high COF (0.7–1.0) and a wear rate up to two orders of magnitude greater than that of 440C, a type of stainless steel of similar hardness [30]. The high wear rate of 60NiTi is caused by abrasive wear, adhesive wear, and the propagation of microcracks due to shear stresses from sliding. These cracks lead to the fracture and removal of 60NiTi materials [2,6,30]. Additionally, the COF of 60NiTi is typically high. Therefore, proper lubrication is necessary for 60NiTi to function well in tribological applications, and applications of interest require the development of a suitable solid lubricant coating [1,11,12,16].

1.2.2 PDA/PTFE

PTFE has many desirable properties such as low COF, high temperature resistance, and chemical resistance, which lead to its use as a solid lubricant in many tribological applications [34]. It is a compatible lubricant for 60NiTi [1]. However, PTFE thin coatings have high wear rates and low adhesion to most substrate materials. To combat the weaknesses of PTFE thin films as solid lubricant coatings, a bio-inspired PDA thin film was developed for use as an adhesive underlayer between PTFE and various substrate materials [35]. PDA is a biomimetic polymer proposed by Lee et al. as a surface modifier that allows further functionalization of a surface [36]. It is inspired by the adhesive proteins that sea mussels secrete to attach themselves to countless surfaces, including PTFE. The driving force of PDA-formation is oxidative polymerization of dopamine [37]. PDA adheres to various substrates through multiple

noncovalent interactions [38]. However, the interactions between PDA and PTFE are unknown, and determining the specific binding mechanisms between PDA and various substrates is an ongoing field of study.

Beckford et al. first used a PDA adhesive underlayer to adhere thin PTFE coatings to stainless steel substrate to enhance the tribological performance of PTFE as a solid lubricant coating [35]. The PDA/PTFE coating was able to reduce friction and wear of stainless steel substrates without the need to modify the substrate surfaces, which is important for bearing applications [7]. In this first study of PDA/PTFE coating, it was found to withstand approximately 500 times more rubbing cycles than PTFE film alone [35]. The coating performance was incrementally improved through the addition of various micro/nanoparticle fillers, modifying the PTFE heat-treatment process, and increasing the coating thickness [10], [39–47].

Preliminary studies showed that using a PDA adhesive underlayer also significantly improved PTFE coating durability on 60NiTi, which motivated the work presented in this dissertation. Deposition and testing of PDA/PTFE coatings on 60NiTi are presented in Chapter 3 alongside a systematic study of the effects of substrate surface roughness. The effectiveness of PDA/PTFE and its microstructural behavior during sliding are not fully understood. The present work provides greater depth to the explanation of PDA/PTFE-based coating effectiveness, and it provides new insight into the coating behavior.

The friction, deformation, and wear behavior of PDA/PTFE and PTFE and micro/nanoparticle composite coatings on stainless steel substrates have been studied through scratch and wear tests using tribometers with bearing balls as the counterface [35,39,41–50]. This macroscale testing method is effective for computing the quantitative durability of the coating in ball-on-disk configurations that mimic real applications. However, these tests lack microscale control of the applied normal load, and it is difficult to elucidate the microstructural behavior of the coating. These studies revealed PDA/PTFE to be an effective solid lubricant coating that drastically reduces the COF and is durable for thousands of rubbing cycles. However, the coating thickness was found to diminish quickly after the first few rubbing cycles, and the durability of the coating was attributed to a robust and well-adhered thin layer of coating at the substrate interface. Previous studies hypothesized from progressive testing that the early reduction in coating thickness could be attributed to delamination [39] and removal [35] of most of the PTFE coating before the counterface reached a more resilient layer of PTFE at the PDA/PTFE interface. However, plastic deformation of the coating was observed before delamination and failure during linear increasing macro-scale scratch tests [40]. The mechanisms that contributed to the early reduction in coating thickness were not fully understood. In the present work, nanoindenter scratch tests were performed to study the deformation behavior and failure mechanisms of the coating. These tests and their results are presented in Chapter 4 and Chapter 5.

1.2.3 PDA/PTFE as a Ball Bearing Lubricant

In certain bearing applications, contamination from grease and oil lubricants is a concern [51–53]. For example, a particular application of interest for 60NiTi/PDA/PTFE is centrifuge

bearings on the distillation assembly of the water recovery system on the International Space Station [23]. This system creates potable water from various waste streams on the spacecraft. The centrifuge bearings are exposed to highly acidic waste fluid, which causes corrosion on 440C stainless steel bearings. A recent design used soft cobalt alloy bearings, but these bearings can wear in use or be damaged during assembly [23]. Hybrid 60NiTi bearings are being explored as a solution to the existing corrosion and wear issues. However, tribological concerns hinder the use of 60NiTi in this application. Therefore, PDA/PTFE coating was explored as a ball bearing lubricant.

1.3 Outline of Methods

1.3.1 Nanomechanical Properties of Hardened 60NiTi (Chapter 2)

The microstructure of hardened 60NiTi was imaged using scanning electron microscopy (SEM) and characterized with energy-dispersive x-ray spectroscopy (EDS). The mechanical properties of 60NiTi and its phases were studied through nanoindentation. The high hardness and low elastic modulus exhibited by 60NiTi are caused by its unique microstructure. The high hardness results from an Orowan hardening mechanism caused by nanoscale Ni_4Ti_3 precipitates that form inside narrow B2 NiTi channels [28]. In addition to NiTi + Ni_4Ti_3, the microstructure of hardened 60NiTi commonly consists of larger, microscale Ni_3Ti precipitates [27]. The load-displacement behavior and mechanical properties of the NiTi + Ni_4Ti_3 region and Ni_3Ti precipitates were previously unknown. However, selectively performing low load and low displacement nanoindentations on this region and phase enabled their elastic modulus and hardness to be measured. Understanding the mechanical properties of this region and phase provided insights into the properties and tribological behavior of the bulk material.

1.3.2 The Effects of Surface Roughness on the Durability of PDA/PTFE Solid Lubricant Coatings on 60NiTi (Chapter 3)

A PTFE-based solid lubricant coating was developed for use on 60NiTi to solve pressing lubrication issues for 60NiTi mechanical component applications. A PDA adhesive underlayer was used to enhance the adhesion between 60NiTi and the thin (1-2 μm) PTFE coating. PDA was deposited on 60NiTi by immersing 60NiTi surfaces in a heated solution containing dopamine hydrochloride. PTFE was deposited using dip-coating. The coating was characterized by 3D laser scanning confocal microscopy (3DLSCM), stylus profilometry, atomic force microscopy (AFM), and SEM. The tribological performance of 60NiTi/PDA/PTFE was evaluated through ball-on-disk reciprocating wear tests with a tribometer. The effects of the substrate surface roughness on the tribological behavior of 60NiTi/PDA/PTFE were also studied using this form of tribological testing. Grinding and polishing procedures were developed to produce various degrees and forms of 60NiTi substrate surface roughness. Four different substrate surface finishes were investigated: mirror-finish, light polishing, sandpaper-roughened, and a valley-dominated surface produced through a combination of sandpaper-roughening and polishing. The wear tracks and counterfaces were analyzed by 3DLSCM, stylus profilometry, SEM, and EDS. The PDA/PTFE coating was shown to be an effective solid lubricant for 60NiTi in the tested conditions, and the valley-dominant substrate surface roughness greatly improved the durability of the coating.

1.3.3 Microscale Friction and Deformation Behavior of PDA)/PTFE-coated 60NiTi from Nanoscratch Tests (Chapter 4)

The microscale friction and deformation behavior of 60NiTi/PDA/PTFE was studied through nanoindenter scratch tests. The scratch behavior of PDA/PTFE coatings has traditionally been studied using macro-scale tribometers. However, macroscale tribological tests lack microscale control of the applied normal load, and the resulting coating deformation cannot be readily measured at the nanoscale. Nanoscratch tests enable a higher degree of control over the applied normal load and measure deformation at the nanoscale. Wear is a phenomenon that largely takes place at the micro and nanoscale because it is driven by the interactions between surface asperities. Therefore, nanoindenter scratch studies are very useful for studying wear mechanisms.

To properly understand tribological behavior, the differences between the apparent area of contact and real area of contact must be considered. Nanoindentation scratch tests were performed using a 5-μm-radius spheroconical diamond tip and the applied normal load ranged from 25 to 8000 μN. The ball-on-disk tribometer tests in Chapter 3 were performed using a 6.35-mm-diameter Si_3N_4 ball and an applied normal load of 2 N. The theoretical Hertzian contact pressure of a spherical Si_3N_4 ball with 6.35-mm-diameter pressured against flat 60NiTi with 2-N load is 615 MPa. For comparison, this same theoretical Hertzian contact pressure is achieved by pressing a diamond sphere with 5-μm-radius against a flat plate of 60NiTi with a load of 4.95 μN. Therefore, the theoretical contact stresses of the nanoindenter scratch tests are higher than the theoretical contact stress of the linear-reciprocating tribometer tests. However, real surfaces are not perfectly spherical or perfectly flat. The real contact area of surfaces is dictated by

surface asperities, and wear is driven by asperity interactions. Nanoindenter scratch tests with small, sharp indenters can approximate these asperity interactions and provide valuable insights to the wear mechanisms that occur during sliding contact of macro-scale mechanical components.

Nanoindenter scratch tests were performed on 60NiTi, 60NiTi/PDA, and 60NiTi/PDA/PTFE. The study revealed that PDA/PTFE coating failure is strongly correlated with the removal of the PDA particles in the underlayer. The findings also suggest that the compaction of the thin PDA/PTFE coatings could be the main reason for the previously reported large initial wear depth in macro-scale tribology studies.

1.3.4 Repetitive Nanoindenter Scratch Testing of PDA/PTFE-based Thin Coatings (Chapter 5)

The SEM images of nanoindenter scratches on 60NiTi/PDA/PTFE showed that the coating deformed plastically under lower-load scratches and was compressed to form a more solid and uniform coating structure. Therefore, a method was developed to perform and image repetitive nanoindenter scratches to study the behavior of the scratch-compacted coating. The results and analysis provided new insights into the progression of coating failure. Furthermore, this method was used to analyze the behavior of 60NiTi/PDA/PTFE with varying substrate roughness and with graphite particles incorporated in the PTFE layer. The testing revealed differences in the microstructural behavior of the various coatings that explain the remarkably enhanced performance of 60NiTi/PDA/PTFE coatings when the substrate is rough and graphite particles are added to the PTFE layer.

1.3.5 PDA/PTFE-coated Ball Bearings (Chapter 6)

A particular application of interest for 60NiTi/PDA/PTFE is a ball bearing in the harsh environment of the water recovery system on the International Space Station. The previous studies suggest that PDA/PTFE could perform well in this application. However, PDA/PTFE coatings have never been applied to ball bearings. In this chapter, methods are presented for applying PDA/PTFE coating to ball bearing components. Hybrid 440C/Si_3N_4 bearings with snap-in cages were used so that assembly and disassembly could be done without damaging the bearing components and the coating. The bearings were disassembled, the races and balls were coated with PDA/PTFE, and then the bearings were reassembled. A custom-built bearing tester was used to evaluate the effectiveness of the PDA/PTFE-coated bearings compared to dry bearings (non-lubricated) and grease-lubricated bearings. Radial loads were applied to the bearings and an accelerometer was used to detect bearing vibrations. Additionally, thermocouples were used to measure temperature near the bearings during operation. The bearings were disassembled periodically, and the races and balls were inspected through 3DLSCM. The coated bearing tests mark a transition from PDA/PTFE coating development on flat substrates and tribometer-based testing to direct evaluation as a ball bearing lubricant.

1.4 References

[1] C. DellaCorte, F. Thomas, and O. A. Leak, “Tribological evaluation of candidate gear materials operating under light loads in highly humid conditions,” in *Society of Tribologists and Lubrication Engineers Annual Meeting and Exhibition*, 2015.

[2] R. Neupane and Z. Farhat, “Wear and dent resistance of superelastic TiNi alloy,” *Wear*, vol. 301, no. 1–2, pp. 682–687, Apr. 2013, doi: 10.1016/J.WEAR.2012.11.017.

[3] S. v Pepper, C. DellaCorte, R. D. Noebe, D. R. Hall, and G. Glennon, “Nitinol 60 as a material for spacecraft triboelements,” in *13th European Space Mechanisms and Tribology Symposium 2009*, 2009.

[4] C. DellaCorte, L. E., I. Moore, J. S. Clifton, L. E., I. Moore, and J. S. Clifton, “Static Indentation Load Capacity of the Superelastic 60NiTi for Rolling Element Bearings.” 2012.

[5] C. DellaCorte and W. A. Wozniak, “Design and Manufacturing Considerations for Shockproof and Corrosion-Immune Superelastic Nickel-Titanium Bearings for a Space Station Application,” 2012.

[6] R. Neupane, Z. Farhat, R. Neupane, and Z. Farhat, “Wear Resistance and Indentation Behavior of Equiatomic Superelastic TiNi and 60NiTi,” *Materials Sciences and Applications*, vol. 6, no. 7, pp. 694–706, Jul. 2015, doi: 10.4236/MSA.2015.67071.

[7] C. DellaCorte, R. D. Noebe, M. Stanford, and S. A. Padula, “Resilient and corrosion-proof rolling element bearings made from superelastic Ni-Ti alloys for aerospace mechanism applications,” 2011.

[8] C. DellaCorte, S. v Pepper, R. Noebe, D. R. Hull, and G. Glennon, “Intermetallic nickel-titanium alloys for oil-lubricated bearing applications,” 2009.

[9] T. W. Scharf and S. v Prasad, “Solid lubricants: a review,” *J Mater Sci*, vol. 48, no. 2, pp. 511–531, 2013, doi: 10.1007/s10853-012-7038-2.

[10] D. Choudhury, C. Miller, and M. Zou, “Tribological performance of PDA/PTFE+ graphite particle coatings on 60NiTi,” *Appl Surf Sci*, vol. 527, p. 146731, 2020.

[11] C. Miller, D. Choudhury, and M. Zou, “The Effects of surface roughness on the durability of polydopamine/PTFE solid lubricant coatings on NiTiNOL 60,” *Tribology Transactions*, vol. 62, no. 5, pp. 919–929, 2019.

[12] D. Choudhury, C. Miller, N. Harris, and M. Zou, “The effect of coating thickness on the tribological properties of polydopamine/PTFE+ graphite particle coatings on 60NiTi,” *Surf Coat Technol*, vol. 420, p. 127320, 2021.

[13] W. J. Buehler, J. v Gilfrich, and R. C. Wiley, “Effect of low-temperature phase changes on the mechanical properties of alloys near composition TiNi,” *J Appl Phys*, vol. 34, no. 5, pp. 1475–1477, 1963.

[14] W. J. Buehler, J. v Gilfrich, and R. C. Wiley, “Effect of low-temperature phase changes on the mechanical properties of alloys near composition TiNi,” *J Appl Phys*, vol. 34, no. 5, pp. 1475–1477, 1963.

[15] K. Khanlari, M. Ramezani, and P. Kelly, “60NiTi: a review of recent research findings, potential for structural and mechanical applications, and areas of continued investigations,” *Transactions of the Indian Institute of Metals*, vol. 71, no. 4, pp. 781–799, 2018.

[16] C. Miller, C. DellaCorte, and M. Zou, “Nanomechanical properties of hardened 60NiTi,” *Materials Science and Engineering: A*, vol. 800, p. 140284, 2021.

[17] O. Benafan, A. Garg, R. D. Noebe, H. D. Skorpenske, K. An, and N. Schell, "Deformation characteristics of the intermetallic alloy 60NiTi," *Intermetallics (Barking)*, vol. 82, pp. 40–52, 2017.

[18] "SPECIFICATION FOR 60Ni-40Ti BILLETS." NASA Standard, Dec. 10, 2020.

[19] M. K. Stanford, "Charpy impact energy and microindentation hardness of 60-NITINOL," 2012.

[20] M. K. Stanford, "Preliminary investigation of surface treatments to enhance the wear resistance of 60-nitinol," 2016.

[21] M. K. Stanford, "Hot isostatic pressing of 60-Nitinol," National Aeronautics and Space Administration, Glenn Research Center, 2015.

[22] M. K. Stanford, "Hardness and microstructure of binary and ternary nitinol compounds," National Aeronautics and Space Administration, Glenn Research Center, 2019.

[23] C. DellaCorte, "Novel super-elastic materials for advanced bearing applications," in *Advances in Science and Technology*, Trans Tech Publ, 2014, pp. 1–9.

[24] C. DellaCorte, "NiTi Alloys: New Materials that enable Shockproof, Corrosion Immune Bearings," in *Society of Tribologists and Lubrication Engineers (STLE) Section Meeting*, 2017.

[25] C. DellaCorte, M. K. Stanford, and T. R. Jett, "Rolling contact fatigue of superelastic intermetallic materials (SIM) for use as resilient corrosion resistant bearings," *Tribol Lett*, vol. 57, no. 3, pp. 1–10, 2015.

[26] C. DellaCorte and M. Jefferson, "60NiTi Intermetallic Material Evaluation for Lightweight and Corrosion Resistant Spherical Sliding Bearings for Aerospace Applications, Report on NASA-Kamatics SAA3-1288," in *Tribology Frontiers Conference*, 2015.

[27] B. C. Hornbuckle, R. D. Noebe, and G. B. Thompson, "Influence of Hf solute additions on the precipitation and hardenability in Ni-rich NiTi alloys," *J Alloys Compd*, vol. 640, pp. 449–454, 2015.

[28] B. C. Hornbuckle, X. Y. Xiao, R. D. Noebe, R. Martens, M. L. Weaver, and G. B. Thompson, "Hardening behavior and phase decomposition in very Ni-rich Nitinol alloys," *Materials Science and Engineering: A*, vol. 639, pp. 336–344, 2015.

[29] B. C. Hornbuckle, "Investigations in phase stability and mechanical attributes in nickel-rich Nitinol with and without hafnium additions," Doctoral Dissertation, The University of Alabama, 2014.

[30] K. Khanlari, M. Ramezani, P. Kelly, P. Cao, and T. Neitzert, “Reciprocating sliding wear behavior of 60NiTi as compared to 440C steel under lubricated and unlubricated conditions,” *Tribology Transactions,* vol. 61, no. 6, pp. 991–1002, 2018.

[31] K. Khanlari, M. Ramezani, P. Kelly, and T. Neitzert, “Effect of hafnium addition in 60NiTi alloy hardened under open atmosphere conditions,” *Metallography, Microstructure, and Analysis,* vol. 7, no. 4, pp. 476–486, 2018.

[32] C. DellaCorte, “Ni-Ti Next Generation Bearings for Space Applications,” in *Schaeffler International Bearing Meeting*, 2018.

[33] T. L. Oberle, “Wear of metals,” *Jom,* vol. 3, no. 6, pp. 438–439, 1951.

[34] S. K. Biswas and K. Vijayan, “Friction and wear of PTFE—a review,” *Wear,* vol. 158, no. 1–2, pp. 193–211, 1992.

[35] S. Beckford and M. Zou, “Wear resistant PTFE thin film enabled by a polydopamine adhesive layer,” *Appl Surf Sci*, vol. 292, pp. 350–356, 2014.

[36] H. Lee, “Bioadhesion of Mussels and Geckos: Molecular Mechanics, Surface Chemistry, and Nanoadhesives,” Doctoral Dissertation, Northwestern University, Evanston, IL, 2008.

[37] J. H. Ryu, P. B. Messersmith, and H. Lee, “Polydopamine Surface Chemistry: A Decade of Discovery,” *ACS Appl Mater Interfaces*, vol. 10, no. 9, pp. 7523–7540, Mar. 2018, doi: 10.1021/acsami.7b19865.

[38] C. Zhang *et al.*, “Deposition and Adhesion of Polydopamine on the Surfaces of Varying Wettability,” *ACS Appl Mater Interfaces*, vol. 9, no. 36, pp. 30943–30950, Sep. 2017, doi: 10.1021/acsami.7b09774.

[39] F. Soltani-Kordshuli *et al.*, “Tribological behavior of the PDA/PTFE+ Cu-SiO2 nanoparticle thin coatings,” *Surf Coat Technol*, vol. 409, p. 126852, 2021.

[40] Y. Zhao and M. Zou, “Experimental investigation of the wear mechanisms of thin PDA/PTFE coatings,” *Prog Org Coat*, vol. 137, p. 105341, 2019.

[41] Y. Jiang, D. Choudhury, M. Brownell, A. Nair, J. A. Goss, and M. Zou, “The effects of annealing conditions on the wear of PDA/PTFE coatings,” *Appl Surf Sci*, vol. 481, pp. 723–735, 2019.

[42] S. K. Ghosh, C. Miller, D. Choudhury, J. A. Goss, and M. Zou, “The effects of PTFE thickness on the tribological behavior of thick PDA/PTFE coatings,” *Tribology Transactions*, vol. 63, no. 3, pp. 575–584, 2020.

[43] S. Beckford, Y. A. Wang, and M. Zou, “Wear-resistant PTFE/SiO2 nanoparticle composite films,” *Tribology Transactions*, vol. 54, no. 6, pp. 849–858, 2011.

[44] S. Beckford, J. Cai, J. Chen, and M. Zou, “Use of Au nanoparticle-filled PTFE films to produce low-friction and low-wear surface coatings,” *Tribol Lett*, vol. 56, no. 2, pp. 223–230, 2014.

[45] S. Beckford, L. Mathurin, J. Chen, and M. Zou, “The influence of Cu nanoparticles on the tribological properties of polydopamine/PTFE+ Cu films,” *Tribol Lett*, vol. 59, no. 1, pp. 1–9, 2015.

[46] S. Beckford, J. Cai, R. A. Fleming, and M. Zou, “The effects of graphite filler on the tribological properties of polydopamine/PTFE coatings,” *Tribol Lett*, vol. 64, no. 3, pp. 1–10, 2016.

[47] S. Beckford, L. Mathurin, J. Chen, R. A. Fleming, and M. Zou, “The effects of polydopamine coated Cu nanoparticles on the tribological properties of polydopamine/PTFE coatings,” *Tribol Int*, vol. 103, pp. 87–94, 2016.

[48] A. Abe, D. Choudhury, and M. Zou, “Improved tribological performance of polydopamine/polytetrafluoroethylene thin coatings with silica nanoparticles incorporated into the polydopamine underlayer,” *J Tribol*, vol. 143, no. 11, 2021.

[49] D. Choudhury, I. I. Niyonshuti, J. Chen, J. A. Goss, and M. Zou, “Tribological performance of polydopamine+ Ag nanoparticles/PTFE thin films,” *Tribol Int*, vol. 144, p. 106097, 2020.

[50] M. Zou, H. Wang, P. R. Larson, K. L. Hobbs, M. B. Johnson, and O. K. Awitor, “Ni nanodot-patterned surfaces for adhesion and friction reduction,” *Tribol Lett*, vol. 24, no. 2, pp. 137–142, 2006.

[51] S. A. Howard, C. DellaCorte, M. J. Dube, and L. Hawkins, “Magnetically Levitated Space Mechanisms,” *2020 NASA Engineering and Safety Center Technical Update*, 2020.

[52] M. J. Todd, “Solid lubrication of ball bearings for spacecraft mechanisms,” *Tribol Int*, vol. 15, no. 6, pp. 331–337, 1982.

[53] M. Nishimura and M. Suzuki, “Solid-lubricated ball bearings for use in a vacuum—state-of-the-art,” *Tribol Int*, vol. 32, no. 11, pp. 637–647, 1999.

CHAPTER 2

NANOMECHANICAL PROPERTIES OF HARDENED 60NITI

Abstract

The nanomechanical properties of hardened 60NiTi were studied using nanoindentation. The hardened 60NiTi consists of two regions: the NiTi + Ni_4Ti_3 region, which is composed of a B2 NiTi matrix and nanoscale Ni_4Ti_3 precipitates, and the globular Ni_3Ti precipitates. Blind nanoindentation was first performed on 60NiTi using a diamond Berkovich without differentiating the regions. The two regions were then selectively indented using a diamond cube corner nanoindenter. The results show that the elastic modulus and hardness of the NiTi + Ni_4Ti_3 region were similar to those of bulk 60NiTi. The Ni_3Ti phase was found to have an elastic modulus that is more than double that of bulk 60NiTi and the NiTi + Ni_4Ti_3 region. The hardness was also found to be significantly higher. This study not only provides the first quantitative measurements of the mechanical properties of Ni_3Ti precipitates within 60NiTi but also suggests that the presence of large amounts of easily imaged Ni_3Ti could serve as a good indication of reduced amounts of Ni_4Ti_3, which could lead to lower overall hardness of the material.

2.1 Introduction

In the last decade, Ni-rich NiTi alloys have become increasingly interesting candidate materials for specialized bearing and gear applications. A distinct combination of material properties like high hardness, low elastic modulus, and extreme corrosion resistance have made these alloys promising candidates for solving pressing material problems faced by the National Aerospace and Space Administration (NASA). For example, NiTiNOL 60 bearings are being developed to replace bearings that experience corrosion and wear issues in the water recovery

system of the International Space Station [1]. To solve problems like this, extensive work has been carried out to understand the loadbearing, tribological, and time-temperature-transition (TTT) behavior of binary and ternary Ni-rich NiTiNOL compounds [1-8].

The binary nickel-titanium alloy containing 60 wt% Ni and 40 wt% Ti is known as NiTiNOL 60, or 60NiTi. This composition of nickel-titanium has been shown to achieve the highest hardness amongst the binary compounds after heat treatment at 1050 °C [2]. The high hardness is caused by precipitation hardening through the rapid formation of nanoscale Ni_4Ti_3 precipitates upon cooling from a solution-annealed condition. The Ni_4Ti_3 precipitates form inside of narrow B2 NiTi channels and cause an Orowan strengthening mechanism [3]. The portion of 60NiTi composed of these B2 NiTi channels and Ni_4Ti_3 precipitates will be referred to as the NiTi + Ni_4Ti_3 region. The Ni_4Ti_3 phase is metastable and will eventually decompose to larger, Ni-rich phases if the alloy is not quenched after being solutionized. Without proper quenching, a significant drop in hardness will occur from the precipitation of the metastable Ni_3Ti_2 and stable Ni_3Ti phases [4].

The hardening behavior of 60NiTi has been studied using Vickers and Rockwell hardness testers and mechanical testing systems [2, 5-8]. However, the existing literature lacks a study of the load-displacement behavior of 60NiTi in the μN to mN load range and with displacements on the order of nanometers, which is important for understanding the elastic behavior of 60NiTi in addition to its hardness. Furthermore, the load-displacement behavior and mechanical properties of the NiTi + Ni_4Ti_3 region and globular Ni_3Ti precipitates are unknown. Understanding the mechanical properties of this region and phase will help explain the properties of the bulk

material and can guide future developments of the 60NiTi microstructure for improved mechanical performance.

2.2 Experimental Methods

2.2.1 Sample Preparation

60NiTi coupons with dimensions 25.4 × 25.4 × 2 mm were cut by wire electrical discharge machining (EDM) from billets made using the Hot Isostatic Pressing Method (HIP) method described in NASA's technical standards [9]. The composition of the material, measured using Atomic Emission Spectroscopy and wet chemical methods, is shown in Table 2.1. The samples were heat-treated using a 1050 °C soak for 2 hours followed by a furnace cool to 900 °C and then a rapid water quench. Next, the samples were aged at 400 °C for an hour. This process has been shown to produce a NiTi microstructure which contains nanoscale Ni_4Ti_3 precipitates throughout [4, 10]. A secondary Ni_3Ti phase is dispersed throughout the NiTi + Ni_4Ti_3 region as micro-scale precipitates.

Table 2.1. Composition of the 60NiTi samples.

Element	Ni	Ti	C	O	Fe	Cu	N	H
Concentration (wt%)	59.6	40.4	0.003	0.03	0.02	0.01	<0.001	0.002

The 60NiTi coupons were ground and polished to a mirror-finish using a grinder-polisher machine (Buehler EcoMet 300 Polisher, Buehler) and a three-step process, all under a 6-lb load. First, they were ground flat with a 320-grit sandpaper for 9 minutes. Next, they were lapped with 9-μm polycrystalline diamond polishing suspension for 8 minutes. Lastly, they were polished

using 60-nm colloidal silica polishing suspension for 5 minutes. The process reduced the roughness of the surface to less than 15 nm of average roughness (R_a). However, the globular Ni_3Ti phase protruded several nanometers above the NiTi + Ni_4Ti_3 region. These protrusions could potentially be caused by the Ni_3Ti phase being harder and thus having a lower removal rate by the polishing suspension than the NiTi matrix. The slight alkalinity of colloidal silica solution could also have caused a mild etch that enhanced the contrast between the NiTi + Ni_4Ti_3 region and Ni_3Ti phase [2]. After the coupons were polished, they were cleaned by sonicating for 20 minutes each in acetone, isopropyl alcohol, 1.0% detergent, and deionized water. They were then dried with nitrogen gas and subsequently characterized and tested.

2.2.2 Sample Characterization

Sample surfaces were characterized using scanning electron microscopy (SEM) (VEGA3, Tescan and Nova Nanolab, FEI), energy dispersive x-ray spectroscopy (EDS) (XL30, Phillips/FEI), and atomic force microscopy (AFM) (Dimension Icon, Bruker). SEM was used to image the surface with secondary electron (SE) and back-scattered electron (BSE) detectors. The BSE images show high-resolution compositional maps of a surface which can be used to quickly distinguish the number of phases and their mutual textural relationships. The different phases of the alloy have different brightness that is relative to the atomic number of the elements present in each phase. EDS was used to identify the various phases of the material. Additionally, focused ion beam (FIB) milling was used to remove sections of 60NiTi and enable SEM cross-section views of the precipitates. Also, sample surfaces were imaged through scanning probe microscopy (SPM) with the nanoindenter (TriboIndenter, Hysitron) before and after indentations. The

roughness of the polished surfaces was measured with stylus profilometry (Dektak 150, Bruker, Santa Barbara, CA).

2.2.3 Nanoindentation

A diamond Berkovich tip with 150 nm tip radius was used to measure the modulus of elasticity and hardness of the material. The elastic moduli were calculated from the unloading portion of the load-displacement curves according to the method developed by Oliver and Pharr [11-12]. The following equation was used to convert reduced modulus of elasticity values (E_r) to the modulus of elasticity (E):

$$\frac{1}{E_r} = \frac{(1-\nu^2)}{E} + \frac{(1-{\nu_i}^2)}{E_i} \quad (1)$$

Where ν is the Poisson's ratio of the sample, ν_i is the Poisson's ratio of the indenter, E_r is the reduced modulus, E is the modulus of elasticity of the sample, and E_i is the modulus of elasticity of the indenter. The value used for the Poisson's ratio of 60NiTi was 0.34 [1] and for the polycrystalline diamond indenter was 0.07 [13]. The value used for the modulus of elasticity of the indenter was 1140 GPa [13].

Eight different maximum indentation loads (1000, 2000, 3000, 4000, 5000, 6000, 7000, and 8000 μN) were used to study the effects of indentation load/depth on the mechanical properties of 60NiTi. The tests were repeated five times at each load. These indents were load-controlled with constant loading and unloading rates of 200 μN/s. A holding time of five seconds at the maximum load was also applied to allow for compensation of creep and thermal drift.

To determine the mechanical properties of the NiTi + Ni_4Ti_3 region and the Ni_3Ti phase, a diamond cube corner tip with 100 nm tip radius was used to selectively indent on this region and phase at three different loads of 50, 100, and 250 μN. The tests were repeated three times at each load. The indents were load-controlled with a five-second holding time at the maximum load, but the loading and unloading rates were reduced to 10 μN/s due to the small indentation loads applied. The NiTi + Ni_4Ti_3 region and Ni_3Ti phase were identified during nanoindentation tests by imaging the surface using the in-situ scanning probe microscopy with the nanoindenter tip. The NiTi + Ni_4Ti_3 region is flat and uniform, but the Ni_3Ti phase is raised 10-30 nm above the NiTi + Ni_4Ti_3 region. This relationship between the topography and the composition of the sample can be seen from the AFM, SEM, and EDS analysis.

The cube corner tip was used with much smaller indentation loads than the Berkovich tip because the sharper tip allows for plastic deformation to be achieved at smaller load, depth, and plastic volume. Small indentation volumes were needed to isolate the measurements to the particular region or phase of the material. Thus, the material properties of the microscale Ni_3Ti phase (islands) can be measured more accurately and with minimal effects from the surrounding NiTi + Ni_4Ti_3 region. The selected loads of 50, 100, and 250 μN were high enough to cause plastic deformation of the sample, which is necessary to measure the hardness, yet low enough to not cause too much plastic deformation of the Ni_3Ti precipitates in order to confine the plastic deformation to within the Ni_3Ti precipitates and thus accurately measure the properties of the Ni_3Ti. Also, the 250 μN load indentation using the cube corner tip produced a similar displacement on NiTi + Ni_4Ti_3 to that of the 1000 μN load indentation on 60NiTi using the Berkovich tip. This overlap is helpful for comparing the results calculated using each tip.

To ensure that both nanoindentation tips produced accurate and comparable results, the tip-specific cross-sectional area change with contact depth, i.e., tip area function, was calibrated using a fused quartz sample of known elastic modulus and Poisson's ratio. The displacement range relevant to each tip was used during this tip area function calibration process. This ensures that each tip will accurately calculate the elastic modulus and hardness across a specific range of displacement depths. The results confirm that both tips provide similar measurements for the elastic modulus and hardness when indenting on 60NiTi. Additionally, Neupane et al. showed that the nanoindentation behavior of 60NiTi is not significantly affected by the loading rate [8].

2.3 Results and Discussion

2.3.1 Surface Characterizations

Figure 2.1 shows SEM images of the polished, hardened 60NiTi surface. The images in (a) and (b) were produced from the SE detector and the images in (c) and (d) were produced from the BSE detector. The light-colored plateaued regions are the secondary Ni_3Ti phase; the mild grey area that makes up the majority of the surface is the NiTi + Ni_4Ti_3 region. The small dark areas are an oxide phase formed during the manufacturing process [2, 14]. To determine the abundance of the matrix, the secondary phase, and the oxide phase, an imaging processing tool was used to perform area fraction analysis on the BSE images. Images with a view field of 300 μm were taken at three random locations on the 60NiTi surface for the area fraction analysis. The NiTi + Ni_4Ti_3 region was measured to cover 86.6 ± 1.1% of the surface. The Ni_3Ti precipitates accounted for 11.8 ± 1.0% of the surface and 1.6 ± 0.3% was composed of the oxide phase.

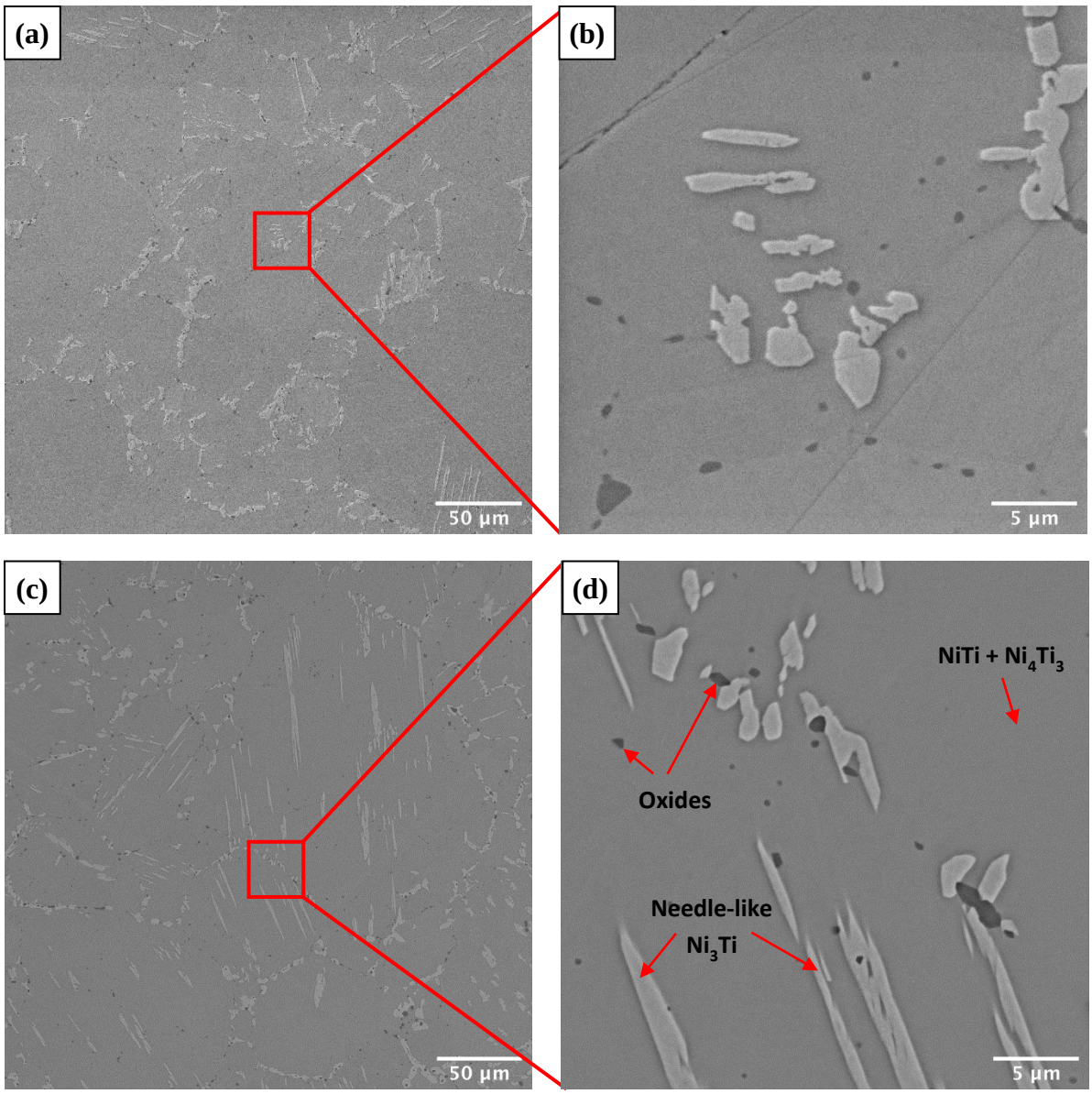

Figure 2.1. SEM images of the polished 60NiTi surface. (a) and (b) are SE images; (c) and (d) are BSE images. The various phases in the material are labeled in (d).

EDS was used to identify the composition of the different phases of the material [15]. Figure 2.2 shows the locations and the spectra for EDS point measurements on NiTi + Ni_4Ti_3, a globular-shaped precipitate, a needle-like precipitate, and an oxide phase. Since the Ni_3Ti precipitates appeared in the SEM images as two distinct shapes: globular and needle-like, EDS was used to confirm that all the light-colored precipitates, regardless of their shapes, were the

Ni_3Ti phase. The spectrum plotted in Figure 2.2(a) using the black, long-dashed line corresponds to the point measurement on the globular-shaped precipitate shown in Figure 2.2(c). The spectrum plotted in Figure 2.2(a) using the red, short-dashed line corresponds to the point measurement on the needle-shaped precipitate shown in Figure 2.2(d). These spectra are seen to overlap one another in Figure 2.2(a) and thus the two differently shaped precipitates have the same composition.

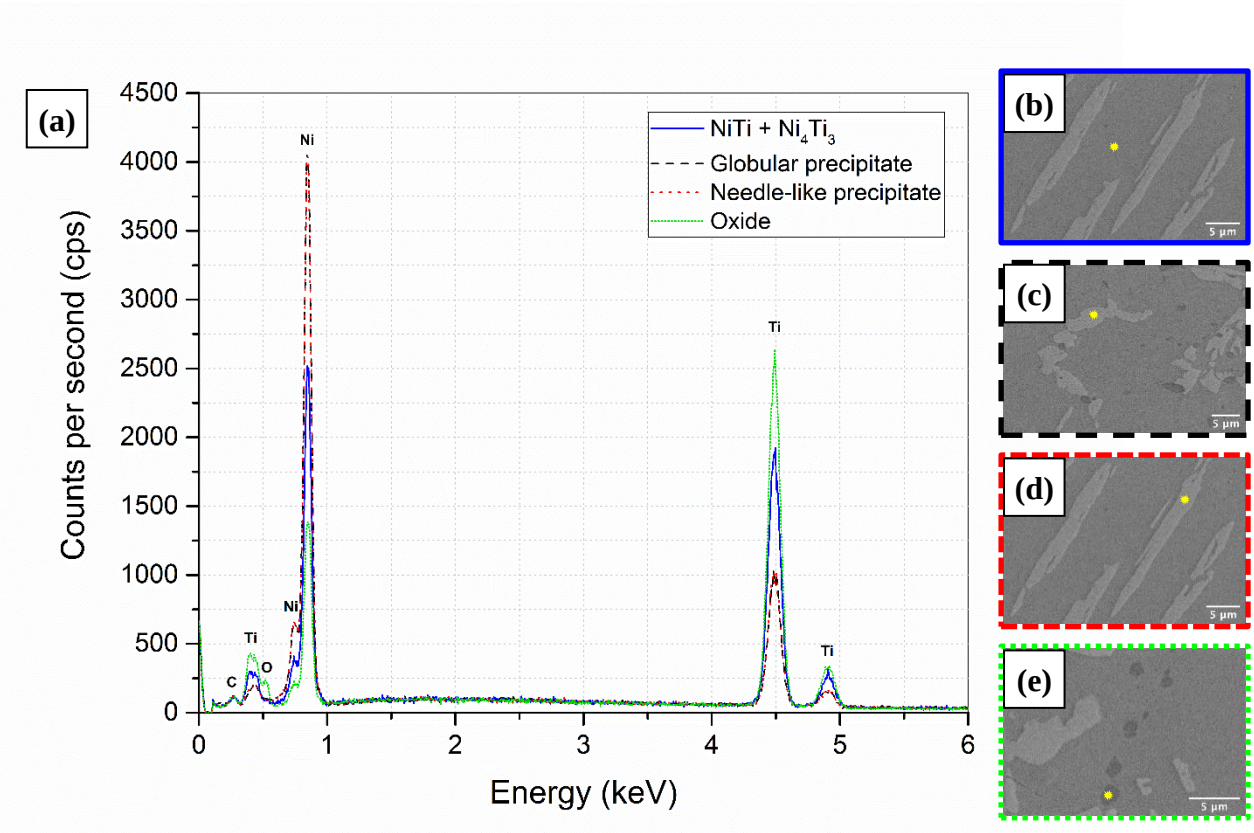

Figure 2.2. EDS analysis of 60NiTi. The spectra are shown in (e) and SEM images that show the locations of the EDS point measurements on NiTi + Ni_4Ti_3, a globular-shaped precipitate, a needle-like precipitate, and an oxide phase are shown in (b), (c), (d), and (e), respectively.

The Ni $L\beta_1$ peak at 0.866 KeV and the Ti $K\alpha_1$ peak at 4.512 KeV were very pronounced and the ratio between the peak height of these two peaks was used to identify the composition of the material. This Ni:Ti peak height ratio is not equal to the atomic ratio of the elements, but it

can be used to make inferences about the elemental composition. Three measurements were taken at different locations for the NiTi + Ni_4Ti_3 region, globular-shaped precipitates, needle-like precipitates, and the oxide phase. The average Ni:Ti ratio was calculated for each of these areas. As can be seen from Table 2.2, the Ni:Ti ratio of the NiTi + Ni_4Ti_3 region was measured to be 1.37 ± 0.04. The ratio for the globular-shaped precipitates was 3.94 ± 0.08 and for the needle-shaped precipitates it was 3.96 ± 0.13. Since the ratios for the globular- and needle-shaped precipitates were statistically indifferent and they were slightly less than three times the ratio for NiTi + Ni_4Ti_3, both shapes of these precipitates were determined to be the Ni_3Ti phase.

Table 2.2. Average Ni:Ti peak height ratios from EDS point measurements on the various phases of hardened 60NiTi.

Phase	Average Ni:Ti Ratio	Standard Deviation
NiTi + Ni_4Ti_3	1.37	0.04
Ni_3Ti globular	3.94	0.08
Ni_3Ti needle-like	3.96	0.13
Oxide	0.57	0.03

More detailed measurements may reveal that some of the phases identified as Ni_3Ti may slightly differ from one another, but for simplicity and based upon the semi-quantitative SEM EDS results, they will be called Ni_3Ti here. The primary concern that motivated the acquisition of these EDS measurements was whether the needle-like precipitates were composed of Ni_3Ti_2 rather than Ni_3Ti. Hornbuckle et al. showed that this Ni_3Ti_2 phase develops in certain Ni-Ti alloys and has a similar needle-like structure [3]. However, the present EDS studies showed that

the needle-shaped precipitates in these hardened 60NiTi samples more closely resembled Ni_3Ti than Ni_3Ti_2.

The oxide phase was found to have a Ni:Ti ratio of 0.57 ± 0.03. An oxygen peak appeared at 0.525 KeV for this phase and can be seen in Figure 2.2(e). Due to the spikes in Ti and O, it is likely that this phase is titanium dioxide. However, Ni still appears in a reduced quantity in these measurements because of the small size of the particles. X-rays could still be emitted from the Ni in the surrounding material because the particles were smaller than the spatial resolution for this form of analysis.

The AFM image in Figure 2.3 shows the polished 60NiTi surface and representative precipitates. From these images, the Ni_3Ti precipitates are shown to protrude above the NiTi + Ni_4Ti_3 region tens of nanometers. This allows these precipitates to be located when imaging with the nanoindenter tip and isolated indentations to be performed on them.

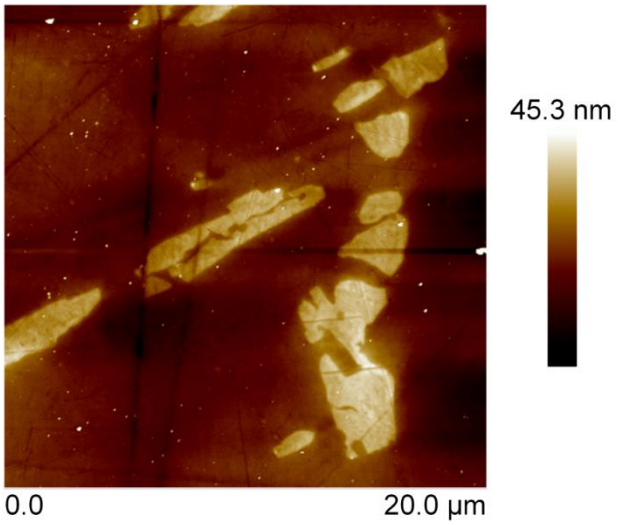

Figure 2.3. AFM image of the polished 60NiTi surface showing protruding Ni_3Ti precipitates.

FIB milling was used to investigate the depth of the Ni_3Ti precipitates. Figure 2.4 shows an SEM image of a Ni_3Ti precipitate that was FIB-milled until the bottom of the precipitate became visible. Multiple precipitates of various shapes and sizes were milled, and their depth varied from a few to several microns. The depth was on the same scale as the length and width dimensions that are visible on the surface of the material. These measurements verified that the depth of the Ni_3Ti precipitates was sufficient for nanoindentation to be used to measure the material properties with minimal effects from the surrounding NiTi + Ni_4Ti_3 region.

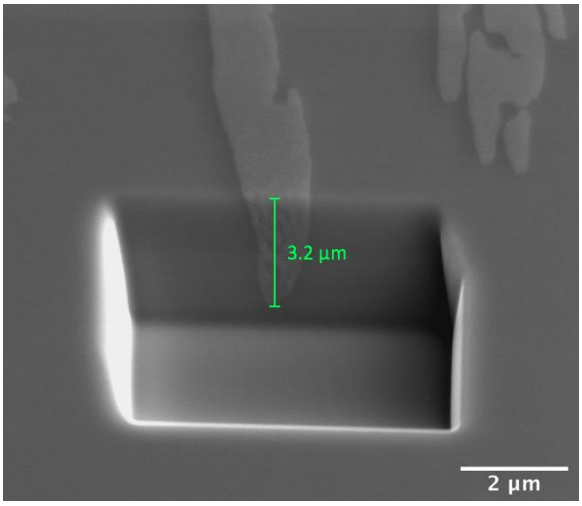

Figure 2.4. SEM image of a Ni_3Ti precipitate that was FIB-milled to reveal the precipitate's depth.

2.3.2 Nanoindentation

Representative load-displacement curves from the nanoindentation tests with the Berkovich tip are shown in Figure 2.5. One nanoindentation curve at each maximum load is shown. The loading portions of the curves were smooth and overlapped one another. Only slight variations occurred across the five indentations performed at each load. These variations are

reflected in the standard deviation of the modulus of elasticity and hardness calculated from these curves as shown in Figure 2.6. No significant dependence on the indentation load was observed for these values.

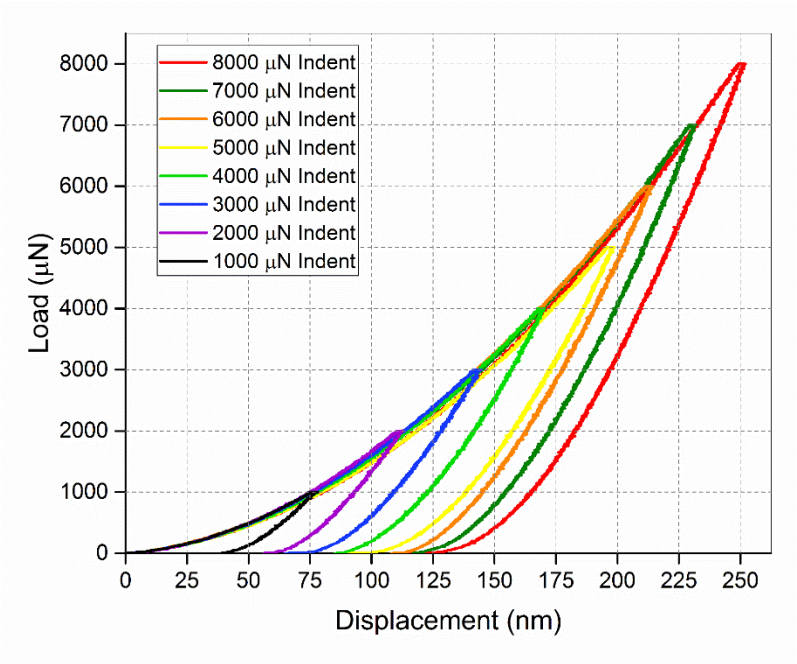

Figure 2.5. Load-displacement curves for 1000 – 8000 μN indents on 60NiTi using a Berkovich tip.

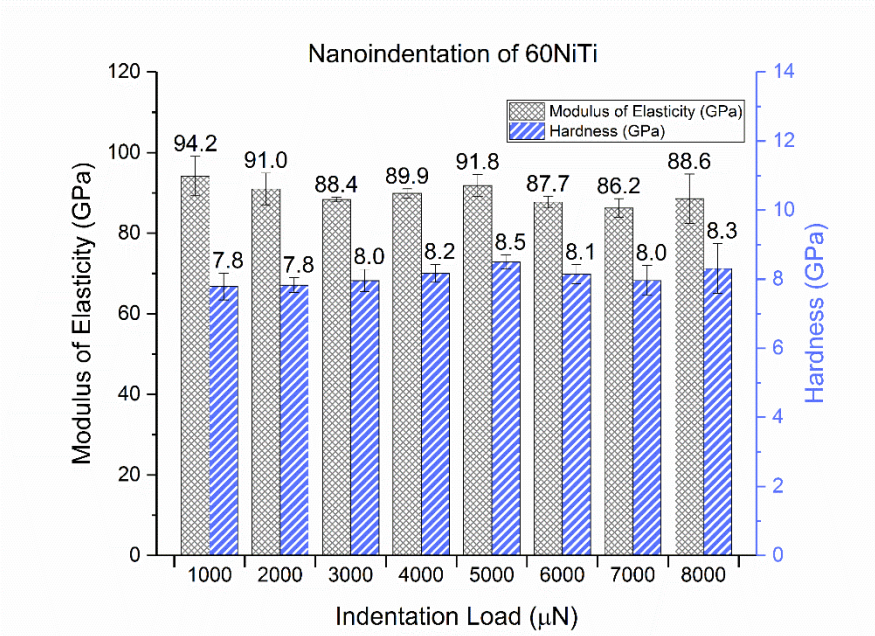

Figure 2.6. Modulus of elasticity and hardness of 60NiTi obtained from 1000 – 8000 μN load nanoindentations performed on 60NiTi using a Berkovich tip.

The average Young's modulus across all forty indents was 89.7 ± 3.9 GPa and the average hardness was 8.1 ± 0.4 GPa. The deviation is believed to be caused by the varying concentrations of the secondary Ni_3Ti precipitates at different indentation locations. These measurements were slightly lower than those reported by Neupane et al. from nanoindentation tests on solution treated 60NiTi [8]. However, their undisclosed solution treatment process may have differed from the one used in our study, and this could have produced differences in the microstructure and behavior of their solution-treated 60NiTi samples. They reported the Young's modulus to be 113 ± 4 GPa and the hardness to be 9.3 ± 0.2 GPa. In their studies, a diamond Berkovich indenter was used to indent 60NiTi at loads from 50 – 450 mN and with maximum depths from 0.5 – 2 μm. Their larger indentation loads and depths also could have caused their measurements to capture more of the bulk properties of the material, including the Ni_3Ti precipitates, whereas the lower load and depth indentations performed in this study mostly captured the properties of the NiTi + Ni_4Ti_3 region. However, the elastic modulus measurement in the present study (~90 GPa) compared more closely to the values reported for the bulk properties of 60NiTi in other studies (95-100 GPa) [1, 16].

A cube corner tip was used to image the surface and selectively indent the NiTi + Ni_4Ti_3 region and the Ni_3Ti phase at maximum loads of 50, 100, and 250 μN. The SPM topographic images were used to locate the NiTi + Ni_4Ti_3 regions and the Ni_3Ti precipitates for nanoindentation. The protruding nature of the Ni_3Ti precipitates made them easily distinguishable from the surrounding NiTi + Ni_4Ti_3 region in these images. Figure 2.7 shows an SPM image of the 60NiTi surface with 3 indents on both the NiTi + Ni_4Ti_3 region and a Ni_3Ti precipitate. Indents labeled 1-3 are on the NiTi + Ni_4Ti_3 region and are at maximum loads of 50,

100, and 250 μN, respectively. Indents labeled 4-6 are on the Ni_3Ti precipitate and are also at max loads of 50, 100, and 250 μN, respectively.

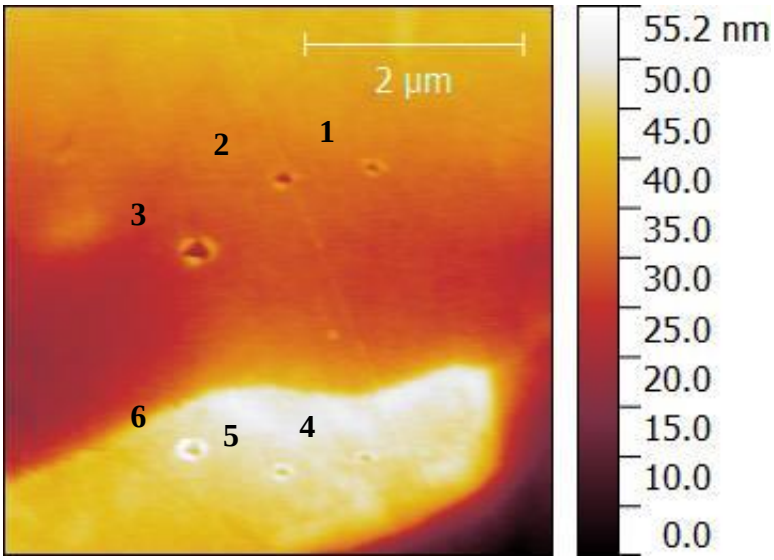

Figure 2.7. SPM image of the 60NiTi surface with indentations performed at points 1-6 with maximum loads of 50, 100, 250, 50, 100, and 250 μN, respectively. Points 1-3 are on the NiTi + Ni_4Ti_3 region and points 4-6 are on a Ni_3Ti precipitate.

Three indents were performed at each of the three loads on both the NiTi + Ni_4Ti_3 region and the Ni_3Ti precipitates. Figure 2.8 shows the load-displacement curves from these indents. The slopes of the loading and unloading portions of the curves for the indentations on the Ni_3Ti precipitates were significantly steeper than those of the indentations on the NiTi + Ni_4Ti_3 region. The shape of the indentation loading curves was very similar when the indentations were performed on the same precipitate, regardless of the indentation load. For example, the indents on Ni_3Ti in Figure 2.8 were all performed on the same precipitate. However, there was significant difference between the behaviors of the indentations on different precipitates. This can be seen in the large deviations of the modulus and hardness measurements, shown in Figure 2.9.

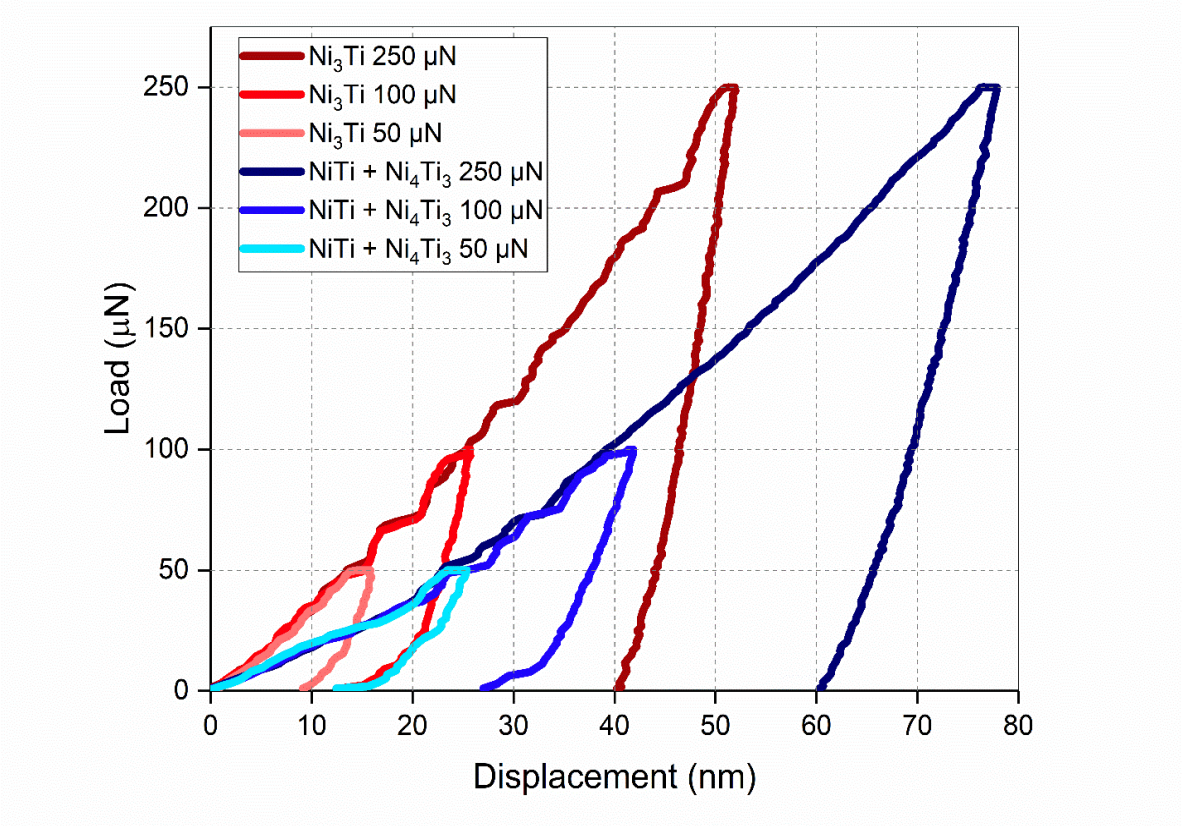

Figure 2.8. Load-displacement curves for 50, 100, and 250 μN indents on the NiTi + Ni_4Ti_3 region and a Ni_3Ti precipitate of 60NiTi. Indentations were made with a cube corner tip.

The results from the indentations on the NiTi + Ni_4Ti_3 region and the Ni_3Ti precipitate can be seen in Figure 2.9. Across the three different loads, the average modulus of elasticity of the NiTi + Ni_4Ti_3 region was 99.9 ± 8.3 GPa and the average hardness was 8.3 ± 0.9 GPa, which are similar to the values measured for hardened 60NiTi using the Berkovich tip and the values reported in literature for the bulk properties of 60NiTi [1, 13]. This result was expected since the majority of the bulk material is composed of the NiTi + Ni_4Ti_3 region. However, the measurements for the Ni_3Ti phase showed significant variation from the NiTi + Ni_4Ti_3 region. The elastic modulus and hardness of the Ni_3Ti phase were both much larger. The elastic modulus of the Ni_3Ti phase was 262 ± 33 GPa and the hardness was 13.1 ± 1.7 GPa. The large amounts of

variation in the measurements on the Ni_3Ti phase, both at the same and different maximum loads, are believed to be due to the varying size, shape, and flatness of the Ni_3Ti precipitates. Nonetheless, a clear trend was revealed by the data that suggests that the Ni_3Ti is stiffer and harder than the NiTi + Ni_4Ti_3 region and bulk 60NiTi.

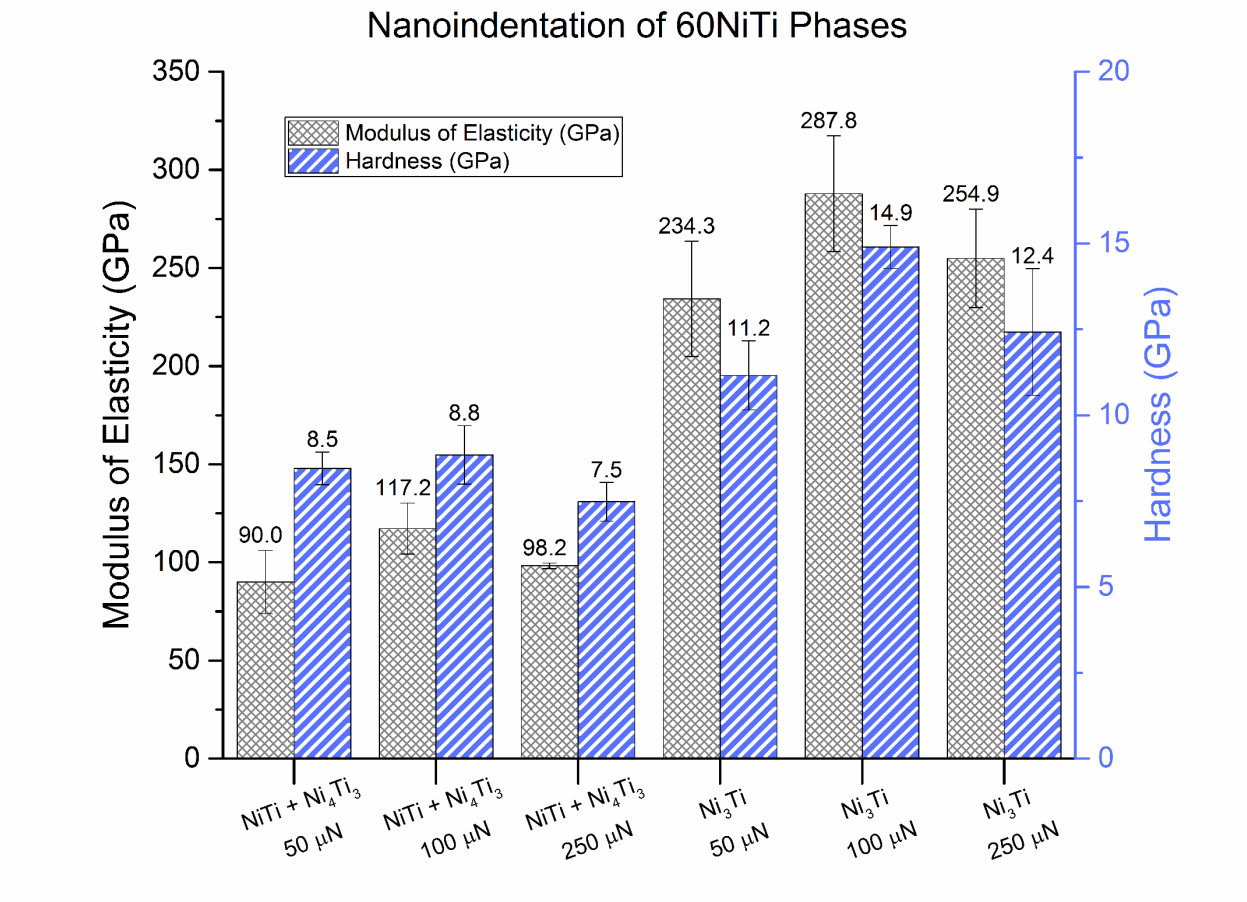

Figure 2.9. Modulus of elasticity and hardness of the NiTi + Ni_4Ti_3 region and Ni_3Ti precipitates of 60NiTi obtained from nanoindentations at 50, 100, and 250 μN loads using a cube corner tip.

Determining the mechanical properties of the Ni_3Ti precipitates helps to further the understanding of their effects on the bulk properties of 60NiTi. Despite Ni_3Ti being a hard phase, the hardness of 60NiTi has been shown to be less when there is a higher volume of Ni_3Ti

precipitates [2, 13], such as in homogenized 60NiTi. This occurs because the nanoscale Ni_4Ti_3 precipitates in the NiTi + Ni_4Ti_3 region must be reduced in order to form more Ni_3Ti [17]. When this occurs, the Orowan strengthening mechanism provided by the nanoscale Ni_4Ti_3 precipitates in the NiTi matrix is weakened and the hardness of the bulk material decreases. This study not only provides the first quantitative measurements of the mechanical properties of Ni_3Ti precipitates within 60NiTi but also suggests that the presence of large amounts of easily imaged Ni_3Ti could serve as a good indication of reduced amounts of Ni_4Ti_3, which could lead to lower overall hardness of the material.

2.4 Conclusions

The nanoindentation behavior of 60NiTi was studied using a nanoindenter with a Berkovich tip and a cube corner tip. Using the Berkovich tip, the elastic modulus and hardness of the material were found to be 89.7 ± 3.9 GPa and 8.1 ± 0.4 GPa, respectively. However, nanoindentations of the NiTi + Ni_4Ti_3 region and the globular Ni_3Ti precipitates using the cube corner tip revealed significant differences in their mechanical properties. The NiTi + Ni_4Ti_3 region was found to have an elastic modulus of 99.9 ± 8.3 GPa and a hardness of 8.3 ± 0.9 GPa, while the Ni_3Ti precipitates were measured to have a much higher elastic modulus of 262 ± 33 GPa and hardness of 13.1 ± 1.7 GPa. The properties of hardened 60NiTi measured by the Berkovich tip resembled the properties of the NiTi + Ni_4Ti_3 region, but the Ni_3Ti phase had a much higher elastic modulus and hardness.

2.5 Acknowledgements

We thank the National Aeronautics and Space Administration (NASA) for the support under NASA Award No: 80NSSC17M0020 and Dr. Adam Howard at the NASA Glenn Research Center (GRC) for serving as our NASA Technical Monitor and Technical Contact.

2.6 References

[1] C. DellaCorte, Novel super-elastic materials for advanced bearing applications, Advances in Science and Technology. 89 (2014) 1-9.

[2] M.K. Stanford, Hardness and microstructure of binary and ternary nitinol compounds, NASA Technical Report, NASA/TM-2016-218946, 2016.

[3] B.C. Hornbuckle, X.X. Yu, R.D. Noebe, R. Martens, M.L. Weaver, G.B. Thompson, Hardening behavior and phase decomposition in very ni-rich nitinol alloys, Mater. Sci. Eng. A 639, (2015) 336-344.

[4] B.C. Hornbuckle, R.D. Noebe, G.B. Thompson, Influence of Hf solute additions on the precipitation and hardenability in Ni-rich NiTi alloys, J. Alloys Compd. 640 (2015) 449-454.

[5] O. Benafan, A. Garg, R.D. Noebe, H.D. Skorpenske, K. An, N. Schell, Deformation characteristics of the intermetallic alloy 60NiTi, Intermetallics 82 (2017) 40-52.

[6] K. Khanlari, M. Ramezani, P. Kelly, T. Neitzert, Effect of hafnium addition in 60NiTi alloy hardened under open atmosphere conditions, Metallography, Microstructure, and Analysis 7 (2018) 476-486.

[7] R. Neupane, Z. Farhat, Wear and dent resistance of superelastic TiNi alloy, Wear 301 (1) (2013) 682-687.

[8] R. Neupane, Z. Farhat, Wear resistance and indentation behavior of equiatomic superelastic TiNi and 60NiTi, Materials Sciences and Applications 6 (2015) 694-706.

[9] SPECIFICATIONS FOR 60Ni-40Ti BILLETS, MSFC-SPEC-3706, 2016.

[10] M.K. Stanford, Preliminary investigation of surface treatments to enhance the wear resistance of 60-nitinol, NASA Technical Report, NASA/TM-2016-219121, 2016.

[11] W.C. Oliver, G.M. Pharr, An Improved Technique for Determining Hardness and Elastic Modulus Using Load and Displacement Sensing Indentation Experiments, Journal of Materials Research 7 (6) (1992) 1564-1583.

[12] W.C. Oliver, G.M. Pharr, Measurement of Hardness and Elastic Modulus by Instrumented Indentation: Advances in Understanding and Refinements to Methodology, Journal of Materials Research 19 (1) (2004) 3–20.

[13] Hysitron, Inc., TriboIndenter® Users Manual, 2001.

[14] M. Nishida, C.M. Wayman, T. Honma, Precipitation processes in near-equiatomic TiNi shape memory alloys, Metall. Trans. A 17 (9) (1986) 1505-1515.

[15] C. Yan, Q. Zeng, Y. Xu, W. He, Microstructure, phase and tribocorrosion behavior of 60NiTi alloy, Appl. Surf. Sci. 498 (2019) 143838.

[16] M.K. Stanford, Charpy Impact Energy and Microindentation Hardness of 60-NITINOL, NASA Technical Report, NASA/TM—2012-216029, 2012.

[17] B.C. Hornbuckle, Investigation in phase stability and mechanical attributes in nickel-rich nitinol with and without hafnium additions, Doctoral Dissertation, University of Alabama, 2014.

CHAPTER 3

THE EFFECTS OF SURFACE ROUGHNESS ON THE DURABILITY OF POLYDOPAMINE/PTFE SOLID LUBRICANT COATINGS ON NITINOL 60

Abstract

NiTiNOL 60, or 60NiTi, is a nickel-titanium alloy being investigated for bearing and gear applications. 60NiTi has many desirable properties for these applications; for example, it is hard, electrically conductive, highly corrosion resistant, superelastic, and non-magnetic. However, its tribological performance is poor in unlubricated conditions. In this study, a PTFE coating with a polydopamine (PDA) adhesive underlayer was deposited on 60NiTi and evaluated for friction and wear reduction. Additionally, the effects of the substrate surface roughness on the tribological performance of the coating were investigated. The results showed that PDA/PTFE coating on 60NiTi reduced the coefficient of friction (COF) over 85% and prevented wear of 60NiTi for thousands of rubbing cycles during accelerated tests. Furthermore, modifying the 60NiTi substrate surface through various grinding and polishing procedures increased the durability of the coating over 30 times. Therefore, the coating and substrate surface combination showed the potential to provide solid lubrication for 60NiTi.

3.1 Introduction

Nickel-titanium alloys were first developed by W.J. Buehler in the Naval Ordinance Laboratory (NOL) in the 1950s, thus the name NiTiNOL was born (Ni-Ti NOL) [1, 2]. Neither a metal nor ceramic, NiTiNOL 60, or 60NiTi (60 wt % Ni, 40 wt % Ti), is a weakly ordered inter-metallic compound with peculiar properties compared to traditional engineering materials.

60NiTi exhibits the unique combination of high hardness and low Young's modulus [3-4]. The material can be heat treated to reach a hardness of 56 to 62 on the Rockwell C scale, while maintaining a low Young's Modulus around 90 GPa [5]. These characteristics, alongside being corrosion resistant, chemically inert, electrically conductive, and non-magnetic, make 60NiTi an enticing candidate for bearing applications [5-7]. The high hardness inhibits dents from forming and the low modulus reduces the contact pressure compared to traditional bearing materials. Due to these advantages, the National Aeronautics and Space Administration (NASA) has put forth significant amounts of work to develop 60NiTi bearings and gears [8-10].

However, poor tribological performance of 60NiTi has been observed in unlubricated contact. Under these conditions, 60NiTi has a high coefficient of friction (0.7 – 1.0) and a wear rate up to two orders of magnitude greater than that of 440C, a steel of similar hardness [11]. The high wear rate of 60NiTi is caused by abrasive wear, adhesive wear, and the propagation of microcracks due to shear stresses from sliding. These cracks lead to the fracture and removal of 60NiTi materials [11-12]. This necessitates the development of proper lubricants for 60NiTi [9]. The novel coatings in this study are being designed to address this problem. Specifically, these coatings are designed to enable 60NiTi ball bearings and timing gears to be developed for use in the water recovery system of the International Space Station (ISS).

Polytetrafluoroethylene (PTFE) has many desirable properties such as low COF, high temperature resistance, and chemical resistance, which lead to its use as a solid lubricant in many tribological applications [13]. It has been shown to be a compatible lubricant for 60NiTi [8]. However, PTFE thin coatings have high wear rates and low adhesion to most substrate materials.

To combat these weaknesses of PTFE thin films as solid lubricant coatings, a bio-inspired polydopamine (PDA) thin film has been developed to be used as an adhesive underlayer between PTFE and substrate materials [14]. PDA is a biomimetic polymer proposed by Lee et al. [15] as a surface modifier that allows further functionalization of a surface. The study by Beckford et al. [14] showed that a 600 nm-thick PTFE coating deposited on stainless steel substrates using an adhesive PDA underlayer (The coating is denoted as PDA/PTFE) was able to withstand approximately 500 times more rubbing cycles than the PTFE coating deposited on stainless steel directly. The addition of various nanoparticles or graphite particles to the PTFE coating has also been shown to improve the durability of PDA/PTFE coatings [16-19].

Another method used to increase the durability of PTFE coatings is to roughen the substrate surface. A rough substrate surface promotes mechanical interlocking between the coating and the substrate and prevents global delamination. Adhesion between the coating and the substrate is also improved when the substrate surface is roughened because the added roughness will increase the contact area between the coating and the substrate at the interface. However, high substrate roughness can also have negative effects on the tribological performance of the coating. If roughness is too great, then the thin film may not evenly cover the surface. Also, high peaks on a rough surface can serve as localized points of high contact pressure and can initiate the failure of the coating.

Burris et al. showed that counterface roughness has competing effects on the wear of a PTFE-based composite and the formation of a transfer film [20]. Particularly, they found counterface roughness peaks contributed to greater volume loss of the polymer composite, but

roughness valleys helped initiate the formation and stabilization of transfer films. Likewise, the roughness of the substrate surface has competing effects on the wear of polymer coatings. This experiment studies the effects of substrate roughness and develops an optimized substrate surface roughness to be used with thin PDA/PTFE coatings on 60NiTi.

3.2 Experimental Methods

Hardened 60NiTi coupons with dimensions 25.4 × 25.4 × 2 mm were ground, polished, and coated with PDA/PTFE. Four different polishing procedures were used to prepare 60NiTi samples to four varying surface finishes prior to being cleaned and coated. Three samples were prepared for each surface finish, resulting in a total of twelve 60NiTi + PDA/PTFE samples tested.

3.2.1 Sample Preparation

Grinding and lapping procedures were performed using a grinder/polisher machine. All samples were first polished to a mirror finish using a three-step process. First, the samples were ground flat with 320-grit sandpaper by grinding for 9 minutes at a 6-lb load. Next, the samples were lapped with a 9-μm polycrystalline diamond polishing suspension for 8 minutes at a 6-lb load. Lastly, they were lapped with a 60-nm colloidal silica polishing suspension for 5 minutes at a 6-lb load. This process brings all of the samples to a very flat and smooth mirror-finish. From the twelve samples polished to a mirror finish, three of the samples remained at this state and were denoted as S1-A, S1-B, and S1-C. Three other samples were further polished using the 9-μm polycrystalline diamond suspension for 1 minute at a 2-lb load and were denoted S2-A, S2-B, and S2-C. The remaining six samples were ground using the 320-grit sandpaper for 1 minute

at a 1-lb load. Three of these samples were then briefly lapped with the 9-μm polycrystalline diamond suspension for 15 seconds at a 1-lb load to remove peak asperities but retain the roughness dominated by valleys. These three samples were denoted S3-A, S3-B, and S3-C. The remaining three samples that were ground using the 320-grit sandpaper were denoted S4-A, S4-B, and S4-C. All samples were subsequently cleaned by sonicating for 20 minutes each in acetone, isopropyl alcohol, 1.0% detergent, and then in deionized water.

Next, the PDA adhesive underlayer was deposited on each sample surface through submerging the samples in a 700 mL solution of deionized (DI) water that was buffered to a pH of 8.5 by adding 0.848 grams of Tris base and 1.4 grams of dopamine hydrochloride. PTFE was deposited on top of the PDA underlayer using a dip-coater to dip the samples in an aqueous dispersion of PTFE at an insertion and withdrawal speed of 10 mm/min with a soak time of one second. The dip-coating process is pictured in Figure 3.1.

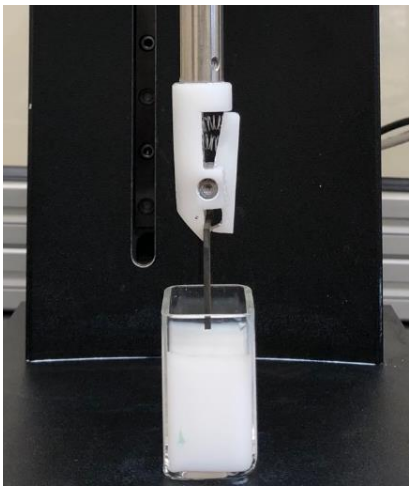

Figure 3.1. Dip-coating a 60NiTi sample with PTFE dispersion.

After the samples had been dip-coated, a heat treatment process was used to remove water and surfactants from the coating and to sinter the PTFE particles. The coated samples were heated first on a hot plate for 3 minutes at 120 °C, then in a furnace for 4 minutes at 300 °C, and lastly, for 4 minutes at 372 °C. A schematic of the finalized 60NiTi + PDA/PTFE sample is shown in Figure 3.2. Note that due to the sample clamping during the dip coating, part of the PDA coating at the edge of the sample is exposed without the PTFE top coat. Photographs of the samples are shown in Figure 3.3.

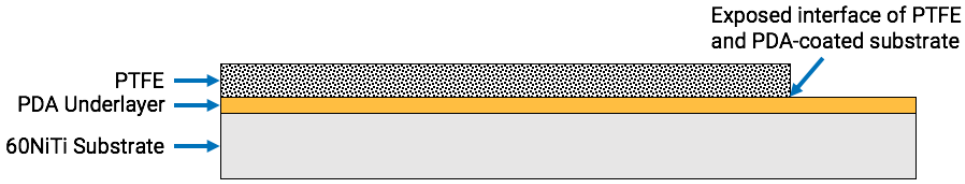

Figure 3.2. Schematic of a 60NiTi + PDA/PTFE sample that identifies the 60NiTi substrate, PDA and PTFE coating layers, and the exposed interface of the PTFE layer and the PDA-coated substrate.

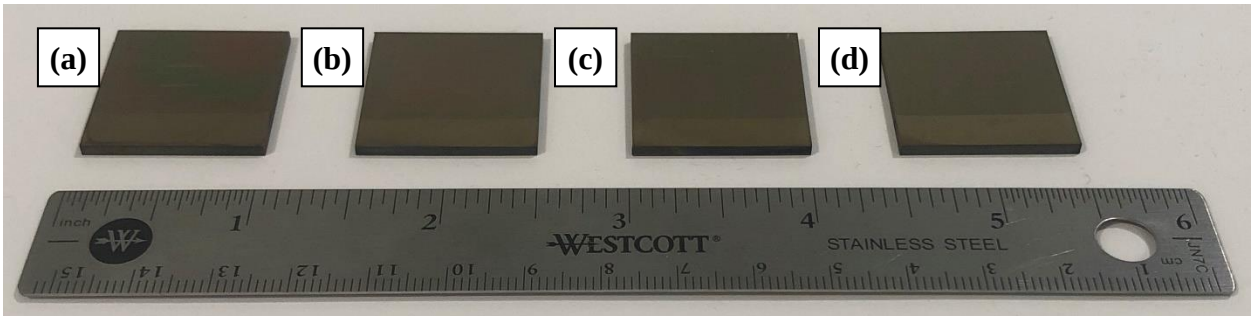

Figure 3.3. Photograph of (a) S1 + PDA/PTFE, (b) S2 + PDA/PTFE, (c) S3 + PDA/PTFE, and (d) S4 + PDA/PTFE after wear tests.

3.2.2 Tribological Testing

The tribological performance of the coated samples was evaluated by performing linear reciprocating friction and wear tests using a tribometer. The tests were performed in a ball-on-plate configuration where the ball was a 6.35 mm diameter Si_3N_4 ball and the plate was the

PDA/PTFE-coated 60NiTi sample. Tests were run with a normal load of 2 N, which corresponds to a Hertzian contact pressure of 615 MPa if the effects of the soft, thin coating are neglected. This load was chosen because the high contact pressure accelerated the tests and enabled the coating to be tested until failure in a reasonable amount of time. Other testing parameters include a stroke length of 5 mm and a sliding speed of 10 mm/s, with a failure criterion of frictional force exceeding 0.7 N, which is equivalent to a coefficient of friction of 0.35. The failure criterion was set because the coefficient of friction increased from around 0.1 to 0.75 when the PDA/PTFE solid lubricant coating had been worn through and the Si_3N_4 ball began to have unlubricated contact with the 60NiTi substrate. With the failure coefficient of friction threshold set at 0.35, the tests do not end prematurely or continue to run past the onset of the counterface ball wearing into the substrate. The reciprocating cycles until the failure threshold is reached defines the durability of the coating. One cycle corresponds to each time the counterface returns to its original position.

3.2.3 Sample Characterization

The roughness of all twelve S1-S4 substrate surfaces was measured using a stylus profilometer and was characterized by arithmetic mean roughness (R_a), root mean square roughness (R_q), peak to valley distance (R_T), and skewness (R_{sk}). The stylus profilometer was also used to measure the roughness of the coating, the profiles of the wear tracks after the durability tests, and the PTFE coating thickness. The coating thickness measurements were made from profile measurements across the exposed interface between the PDA-coated 60NiTi substrate and the PTFE coating (shown in Figure 3.2). Additionally, the morphology of the coating surfaces was imaged using atomic force microscopy.

The Si_3N_4 counterface balls and the wear tracks were imaged using 3D laser scanning microscopy and scanning electron microscopy (SEM) with energy dispersive x-ray spectroscopy (EDS). The counterface balls were imaged after the wear tests to observe transfer films and the wear tracks were imaged to identify the mechanisms of wear.

Nanoindentation was performed to measure the modulus of elasticity and the hardness of 60NiTi and the PDA/PTFE coating. Forty indents were performed on S1 60NiTi samples at loads between 1000 – 8000 μN using a Berkovich tip with a tip radius of 150 nm. A sphero-conical tip with a 1-μm radius was used to indent the PDA/PTFE coating at loads ranging from 20 – 50 μN.

3.3 Results and Discussion

3.3.1 Surface Characterization

Figure 3.4 shows the laser scanning microscope 3D images of the S1-S4 substrate surfaces produced by the various grinding and polishing procedures. The S1 substrate surfaces have a mirror finish and are extremely smooth. S2 surfaces have small unidirectional polishing lines but are still very smooth. S3 surfaces have deep grooves produced from sanding but the peaks are removed and replaced by plateaued regions similar to S2. Lastly, the S4 surfaces contain both the peaks and valleys produced from sanding and are the roughest surfaces.

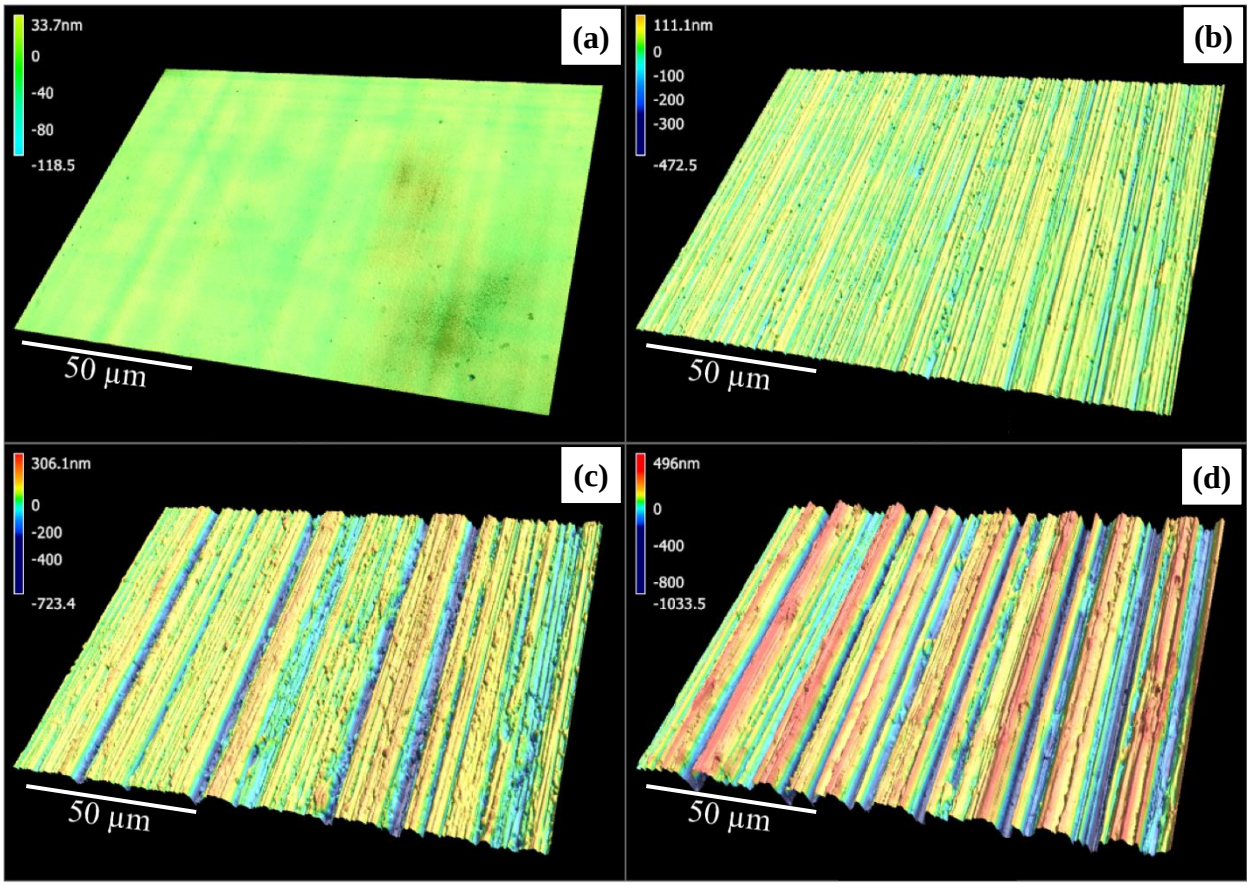

Figure 3.4. 3D laser scanning microscope images of the sample substrate surfaces (display of z-height is magnified). (a) S1, (b) S2, (c) S3, and (d) S4.

Figures 3.5 presents the roughness parameters measured from line profiles of all twelve sample substrate surfaces. The small variations of these measurements proved the effectiveness of the surface preparation procedures to repetitively produce surfaces with similar features. The R_a for the substrate types S1, S2, S3, and S4 is 8.9, 16.7, 69.6, and 127.9 nm, respectively, with the roughness of S3 and S4 being much higher than that of S1 and S2. The R_q and R_T measurements show similar increasing trends from S1 to S4 (Figure 3.5 (a)). The R_{sk} measurements indicate if the surface is dominated by peaks (positive skewness) or valleys (negative skewness). The S3 samples have the greatest negative skewness (-0.58) and the smallest standard deviation in skewness (Figure 3.5 (b)). This quantitative measure shows the

grinding and polishing procedure for the S3 substrates repetitively produced a surface that is dominated by valleys.

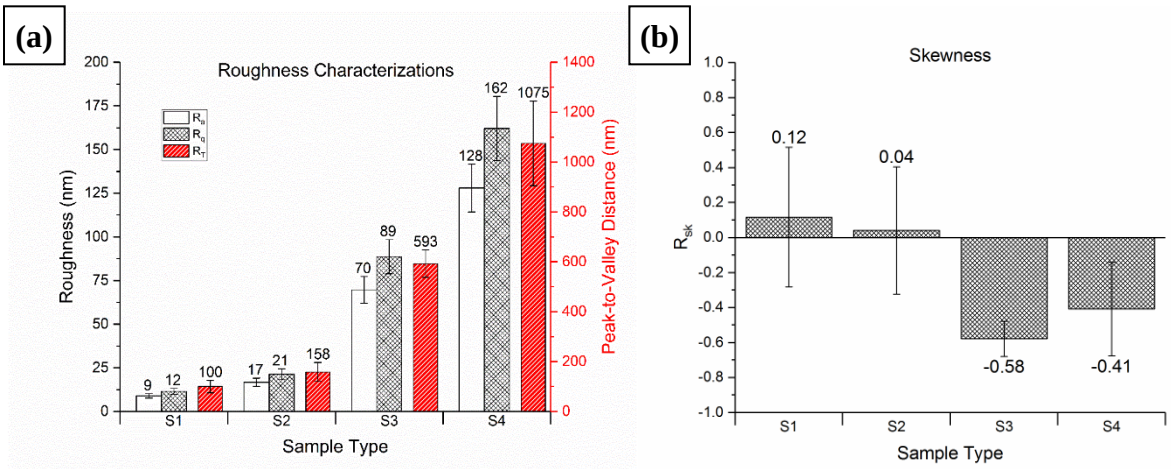

Figure 3.5. Roughness characterizations for substrate surfaces S1-S4. (a) arithmetic mean roughness, R_a, root mean square roughness, R_q, and peak to valley distance, R_T, and (b) skewness, R_{sk}.

The morphology of the coatings is shown in the AFM images in Figure 3.6. The shape and size of the PTFE needles are similar regardless of the substrate surface. However, the larger scale roughness of the coatings measured by the stylus profilometer differs with the substrate surface roughness. Two-millimeter-long profilometer measurements of the coating and substrate were used to measure R_a roughness and these values are shown in Figure 3.7. With the exception of S1 + PDA/PTFE, the roughness of the coating is around half of that of the substrate. This indicates that the coating conformed with the substrate surface and covered both the peaks and the valleys with more coating materials filled and retained in the valleys.

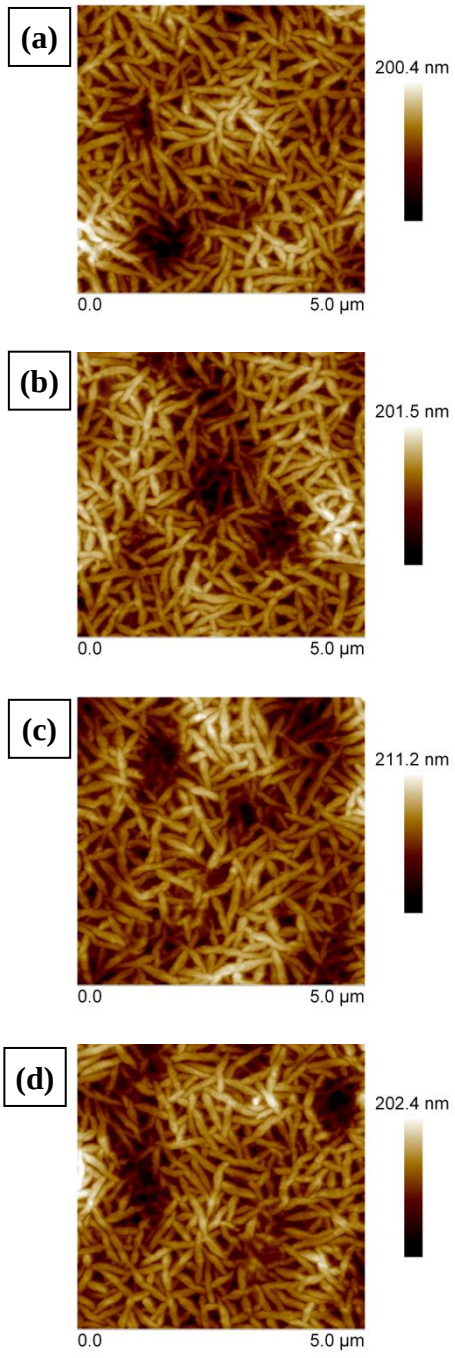

Figure 3.6. AFM images of PDA/PTFE coating morphology after deposition and heat treatment. (a) S1 + PDA/PTFE, (b) S2 + PDA/PTFE, (c) S3 + PDA/PTFE, and (d) S4 + PDA/PTFE.

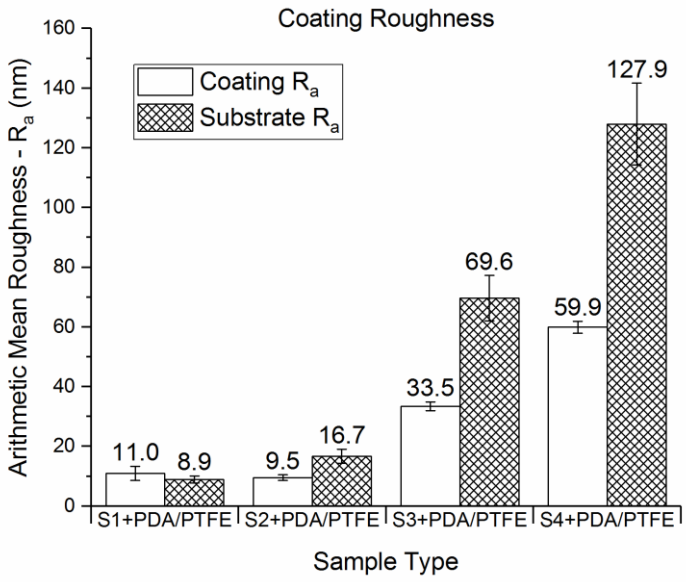

Figure 3.7. Roughness comparison of the coating surface and the substrate surface for S1-S4 + PDA/PTFE.

The thickness of the PTFE coatings, shown in Figure 3.8, was measured from the profile of the exposed interface between the PDA-coated 60NiTi substrate and the PTFE coating. The average measured PTFE coating thickness on the S1, S2, S3, and S4 substrates was 1.27, 1.30, 1.37, and 1.33 μm, respectively. These values are similar to each other and the standard deviations of the measurements on each substrate overlap. This indicates that there is not a substantial difference in the PTFE coating thickness due to substrate roughness. It should be noted that the measurements from this interface only capture the thickness of the PTFE portion of the coating. However, from previous studies [14, 16, 18-19], the thickness of the PDA layer is less than 50 nm and the color of the PDA layer changes drastically with coating thickness. The fact that the color of the PDA layers on all substrates are similar to the previous studies indicates that the thickness of the PDA layer was similar regardless of the substrate surface roughness.

Therefore, the PDA/PTFE coating thicknesses on all substrates are still similar to those of PTFE, which are about 1.3-1.4 μm.

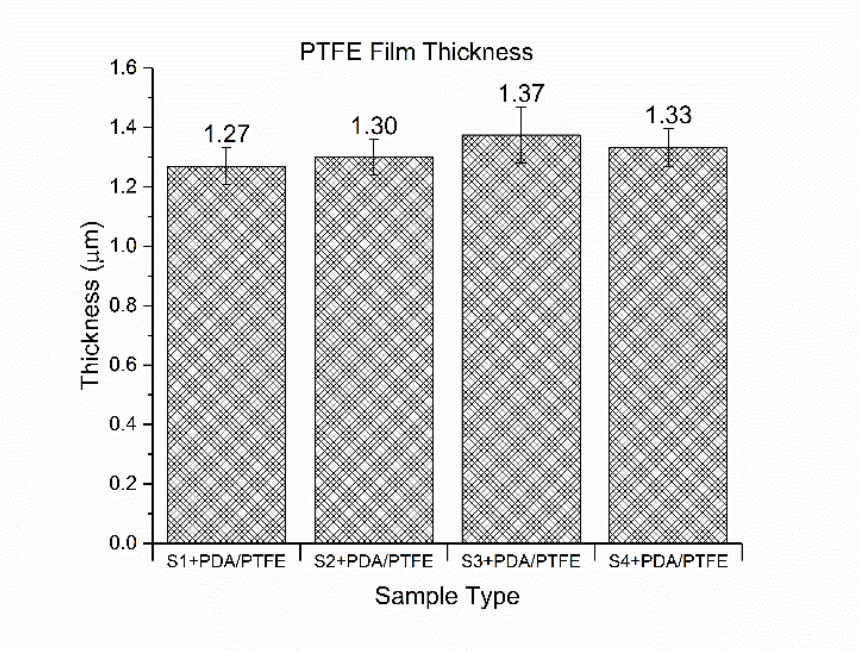

Figure 3.8. PTFE film thickness on S1-S4 substrates.

The nanoindentation tests on 60NiTi yielded an average modulus of elasticity of 89.7 GPa with standard deviation of ± 3.9 GPa and an average hardness of 8.1 GPa with standard deviation of ± 0.4 GPa. These values are on the lower end of the range of elastic modulus values found in literature (90-115 GPa) and slightly lower than published values for nanoindentation hardness of 60NiTi (9.1-9.5 GPa) [4, 11-12, 21]. The PDA/PTFE coating was measured to have an average modulus of elasticity of 1.36 GPa with a standard deviation of 0.11 GPa and an average hardness of 49.4 MPa with a standard deviation of 4.9 MPa. These measurements were also slightly lower than the values reported in literature for elastic modulus (1.5-2.5 GPa) and hardness (60-85 MPa) of PDA/PTFE coatings [16]. These slightly lower numbers of the

mechanical properties may be attributed to the differences in materials and coating fabrication or the nanoindentation processes.

3.3.2 Tribological Testing

Ball-on-plate linear reciprocating wear tests were used to evaluate the tribological properties of the PDA/PTFE coating on 60NiTi (60NiTi + PDA/PTFE) as a Si_3N_4 ball was slid against it. Three tests are run on each of the samples. There are three samples for each of the four sample variants, therefore a total of twelve samples, and a total of 36 tests run on 60NiTi + PDA/PTFE samples. Three ball-on-plate linear reciprocating wear tests were also performed on a bare 60NiTi sample that was polished to a S1 finish. These tests are used to determine tribological properties of unlubricated 60NiTi under the same testing conditions used for the coated samples. However, the failure criterion is removed, and the test is run for only five minutes due to severe wear.

The COF versus rubbing cycles is plotted in Figure 3.9 for one test on each coated sample variant. The average COF was calculated for each of the tests and the values were averaged for each sample variant. The average COF of S1 + PDA/PTFE, S2 + PDA/PTFE, S3 + PDA/PTFE, S4 + PDA/PTFE, and bare 60NiTi were 0.096, 0.098, 0.101, 0.102, and 0.731, respectively (Figure 3.10). The average COF slightly increased with the roughness on the samples coated with PDA/PTFE, but the variations were only within a few percent of 0.10. Furthermore, all S1-S4 + PDA/PTFE samples had over 85% reduction in average COF compared to the bare 60NiTi. This result proved PDA/PTFE coatings on 60NiTi were effective at reducing friction under this test condition.

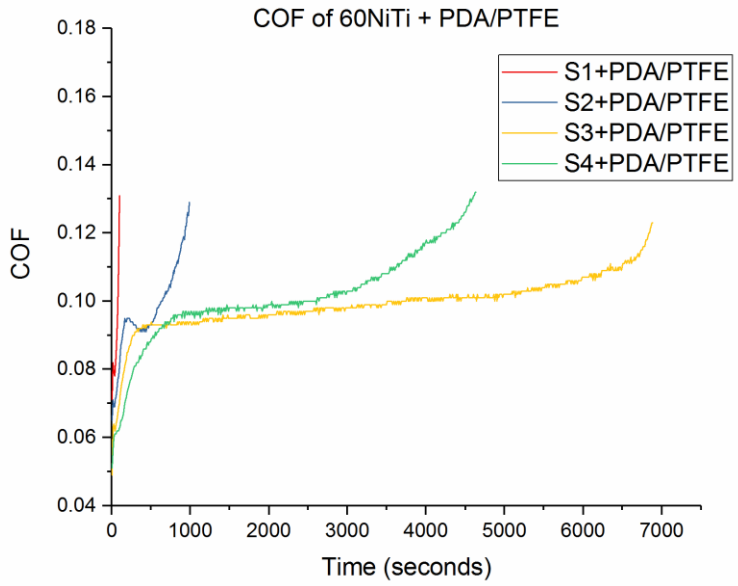

Figure 3.9. COF of S1-S4 + PDA/PTFE throughout the durability tests.

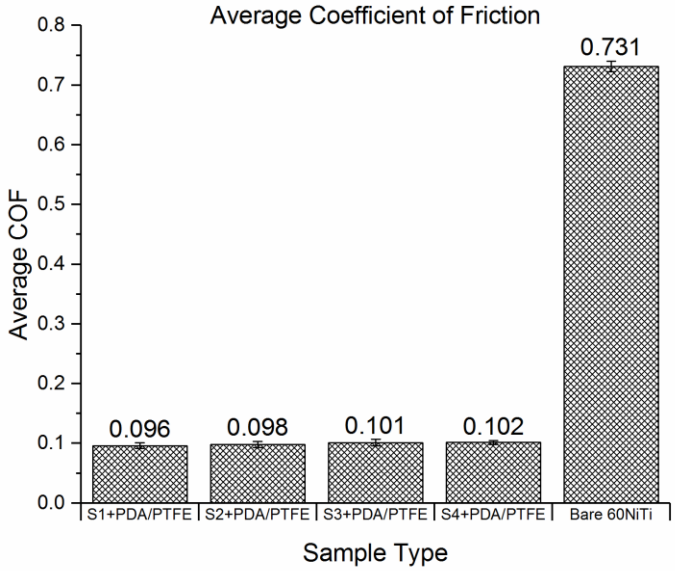

Figure 3.10. Average COF of S1-S4 + PDA/PTFE throughout durability tests.

The durability of the coatings was defined as the reciprocating cycles until the frictional force reached the value 0.7 N. The sharp rise in frictional force, and thus in COF, was caused by

the counterface ball wearing through the coating and having unlubricated contact with the 60NiTi substrate. This failure can be observed through microscopy of the wear track after the end of the durability test, as shown in Figure 3.11. A small, few-hundred-nanometers deep scratch shown in light color can be seen through the middle of the wear track. If the tests were run beyond the sharp rise in frictional force, then the COF rises to near 1.0 and eventually stabilizes around 0.7. The scratch in the substrate grows deeper and wider as time progresses and unlubricated contact between the Si_3N_4 ball and 60NiTi substrate causes severe wear.

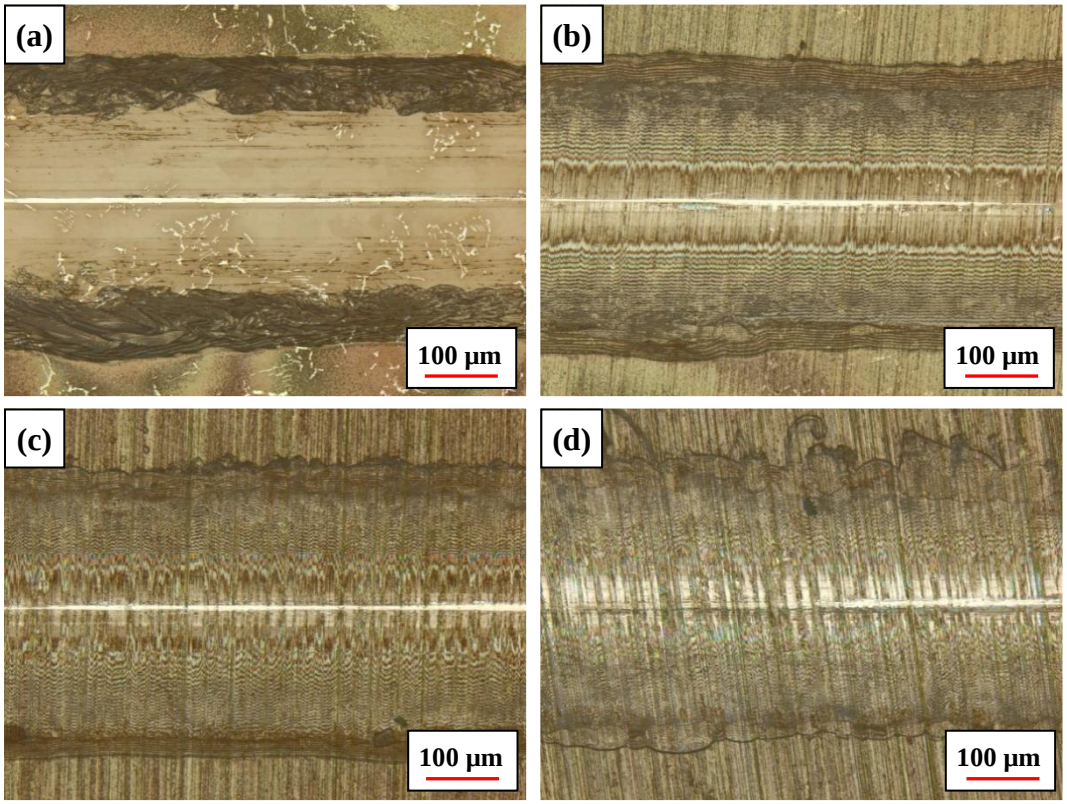

Figure 3.11. Laser scanning microscope images of the wear tracks of (a) S1 + PDA/PTFE, (b) S2 + PDA/PTFE, (c) S3 + PDA/PTFE, and (d) S4 + PDA/PTFE.

The profiles of the wear tracks (Figure 3.12) reveal differences in the wear mechanisms for coatings on substrates with different roughness. For coatings on S1 and S2, the bottoms of the wear tracks were flat, indicating that the coating had delaminated. This global removal was

caused by the substrates' surfaces being too smooth to lock the coating into place. The coating sheared away in large quantities in a short amount of time. The global removal of coating was also evidenced by the pile-up of the coating on the edge of the wear tracks in the laser-optical images in Figure 3.11. In Figure 3.11 (a), the pile-up of removed coating materials on the edge of the wear track consists of thick bands. This indicates that the coating was removed in thick layers as wear occurred. In Figure 3.11 (b), these bands are smaller in size compared to those on S1 samples, but they are much larger than those on the S3 and S4 samples (Figure 3.11 (c) and (d)). The close-together parallel lines seen in the wear tracks of S3 and S4 samples on Figure 3.11 (c) and (d) reveal a more gradual wear of the coating because the layers being removed were much thinner and more numerous. Additionally, these parallel lines are disrupted by the roughness of the substrate towards the center of the wear track. This suggests that the mechanical interlocking of the coating to the rougher substrate surfaces prevented the global removal of coating that was observed with the smoother substrate surfaces. This gradual wear of the coating was also the reason why the profiles of the wear tracks for S3 and S4 samples in Figure 3.12 conform to the shape of the counterface ball.

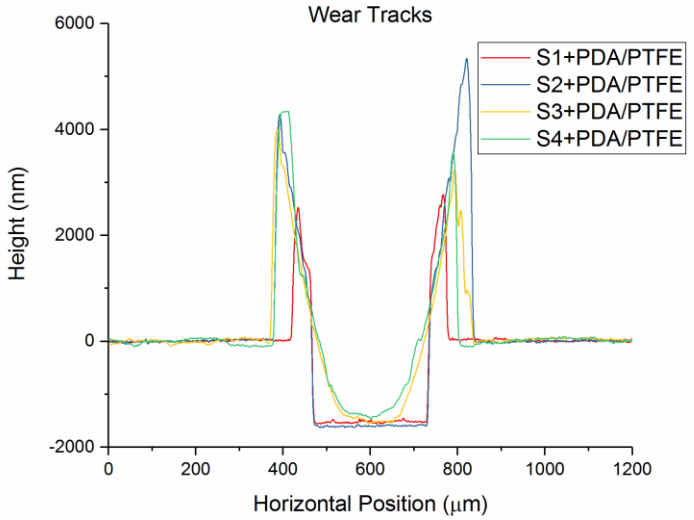

Figure 3.12. Profiles of the wear tracks of S1-S4 + PDA/PTFE samples.

The average coating durability for each sample variant is graphed in Figure 3.13. The durability tests show that the substrate surface finish had a very significant effect on the coating durability. Increasing the roughness of the substrate surface caused the coating to last for several thousand cycles rather than just a few hundred. On average, the samples with the rougher substrate surface finishes, S3 + PDA/PTFE and S4 + PDA/PTFE, had over 30 times that of the samples with the smoothest finish, S1 + PDA/PTFE. Furthermore, the S3 + PDA/PTFE tests showed that using a lapping process to flatten the peak asperities of the abraded substrate surface can further increase the durability of a PDA/PTFE coating. The S3 + PDA/PTFE samples averaged a coating durability over 1000 cycles longer than the S4 + PDA/PTFE samples, a 24.4% increase.

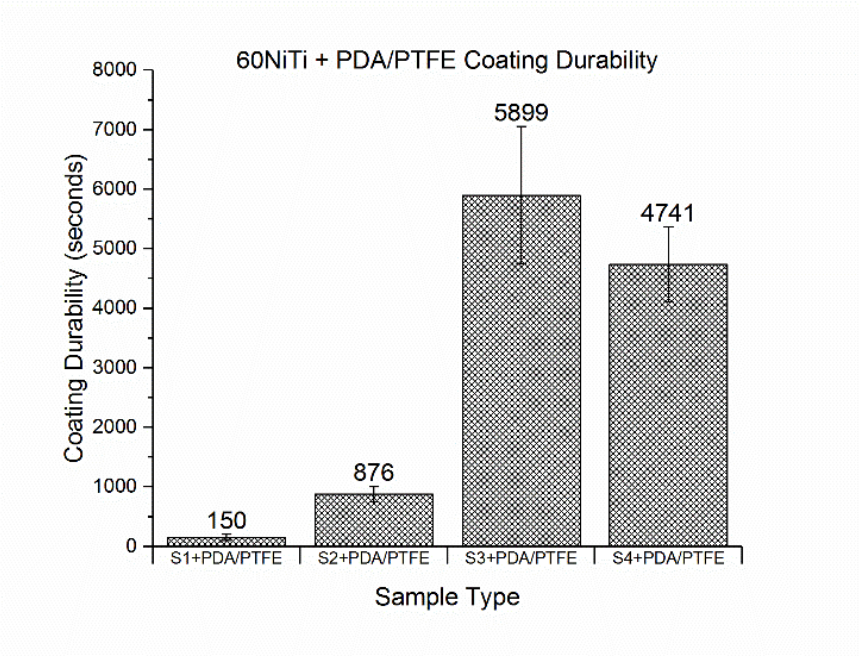

Figure 3.13. Average durability of S1-S4 + PDA/PTFE.

The greater durability of the coatings on the rougher samples was caused by grooves on the substrate surface that locked and held the PDA/PTFE coating in place, keeping the surface lubricated. Grinding 60NiTi with 320 grit sandpaper for the S3 and S4 surfaces created parallel

grooves that were a few microns in width and hundreds of nanometers in depth. The scanning electron microscope (SEM) images in Figure 3.14 show that these grooves were filled with PTFE. This is seen at the interface of the PTFE coating and the PDA-coated substrate that results from dip-coating leaving a portion of the substrate uncoated by PTFE (Figure 3.2). 3D laser scanning microscopy of the wear tracks on S3 + PDA/PTFE and S4 + PDA/PTFE after durability testing also showed these valleys were retaining PTFE (Figure 3.11) and EDS mapping was used to confirm that these grooves were filled with PTFE (Figure 3.15). In addition to the mechanical interlocking of the coating in the grooves of the rougher substrate surfaces, the added roughness also increased the surface area. This increase in surface area resulted in an increase in the adhesion between the coating and the substrate. The increase in adhesion also contributes to the longer durability of the coating on the rougher substrate surfaces.

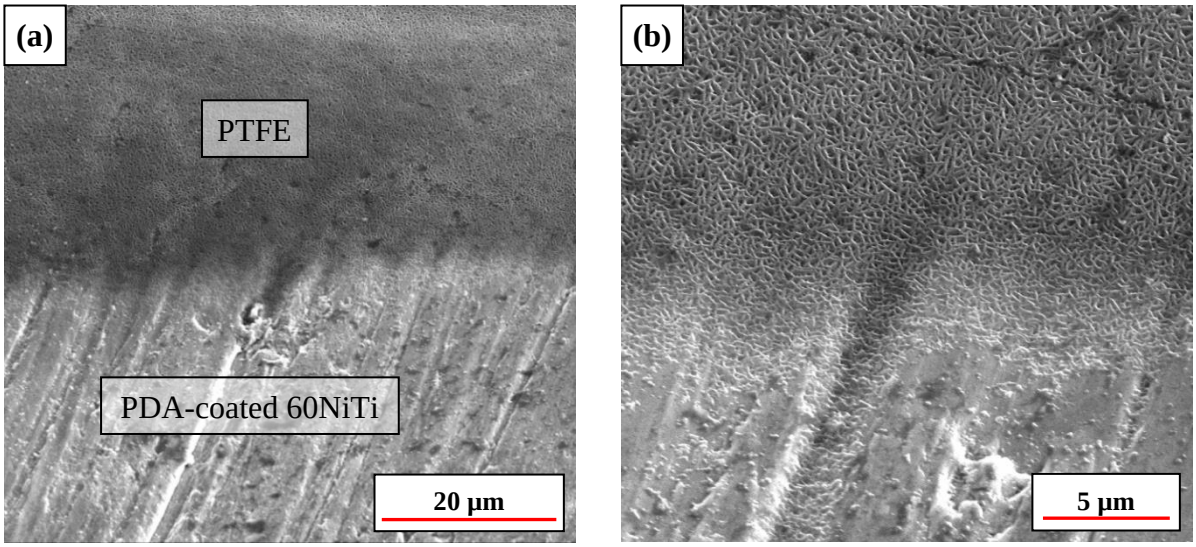

Figure 3.14. SEM images of the interface of PTFE (upper portion of images) and PDA-coated 60NiTi (lower portion of images) on S3 + PDA/PTFE (location of the interface is shown in Figure 3.3). (a) Lower magnification image and (b) higher magnification image showing a deep groove filled with PTFE.

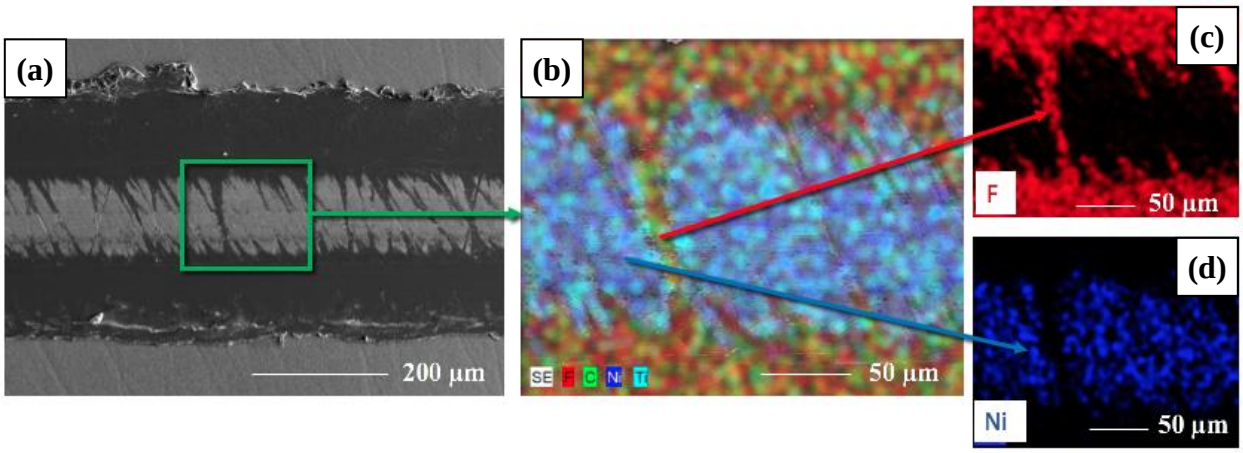

Figure 3.15. SEM image and EDS maps on the wear track of S3 + PDA/PTFE. (a) SEM image of the wear track, (b) EDS map of the inside of the wear track for F, C, Ni, and Ti, (c) EDS map of F, and (d) EDS map of Ni.

The S3 + PDA/PTFE samples outperformed the S4 + PDA/PTFE samples because the peaks of the substrate roughness on S4 samples caused localized increases in contact pressure. The S3 + PDA/PTFE samples were able to distribute contact more evenly across the plateaued areas on the substrate surface. These plateaued areas could also have been lubricated more easily by PTFE in the deep grooves spilling onto them.

The Si_3N_4 counterface balls were also imaged using the 3D scanning laser microscope after the durability tests and a transfer film was observed on the balls. The transfer film originated from the PTFE that was removed from the substrate and adhered to the counterface. This transfer film enabled the favorable rubbing of PTFE on the polymer transfer film rather than PTFE on 60NiTi. Imaging the counterface balls showed that the amount of film transferred to the counterface increased with increased roughness of the substrate surface. This can be seen in the laser scanning microscope images shown in Figure 3.16 and is another reason for the extended durability of the coating on the rougher substrate surfaces.

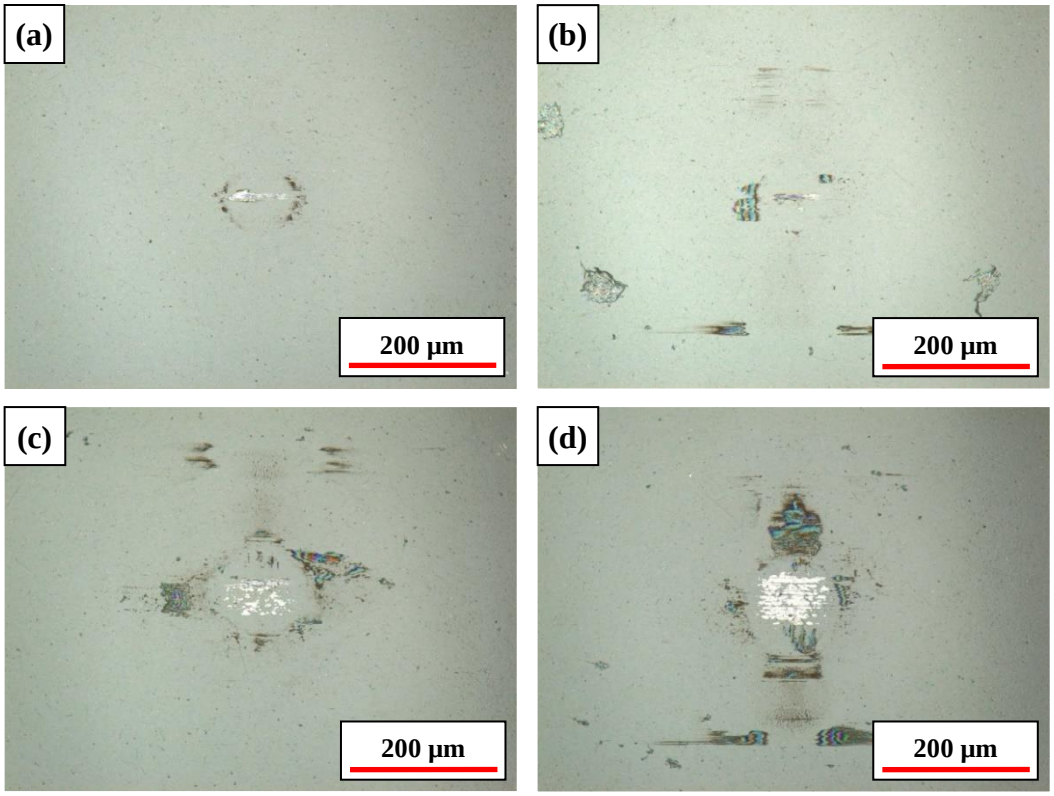

Figure 3.16. 3D laser scanning microscopy images of the counterface balls after wear tested with (a) S1 + PDA/PTFE, (b) S2 + PDA/PTFE, (c) S3 + PDA/PTFE, and (d) S4 + PDA/PTFE counterfaces.

Carbon and fluorine signatures from EDS mapping are used to verify that the transfer film originates from PTFE (Figure 3.17). The size of the wear particles was the primary reason that the amount of coating transferred to the counterface increased with increased roughness of the substrate surface. For the samples with the smoother substrate surfaces, the coating delaminated in large layers, which were difficult to adhere to the counterface because of their size and weight. However, for the rougher substrate samples, the wear particles were much smaller because the mechanical interlocking of the coating and the substrate resisted the global delamination of the coating. The roughness of the substrate broke up the wear debris into smaller particles that could transfer to the counterface more easily and adhere to the counterface better.

The counterface balls also had small amounts of 60NiTi material transfer to them. This is shown in the EDS mapping in Figure 3.18, where the concentration of Ni is seen to spike in the bright white regions of transferred material in the middle of the counterface ball. This transferred film originating from the 60NiTi substrate can also be seen in the laser-optical images in Figure 3.16. It is the bright white material that is adhered to the center of the contact area on the counterface balls. The amount of this film transferred to the balls also increased with the roughness of the substrate. On the roughest substrate surfaces, S4, the removal of the roughness peaks during sliding accounts for the significantly larger amount of 60NiTi-based film transferred to the counterface ball.

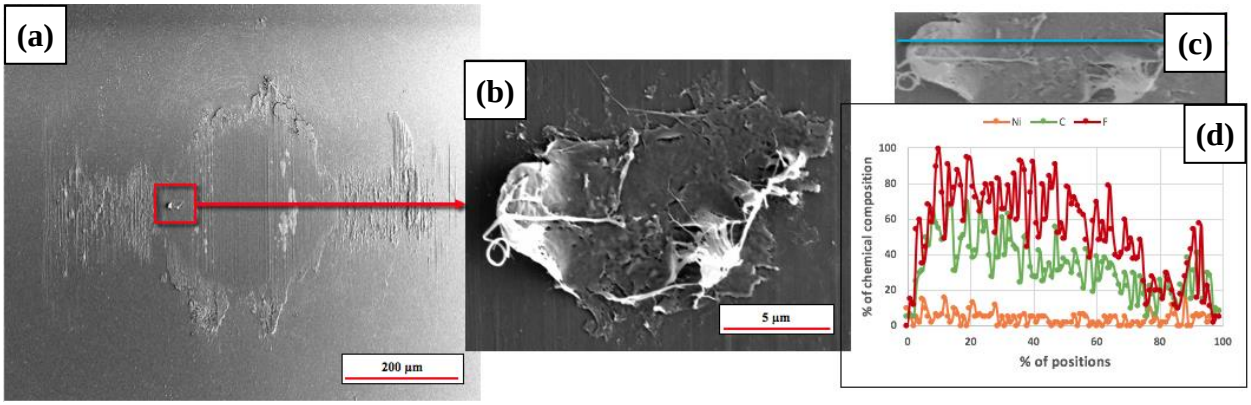

Figure 3.17. SEM imaging and EDS mapping of counterface ball after durability test on S3 + PDA/PTFE. (a) SEM image of the counterface ball, (b) magnified SEM image of transfer film on the counterface ball, (c) EDS line profile across the transfer film, and (d) EDS plot of Ni, C, and F along the line showing the presence of the PTFE elements.

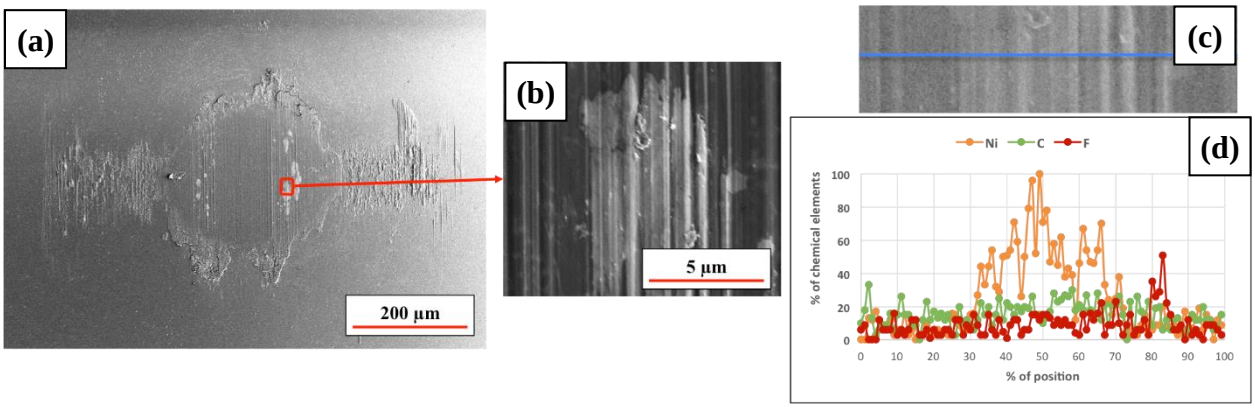

Figure 3.18. SEM imaging and EDS mapping of counterface ball after durability test on S3 + PDA/PTFE. (a) SEM image of the counterface ball, (b) magnified SEM image of transfer film on the counterface ball, (c) EDS line profile across the transfer film, and (d) EDS plot of Ni, C, and F along the line showing the presence of 60NiTi element.

3.4 Conclusions

This study demonstrated the effectiveness of PDA/PTFE solid lubricant coatings on 60NiTi. The 1.5-µm thick coating reduced the COF between Si_3N_4 and 60NiTi over 85% and provided sustained lubrication for thousands of cycles of scratching with a 6.35 mm diameter ball at a 2N load (615 MPa of estimated Hertzian contact pressure). Additionally, replicable procedures were developed to create four different 60NiTi substrate surface finishes of varying roughness and features. Rougher substrate surface finishes were found to increase coating durability over 30 times compared to the smoothest substrates, and secondary polishing steps were found to further improve coating durability over 24%. The valleys of the rougher substrate surfaces were found to mechanically lock and retain PTFE and increase the interface area, enabling a prolonged supply of effective dry lubrication for 60NiTi. The samples with rougher substrate surfaces were also found to deposit a greater amount of transfer film onto the counterface balls, which also contributed to the enhanced performance. For these reasons, the

combination of S3 substrate roughness and the PDA/PTFE coating showed the greatest potential to provide solid lubrication for 60NiTi applications.

3.5 Acknowledgements

We thank the National Aeronautics and Space Administration (NASA) for support under NASA Award No: 80NSSC17M0020 and Dr. Adam Howard for serving as our NASA technical contact. We also thank Dr. Christopher DellaCorte at the NASA Glenn Research Center for providing the 60NiTi samples and the helpful input on the roughness parameter range to use.

3.6 References

[1] Buehler, W.J., Gilfrich, J.V., and Wiley, R.C. (1963), “Effect of Low-Temperature Phase Changes on the Mechanical Properties of Alloys near Composition TiNi,” Journal of Applied Physics, 34, 5, pp. 1475-1477.

[2] DellaCorte, C. (2018), “Ni-Ti Next Generation Bearings for Space Applications,” Proceedings of the Schaeffler International Bearing Meeting, Herzogenaurach, Germany, January 2018.

[3] DellaCorte, C. and Wozniak, W.A. (2012), “Design and Manufacturing Considerations for Shockproof and Corrosion-Immune Superelastic Nickel-Titanium Bearings for a Space Station Application,” NASA/TM-2012-216015.

[4] Neupane, R. and Farhat, Z. (2015), "Wear Resistance and Indentation Behavior of Equiatomic Superelastic TiNi and 60NiTi." Materials Sciences and Applications, 6, 7, pp. 694-706.

[5] Pepper, S. V. (2009), "Nitinol 60 as a Material for Spacecraft Triboelements," 13th European Space Mechanisms and Tribology Symposium - ESMATS 13 Conference, Vienna, Austria, September 2009.

[6] Stanford, M.K. (2015), “Hot Isostatic Pressing of 60-NITINOL,” NASA/TM—2015-218884

[7] DellaCorte, C. (2017), “NiTi Alloys: New Materials that enable Shockproof, Corrosion Immune Bearings,” STLE Section Meeting, Canton, Ohio, February 2017.

[8] DellaCorte, C., Thomas, F., and Leak, O.A. (2015), “Tribological Evaluation of Candidate Gear Materials Operating under Light Loads in Highly Humid Conditions,” NASA/TM—2015-218896.

[9] DellaCorte, C. and Jefferson, M. (2015), “60NiTi Intermetallic Material Evaluation for Lightweight and Corrosion Resistant Spherical Sliding Bearings for Aerospace Applications (Report on NASA-Kamatics SAA3–1288),” NASA/TM—2015-218723.

[10] DellaCorte, C., Noebe, R.D., Stanford, M.K., and Padula, S.A. (2011), “Resilient and Corrosion-Proof Rolling Element Bearings Made From Superelastic Ni-Ti Alloys for Aerospace Mechanism Applications,” NASA/TM-2011-217105.

[11] Khanlari, K, Ramezani, M., Kelly, P., Cao, P., and Neitzert, T. (2018), “Reciprocating Sliding Wear Behavior of 60NiTi as Compared to 440C Steel Under Lubricated and Unlubricated Conditions,” Tribology Transactions, 61, 6, pp. 991-1002.

[12] Khanlari, K., Ramezani, M., & Kelly, P. (2018), “60NiTi: A Review of Recent Research Findings, Potential for Structural and Mechanical Applications, and Areas of Continued Investigations,” Transactions of the Indian Institute of Metals, 71, 4, pp. 781-799.

[13] Nishimura, M., and Suzuki, M. (1999), “Solid-Lubricated Ball Bearings for Use in a Vacuum - State-of- the-Art,” Tribology International, 32, 11, pp. 637-647.

[14] Beckford, S., and Zou, M. (2014), “Wear Resistant PTFE Thin Film Enabled by a Polydopamine Adhesive Layer,” Applied Surface Science, 292, pp. 350-356.

[15] Haeshin, L., “Bioadhesion of Mussels and Geckos: Molecular Mechanics, Surface Chemistry, and Nanoadhesives,” Doctoral Dissertation 2008: Northwestern University, Evanston, Illinois.

[16] Beckford, S., and Zou, M. (2016), "The Effects of Graphite Filler on the Tribological Properties of Polydopamine/PTFE Coatings," Tribology Letters, 64, 3, pp. 42-53.

[17] Beckford, S., Wang, Y.A., and Zou, M. (2011), “Wear-Resistant PTFE/SiO2 Nanoparticle Composite Films,” Tribology Transactions, 54, 6, pp. 849-858.

[18] Beckford, S., Cai, J., Chen, J., and Zou, M. (2014), “Use of Au Nanoparticle-Filled PTFE Films to Produce Low-Friction and Low-Wear Surface Coatings,” Tribology Letters, 56, 2, pp. 223- 230.

[19] Beckford, S., Mathurin, L., Chen, J., and Zou, M. (2015) "The Influence of Cu Nanoparticles on the Tribological Properties of Polydopamine/PTFE + Cu Films," Tribology Letters, 59, 1, pp. 1-9.

[20] Jiaxin, Y., Tao, B., Sun, W., Haidar, D.R., Alam, K.I., Liu, K., Burris, D.L. (2018) “The Competing Effects of Counterface Peaks and Valleys on the Wear and Transfer of Ultra-Low Wear Alumina-PTFE,” Tribology Letters, 66, 12, pp. 1-14.

[21] DellaCorte, C., Howard, S.A., Fransua, T., and Stanford, M.K. (2017), “Microstructural and Material Quality Effects on Rolling Contact Fatigue of Highly Elastic Intermetallic NiTi Ball Bearings,” NASA/TM—2017- 219466.

CHAPTER 4

MICROSCALE FRICTION AND DEFORMATION BEHAVIOR OF POLYDOPAMINE (PDA)/POLYTETRAFLUOROETHYLENE (PTFE)-COATED 60NITI FROM NANOSCRATCH TESTS

Abstract

The scratch behavior of polydopamine (PDA)/polytetrafluoroethylene (PTFE) coatings has traditionally been studied using macro-scale tribometers. However, in this study, a nanoindenter is used to scratch PDA/PTFE coatings on 60NiTi substrate to investigate the nanoscale deformation behavior and failure mechanisms of this coating under various scratch loads. Nanoscratch tests were also performed on the substrate coated only with the adhesive underlayer to study the behavior of PDA under various scratch loads. Scanning electron microscope imaging of the scratches provided further insights to the coating scratch deformation behavior. The study revealed the PDA/PTFE coating failure is strongly correlated with the removal of the PDA particles in the underlayer. The findings also suggest that the compaction of the thin PDA/PTFE coatings could be the main reason for the previously reported large initial wear depth in macro-scale tribology studies.

4.1 Introduction

NiTiNOL 60, or 60NiTi, has drawn significant attention as an advanced material for bearing and gear applications over the last decade [1-2]. The National Aeronautics and Space Administration (NASA) has been investigating 60NiTi as a candidate material for bearing and gear components on the International Space Station (ISS) [3-7]. Its combination of high

hardness, low elastic modulus, and extreme corrosion resistance have made it a promising candidate material for these applications. However, 60NiTi has a high coefficient of friction (COF) in unlubricated conditions and the ISS applications require the use of a solid lubricant.

Polytetrafluoroethylene (PTFE) is a promising solid lubricant for this application. Thin PTFE coatings with a polydopamine (PDA) adhesive underlayer have been shown by Beckford et al. to reduce friction and wear of stainless steel substrates without the need to modify the substrate surfaces, which is important for bearing applications [8]. These PDA/PTFE coatings utilize bio-inspired PDA adhesive underlayer of about 120 nm thickness to improve the adhesion between a thin PTFE coating and the smooth stainless steel substrates. The PDA/PTFE coatings were found to withstand approximately 500 times more rubbing cycles than PTFE film alone [8]. Previous studies have shown that the PDA/PTFE coatings also significantly improved the PTFE coating durability on 60NiTi [9]. Additionally, increasing substrate roughness [9], adding graphite particles [10], and increasing the coating thickness [11] further drastically improved the coating durability. Furthermore, much better durability has been demonstrated on 60NiTi [9] than on stainless steel substrates [8], suggesting the promise of using PDA/PTFE coatings for 60NiTi substrate for improving tribological performance in ISS applications.

Friction, deformation, and wear behavior of PDA/PTFE and PTFE and micro/nanoparticle composite coatings have been studied through macroscale scratch and wear testing using tribometers with bearing balls as the counterface [8-18]. This method is effective for computing a quantitative durability of the coating in ball-on-disk configurations that mimic real applications. These studies revealed PDA/PTFE to be an effective solid lubricant coating on

60NiTi that drastically reduces the coefficient of friction (COF) and is durable for thousands of rubbing cycles at a contact pressure of 615 MPa (neglecting the effects of the soft, thin coating) [9-11]. However, the coating thickness was found to diminish quickly after the first few rubbing cycles and the durability of the coating was attributed to a robust and well-adhered thin layer of coating at the substrate interface. Previous studies hypothesized from progressive testing that the early reduction in coating thickness could be attributed to delamination [18] and removal [8] of most of the PTFE coating before the counterface reached a more resilient layer of PTFE at the PDA/PTFE interface. However, only plastic deformation of the coating was observed prior to delamination and failure during linear increasing macro-scale scratch tests [10,18]. Therefore, the mechanisms that contributed to the early reduction in coating thickness were still not fully understood. This is because these macroscale tribological tests lacked microscale control of the applied normal load and the resulting PDA/PTFE coating and PDA adhesive underlayer deformation could not be observed at the nanoscale.

In this study, a nanoindenter was used to investigate the nanoscale deformation of 60NiTi and the scratch behavior of 60NiTi, 60NiTi/PDA/PTFE, and 60NiTi/PDA. The scratches were imaged using scanning electron microscopy (SEM). We hypothesize that the nanoindentation tip can mimic a microscale asperity on the counter surface and bring about high contact pressure, which can accelerate the coating failure during the nanoscratch testing. Nanoindenter scratch tests enabled the generation and detection of nanoscale deformation during scratches through the precise control of applied normal load, which, when combined with post imaging and analysis of the microstructure of the scratches using SEM, led to a more thorough understanding of the coating frictional deformation behavior and failure mechanisms.

4.2 Experimental Methods

4.2.1 Sample Preparation

60NiTi samples with dimensions 25.4 × 25.4 × 2 mm were supplied by the NASA Glenn Research Center in a hardened condition. The hardening was achieved through a heat-treatment process consisting of a 2-hour soak at 1050 °C followed by a furnace cool to 900 °C and then a rapid water quench. The samples were then aged at 400 °C for an hour. This process has been shown to produce a microstructure containing a matrix of NiTi with nanoscale Ni_4Ti_3 precipitates throughout [19,20]. A secondary Ni_3Ti phase is dispersed throughout the microstructure as micro-scale precipitates.

The surfaces of the 60NiTi samples were ground flat and polished to less than 20 nm of average roughness (R_a) using a grinder-polisher machine (Buehler EcoMet 300 Polisher, Buehler, Lake Bluff, IL) and a 6-lb load. 320-grit sandpaper was used to grind the samples flat for 9 minutes. Then, the samples were lapped with 9-μm polycrystalline diamond polishing suspension for 8 minutes and, lastly, they were polished using a 60-nm colloidal silica suspension for 5 minutes. After polishing, the samples were cleaned by sonicating in acetone, isopropyl alcohol, 1.0% detergent, and deionized water. Subsequently, they were dried with nitrogen gas.

PDA deposition on the polished 60NiTi surfaces took place in a 700 mL solution of deionized (DI) water that was buffered to a pH of 8.5 by adding 0.848 g of tris(hydroxymethyl)aminomethane (T1503, Sigma Aldrich, St. Louis, MO, USA). The solution was heated to a temperature of 60 °C and the temperature was held constant throughout the

deposition process. Once the temperature and pH were stable and at the desired values, 1.4 grams of dopamine hydrochloride (H8502, Sigma Aldrich, St. Louis, MO, USA) was added to the solution and PDA polymerized on the surface for 60 minutes. To speed up the rate of deposition, the bath was rocked on a rocking-shaker at 25 rpm and a rocking angle of 10° throughout the process. After 60 minutes of deposition, the samples were removed from the bath, rinsed with DI water, and dried with nitrogen gas.

A dip-coater (KSV DC, KSV NIMA, USA) was used to deposit the PTFE coating onto the PDA adhesive underlayer by dipping the samples into an aqueous dispersion of PTFE nanoparticles (Teflon Dispersion DISP30, Fuel Cell Earth, MA, USA). An insertion and withdrawal rate of 10 mm/min and a soak time of twenty seconds was used. A three-stage heat treatment process was used to remove water and surfactants from the coating and to sinter the PTFE particles, respectively. The first step of the process was to heat the samples on a hot plate at 120 °C for 3 minutes. Then, the samples are heated in a furnace for 4 minutes at 300 °C and, lastly, the nanoparticles are sintered together in the furnace during heating to 372 °C for 4 minutes. The three heat treatment steps are performed immediately after one another. A portion of the PDA underlayer remains exposed on one side of the sample surface due to the sample not being fully submerged in the PTFE suspension during the dip coating process. This exposed interface of PDA and PTFE was used to measure the thickness of the PTFE coating through contact profilometry (Dektak 150, Veeco, Plainview, NY, USA). The thickness was found to be approximately 1.6 μm.

4.2.2 Sample Characterization

Sample surfaces of the 60NiTi, 60NiTi coated with PDA (60NiTi/PDA), and 60NiTi coated with PDA and then PTFE (60NiTi/PDA/PTFE) were imaged using scanning electron microscopy (SEM) (VEGA3, Tescan, Brno, Czech Republic). Gold was sputtered on the 60NiTi/PDA and 60NiTi/PDA/PTFE sample surfaces prior to SEM imaging to reduce charging effects and enable higher resolution imaging. A diamond-tipped scribe was used to define the locations that scratches were to be performed and these marks served as fiducial marks for locating the scratches during SEM imaging.

4.2.3 Nanoindentation

A nanoindenter (TriboIndenter, Hysitron, Minneapolis, MN, USA) was used to perform load-controlled indentations on 60NiTi and 60NiTi/PDA/PTFE and load-controlled scratch tests on 60NiTi, 60NiTi/PDA, and 60NiTi/PDA/PTFE. A diamond spheroconical tip with 5-μm tip radius was used. Diamond is the standard tip material for nanoindentation probes.

Load-controlled indentations were performed on the 60NiTi sample using a variety of maximum loads. Lower-load indentations were performed from 100-500 μN and higher-load indentations were performed from 1000-8000 μN. Loading and unloading rates of 20 μN/s were used on the lower-load indentations and rates of 200 μN/s were used for the higher-load indentations. A five-second hold time was used at the maximum load of each indent to allow for creep and thermal drift. A predicted load-displacement relationship was determined using the Hertzian contact equations and was used for comparison with the experimental results. The

following equation was used to determine relationship between the applied normal load, W, and the normal displacement, δ, using the effective radius, R, and the composite modulus, E^*:

$$\delta = \left(\frac{9W^2}{16RE^{*2}}\right)^{1/3} \quad (1)$$

where

$$\frac{1}{R} = \frac{1}{R_1} + \frac{1}{R_2} \quad (2)$$

and

$$\frac{1}{E^*} = \frac{1 - {v_1}^2}{E_1} + \frac{1 - {v_2}^2}{E_2} \quad (3)$$

The parameters E and v are Young's modulus of elasticity and the Poisson's ratio, respectively, and the subscripts 1 and 2 refer to the two contacting bodies [21]. The E and v values used for the diamond indenter and 60NiTi are shown in Table 4.1.

Table 4.1. E and v values used in the Hertzian contact equations.

Material	***E* (GPa)**	***v***
Diamond Indenter	1141	0.07
60NiTi	89.7	0.34

4.2.4 Scratch Testing

Load-controlled scratch tests were performed at maximum loads of 25, 50, 100, 200, 500, 1000, 2000, 3000, 4000, 5000, 6000, 7000, and 8000 μN on each of the samples. Five scratches were performed at each load on each sample. The scratch length was 8 μm and it was performed at a constant speed over a 30 s interval. The nanoindenter used two three-plate capacitive force-

displacement transducers to measure the normal and lateral forces throughout the scratch. The COF was calculated as the ratio of the lateral force to the normal force during scratch, and the average COF across the entire scratch length was reported.

The entire scratch process takes 70 s. First, the tip contacts the sample at the location that will be the center of the scratch. During the first 10 s, the tip moves -4 μm at a minimal load to the starting position for the scratch. The topography of the surface is traced during this segment and it can be used to correct the scratch deformation for sample tilt. From t = 10 s until t = 20 s, the load is increased at a constant rate until the scratch load is reached. The tip does not move laterally during this loading segment. At t = 20 s the constant load scratch begins, and the tip moves laterally for 8 μm over the next 30 s (until t = 50 s). Then, the load is steadily removed from t = 50 s to t = 60 s without lateral tip movement; and finally, the tip returns to the starting location with a minimal load from t = 60 s to t = 70 s. After the scratches were performed on each of the samples, they were imaged using SEM to observe the deformation and identify the failure mechanisms.

Three additional 1000 μN scratches were performed repeatedly at the same location to investigate the behavior of the coating after it had been deformed and compressed by an earlier scratch. The three scratches were carried out according to the same scratching procedure previously described.

4.3 Results and Discussion

4.3.1 Surface Characterizations

SEM images of the sample surfaces are shown in Figure 4.1. The 60NiTi surface (Figure 4.1 (a) and (b)) consists of multiple phases of material. A previous study [22] showed that the microstructure of the hardened 60NiTi surface predominantly consists of a NiTi matrix with nanoscale Ni_4Ti_3 precipitates dispersed throughout it, but the Ni_4Ti_3 precipitates are not visible at the magnification of the images in Figure 4.1 (a) and (b). However, microscale Ni_3Ti precipitates appear in Figure 4.1 (a) and (b) as bright globular and needle-like precipitates. Additionally, micron-scale oxide particles appear are small, darker particles that are randomly distributed across the 60NiTi surface.

The surface of the 60NiTi/PDA sample is shown in the SEM images in Figure 4.1 (c) and (d). The PDA deposits on the surface as agglomerates that are hundreds of nanometers in size. These PDA agglomerates add roughness to the surface, which aids in securing the PTFE coating to the sample. The surface of PDA/PTFE-coated 60NiTi is shown in Figure 4.1 (e) and (f). The PTFE coating consists of interwoven PTFE fibrils that form a porous network. The fibrils form as PTFE nanoparticles are sintered together during the heat treatment process.

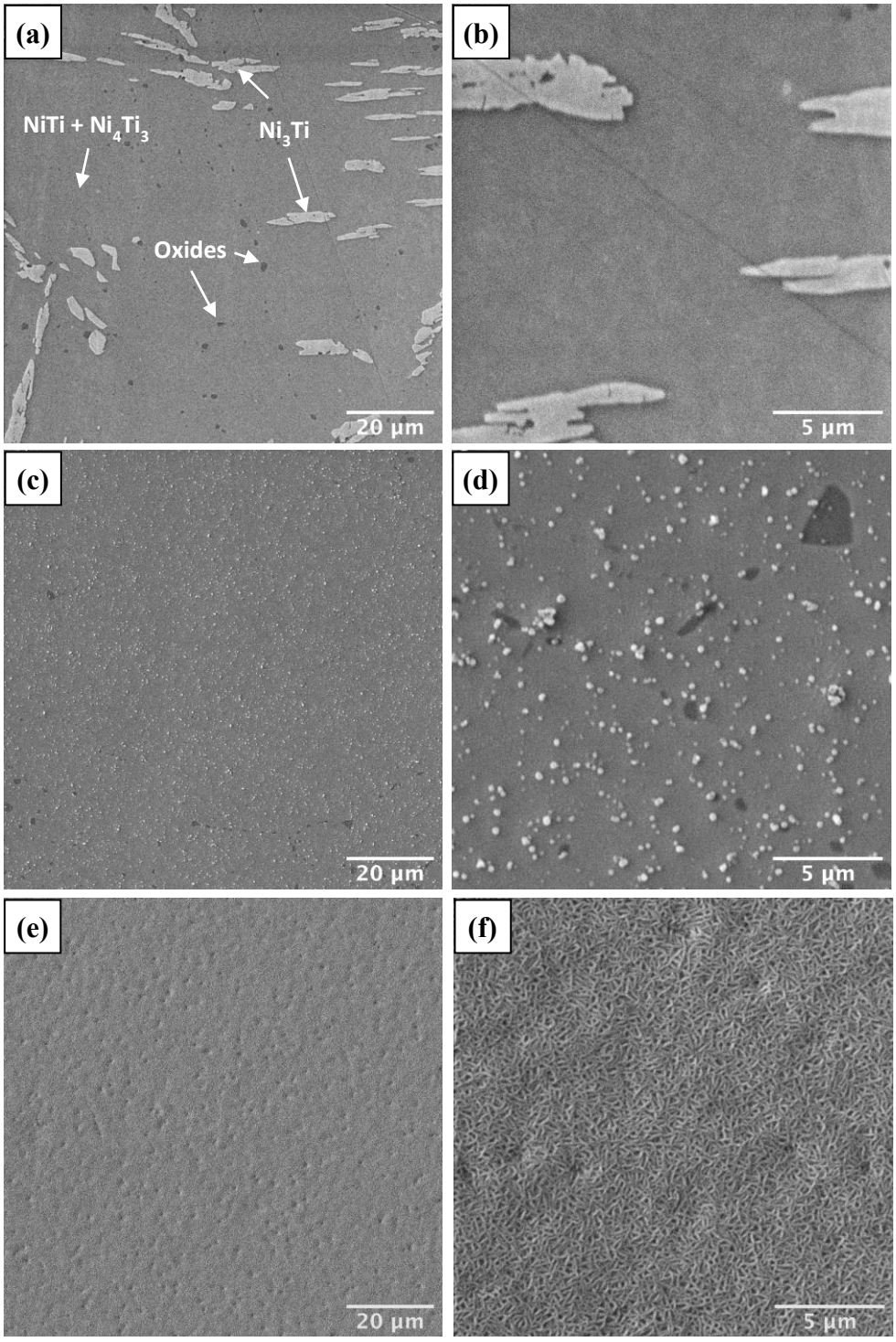

Figure 4.1. SEM images of the sample surfaces: (a) lower-mag 60NiTi, (b) higher-mag 60NiTi, (c) lower-mag 60NiTi/PDA, (d) higher-mag 60NiTi/PDA, (e) lower-mag 60NiTi/PDA/PTFE, and (f) higher-mag 60NiTi/PDA/PTFE.

4.3.2 Nanoindentation

The load-displacement curves from indentations on 60NiTi using the spheroconical diamond tip with a 5 μm radius are plotted in Figure 4.2. Curves labeled "Hertzian Prediction" are included and represent the predicted load-displacement relationship based on Hertzian contact theory according to Equation (1) using the input parameters shown in Table 4.1. Figure 4.2 (a) shows the curves for indentations to maximum loads of 100, 200, 300, 400, and 500 μN. The maximum loads for the indentations shown in Figure 4.2 (b) were 1000, 2000, 3000, 4000, 5000, 6000, 7000, and 8000 μN. At the lower load indentations shown in Figure 4.2 (a), the curves have a very similar trend to the "Hertzian Prediction" curve. The predicted curve continues to overlap the indentation curves in Figure 4.2 (b) until approximately 1000 μN, which corresponds to a Hertzian contact pressure of 4.07 GPa. This prediction is limited to elastic deformation of the bodies, so a comparison is not applicable at the larger indentation loads in Figure 4.2 (b). During larger load indentations, slight hysteresis was observed which indicates that the deformation was not fully elastic. The predicted limit of elastic deformation for 60NiTi (4.07 GPa) aligns with macro-scale indentation resistance tests on 60NiTi [23]. Indentations on polished 60NiTi with a 12.7 mm diameter Si_3N_4 ball did not produce detectable dents at a peak stress of 3.98 GPa, but a peak stress of 4.29 GPa produced a 0.06 μm deep dent [23].

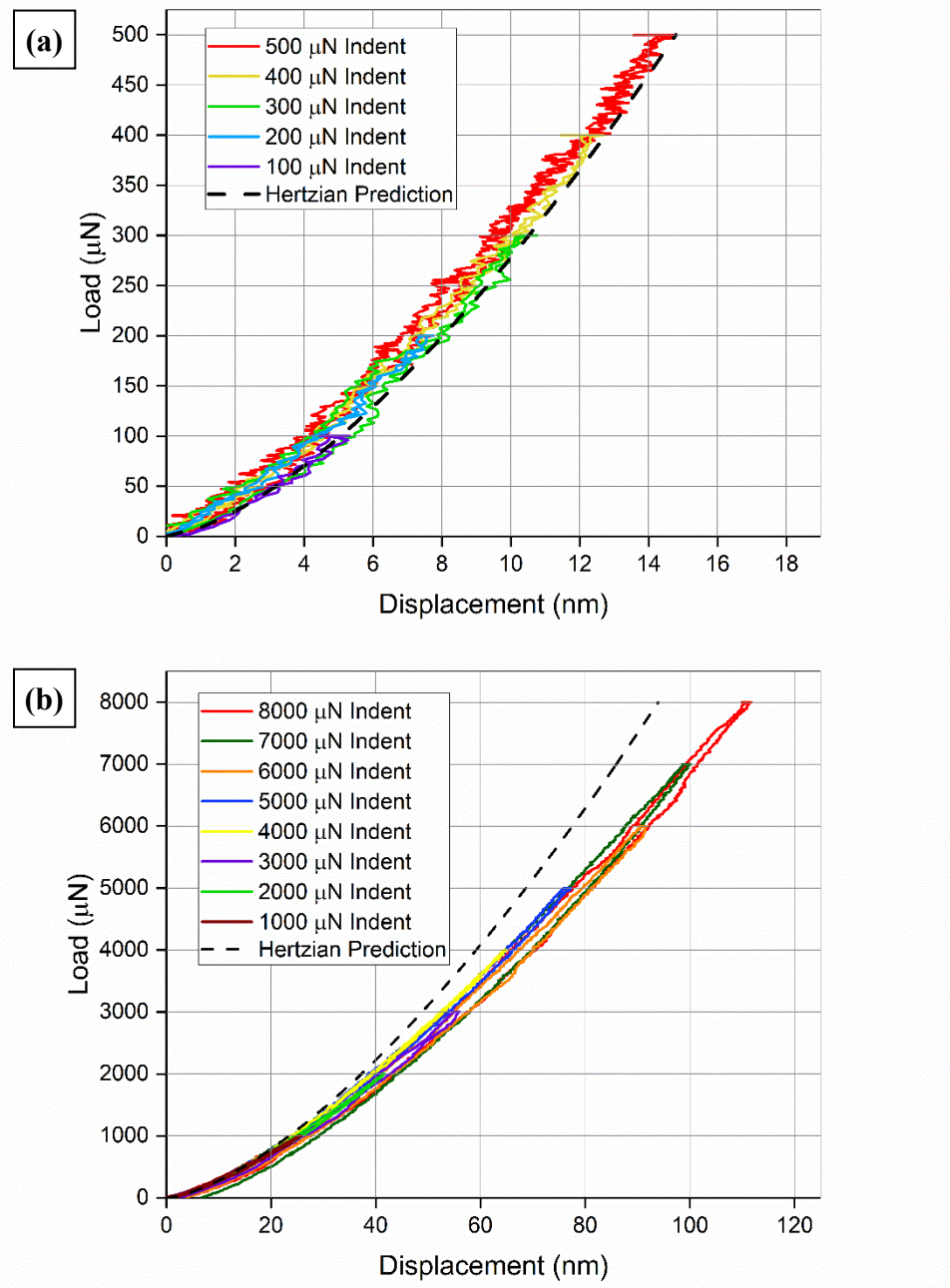

Figure 4.2. Load-displacement curves for indentations on 60NiTi at maximum loads from (a) 100-500 μN and (b) 1000-8000 μN using the diamond indenter.

4.3.3 Scratching of 60NiTi

Figure 4.3 shows a plot of the average COF versus normal force for five scratches with the diamond indenter on each of the samples at loads of 25, 50, 100, 200, 500, 1000, 2000, 3000, 4000, 5000, 6000, 7000, and 8000 μN. For 60NiTi, the average COF was 0.26 at 25 μN, but as the load increased, the COF dropped quickly and approached 0.05 at the largest loads. Although 60NiTi typically has a high COF in dry conditions, the polycrystalline diamond tip is a material with low COF and was a reason for the low COF measurements in these tests. The higher COF at low loads was caused by the influence of the adhesive forces. At higher normal loads, the adhesive forces become insignificant compared to the applied normal loads.

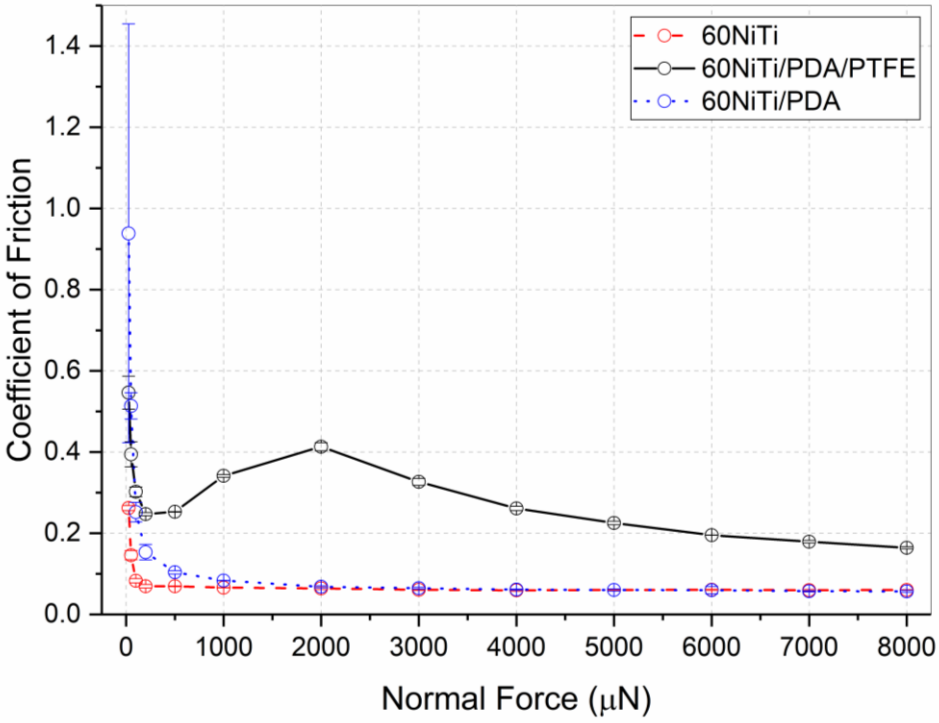

Figure 4.3. Coefficient of friction vs. normal force for scratches on 60NiTi, 60NiTi/PDA/PTFE, and 60NiTi/PDA using the diamond indenter.

4.3.4 Scratching of 60NiTi/PDA/PTFE

The COF of the diamond indenter scratches of 60NiTi/PDA/PTFE is also shown in Figure 4.3, and this sample exhibited interesting oscillations in COF as the load varied. The COF was highest at the lowest load because of the adhesive forces, but it dropped near 0.25 at loads of 200 and 500 μN. From loads ranging from 500 to 2000 μN the COF rose to slightly more than 0.4 before it dropped each time the load was increased from 2000 to 8000 μN. This relationship between the COF and normal force can be explained through analysis of the scratch displacement and observing the scratch deformation using SEM.

The plot of normal displacement versus time for the scratches on 60NiTi/PDA/PTFE using the diamond indenter is shown in Figure 4.4. The loading profile is represented at the top of the plot. The time from t = 10 s until t = 20 s corresponds to the loading portion of the scratch method where the tip is not moving laterally. The intended scratch load is reached at t = 20 s and then the tip moves laterally at a constant load for 8 μm from t = 20 s until t = 50 s. Then, unloading occurs from t = 50 s until t = 60 s without lateral tip movement.

Figure 4.4 shows that the PDA/PTFE coating deforms during the loading segment and then additional deformation occurs during the constant load scratch. The amount of deformation increases as the scratch load is increased. The SEM images in Figure 4.5 show how the coating deforms during these scratches (the scratch direction was from the bottom to the top of each image). At the lowest scratch loads of 25 and 50 μN, only the high asperities are deformed, and the coating remains porous inside of the scratch area. At loads up to 1000 μN, the scratch

plastically deformed the coating, and the coating was compressed. The morphology of the coating changes from being needle-like and porous to uniform and solid as the load is increased.

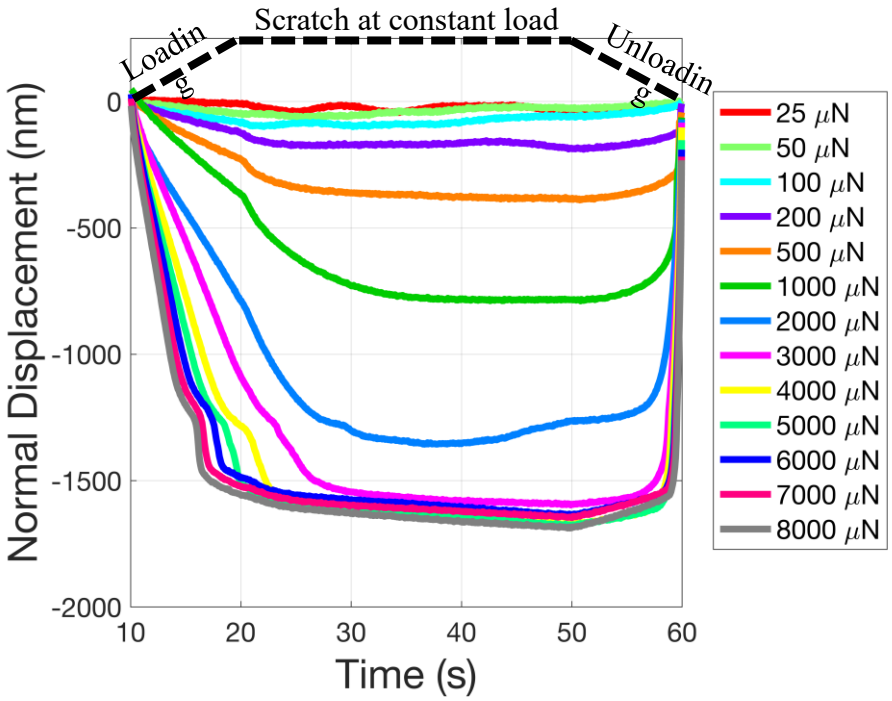

Figure 4.4. Normal displacement vs. time for the scratches performed on 60NiTi/PDA/PTFE using the diamond indenter.

During the scratch at a constant load of 2000 μN, a tear in the compacted coating can be seen (Figure 4.5 (g)), and strands of PTFE bridge the gap across this tear and run in the direction of the scratch. At scratch loads of 3000 μN and greater, the tear in the compressed coating becomes larger and the substrate is clearly exposed. Figure 4.4 shows that the normal displacement during scratch at 3000 μN reached around 1600 nm, which is approximately the coating thickness. Beyond this load, the amount of deformation did not change much. Since 3000 μN can only cause 60NiTi to deform about 55 nm, as shown in Figure 4.2, it can be concluded that the 1600 nm of measured normal displacement was almost entirely from the deformation of

the coating. Since the coating thickness is about 1600 nm, it can be concluded that the tip has reached the substrate at 3000 μN.

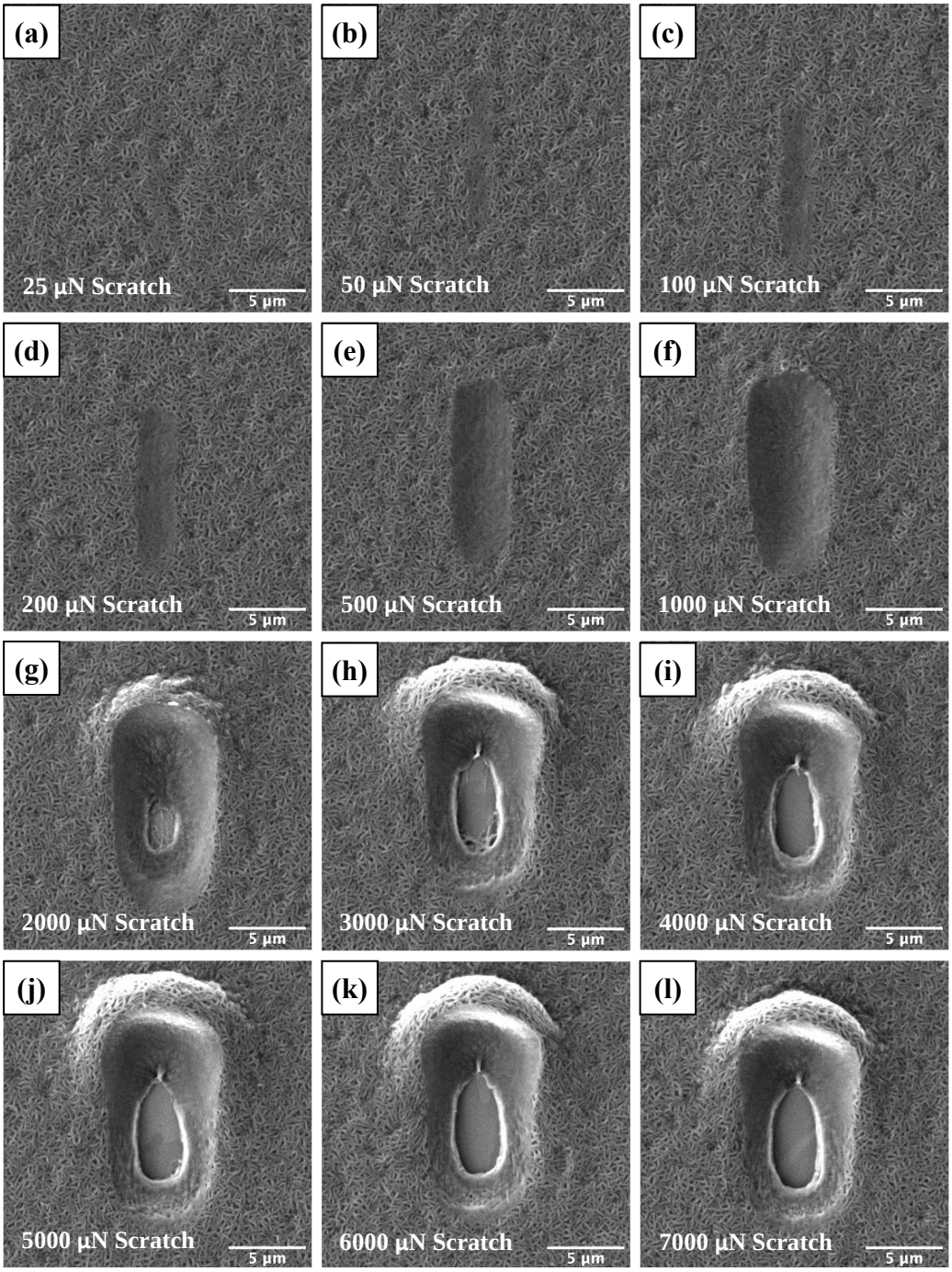

Figure 4.5. Scanning electron microscope image of the scratches performed on 60NiTi/PDA/PTFE using the diamond tip with normal forces of (a) 25, (b) 50, (c) 100, (d) 200, (e) 500, (f) 1000, (g) 2000, (h) 3000, (i) 4000, (j) 5000, (k) 6000, and (l) 7000 μN. The scratch direction was from the bottom to the top of each image.

The time when the tip penetrated the coating and reached the substrate can be identified by closely inspecting the beginning portion of the normal displacement versus time plot in Figure 4.4. A sudden increase in the normal displacement occurred in the plots when the tip starts to penetrate the coating. For the 3000 μN and 4000 μN scratches, this occurred around t = 23 s and 21 s, respectively, both during scratches. However, at loads of 5000 μN and greater, the penetration occurred prior to t = 20 s. This indicates that the coating failed during the loading segment prior to the scratch.

The build-up of coating material at the end of the scratches (top of the images in Figure 4.5) is also informative for the coating failure mechanisms. Little to no build-up occurred during scratches at loads of 1000 μN and less. However, during the 2000 μN scratch a moderate amount of build-up occurred, and at loads of 3000 μN and greater, large and consistent amounts of build-up were observed. Build-up began when the scratch load was large enough to tear the PTFE, but the 2000 μN load was not great enough to fully penetrate the coating, and only a moderate amount of build-up occurred. At loads of 3000 μN and greater, the coating failed completely, the substrate was exposed, and large amounts of build-up occurred due to ploughing of the coating. Ploughing and build-up do not occur at the lower scratch loads because the coating was only being plastically deformed and compressed.

The normal displacement plots and SEM images of Figures 4.4 and 4.5 can be used to interpret how the COF of 60NiTi/PDA/PTFE changed as the scratch load varied in Figure 4.3. The COF increased from loads of 500 to 2000 μN because of increasing amounts of plastic deformation in the coating. However, as the scratch load was increased beyond 2000 μN, the

COF decreased because the tip reached the substrate and the amount of plastic deformation plateaued. Additionally, at loads of 3000 μN and greater, the entire thickness of the coating is removed through ploughing. The lateral forces applied to the tip were predominantly by ploughing through the coating, which were similar at each scratch load above 2000 μN because the same amount of material was being displaced during each scratch. Therefore, the lateral force on the tip due to ploughing remains steady while the normal force increases, and the recorded COF drops.

Since tribological applications involve many loading cycles in the same sliding area, repeating scratch tests were designed to investigate the scratch behavior of the coating after it had been compressed by prior scratches at the same location. The repeating scratches were performed at a 1000 μN load after a uniform and solid morphology is formed from the first scratch. A plot of the normal displacement versus time for the repeating 1000 μN scratches is shown in Figure 4.6. Each scratch began at the same location, and the normal displacement of the second and third scratches grew rapidly as the loading began because the tip moved down into the displaced area caused by the first scratch. Within the first second of the loading segment, the tip touched the compressed coating surface, and the slope of the displacement versus time curve is flatter throughout the remainder of the loading segment for the second and third scratches than it was for the first scratch. During the second scratch, additional displacement and compression of the coating occurred, but the tip only progressed around 100 nm further into the coating than the 700 nm that it did during the first scratch. On the third scratch, the tip furthered the maximum displacement of the coating by less than 50 nm. This trend shows that the compression of the coating into a solid and uniform layer by 1000 μN scratches strengthens the

coating's resistance to deformation. Additionally, the average COF dropped during each subsequent scratch, with the COF being 0.28, 0.22, and 0.20 for the first, second, and third scratch, respectively. Therefore, compression of the coating by previous scratches reduced the COF by changing the morphology of the coating and reducing the amount of plastic deformation that occurred during the scratch.

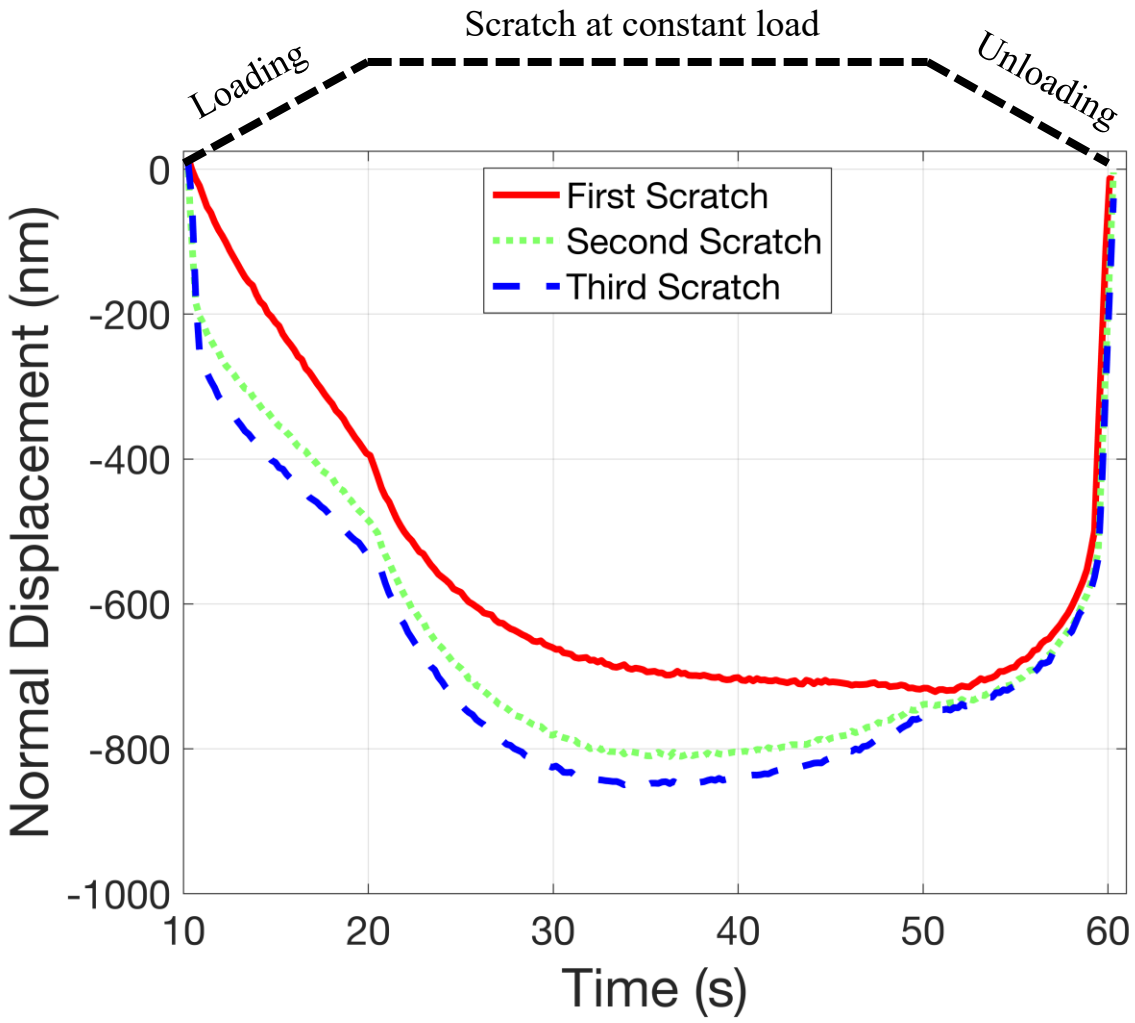

Figure 4.6. Normal displacement vs. time for the repeating 1000 μN scratches on 60NiTi/PDA/PTFE.

Past studies of PDA/PTFE coatings have reported large amounts of coating wear depth change in the early stage of linear reciprocating wear tests followed by extended durability of a

thin and resilient layer at the coating/substrate interface [8,10,17,18]. The results from this scratch study suggest that the large amounts of the wear depth change during the beginning of the tests of PDA/PTFE coatings is primarily due to compression of the porous PTFE layer. The thin and resilient layer at the coating/substrate interface was also shown to consist of compressed PTFE [16], which was more solid and durable than the as-deposited porous coating.

4.3.5 Scratching of 60NiTi/PDA

Previous studies showed that the durability of PDA/PTFE coatings is greatly improved compared to PTFE coatings due to the addition of the PDA adhesive underlayer [8-11,16-18]. Scratch tests were performed on PDA-coated 60NiTi to investigate the COF of 60NiTi/PDA, the resilience of the PDA layer, and the correlation between the scratch behavior of 60NiTi/PDA and 60NiTi/PDA/PTFE. Figure 4.3 shows the COF of 60NiTi/PDA. This sample had the highest COF and greatest resistance to the tip's movement across the surface at low normal loads of 25 and 50 μN among the three types of samples tested. At low normal loads, the adhesive force between the tip and the surface dominates the COF, and the COF is generally higher than that at higher normal loads [24-27]. 60NiTi/PDA had a higher COF than 60NiTi during low load scratches; this suggests that the PDA layer increased the adhesive forces between the tip and the sample, which supports the findings that PDA can be used as an adhesive underlayer [8]. The COF of 60NiTi/PDA at loads of 2000 μN and above approached the same value as the COF of 60NiTi. The reduction in COF at higher loads was caused by the insignificance of the adhesive forces compared to the applied normal loads and the PDA agglomerates being removed from the

60NiTi surface at higher loads as shown in Figure 4.7, which shows the scratches on 60NiTi/PDA imaged using SEM.

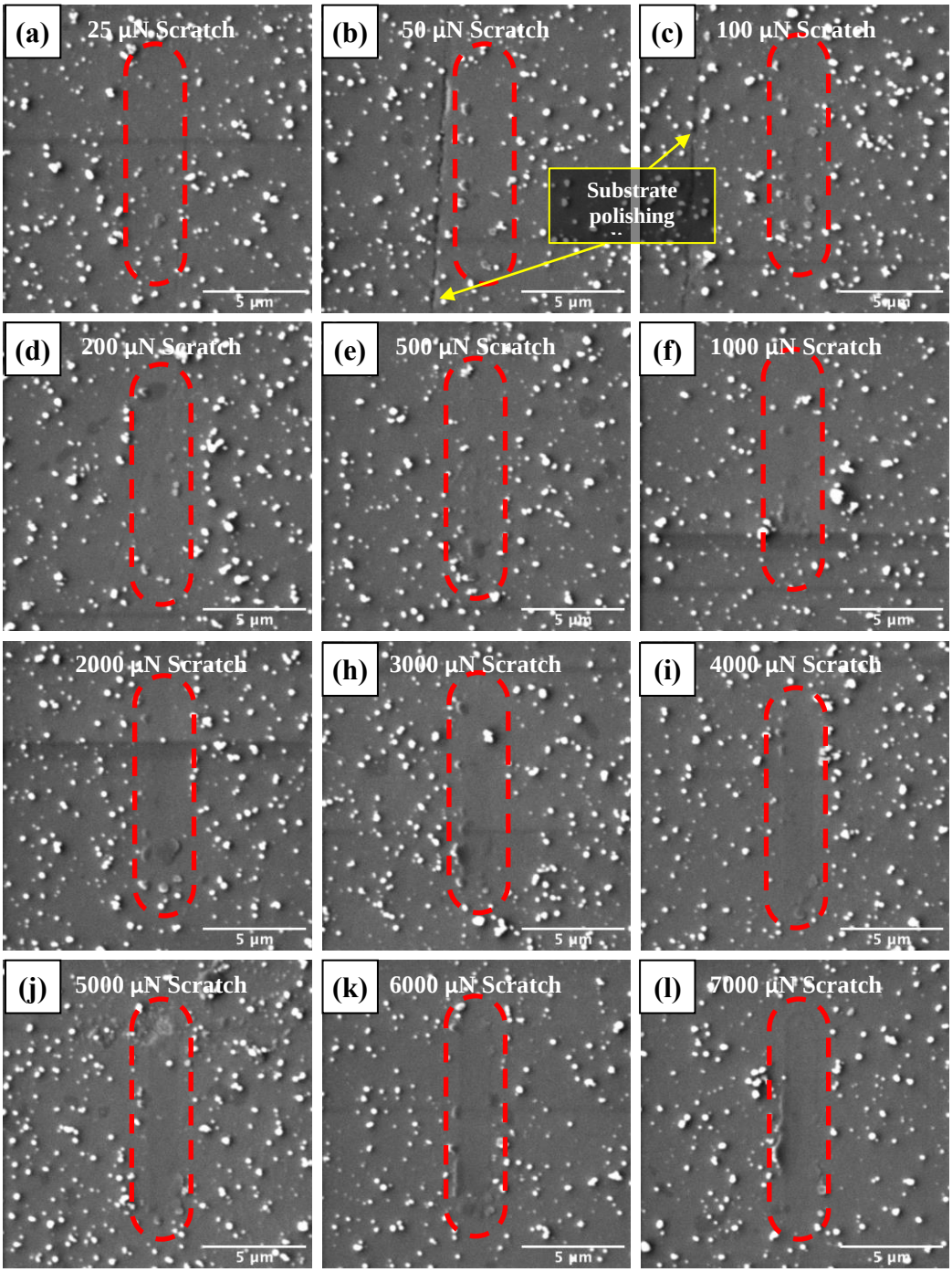

Figure 4.7. Scanning electron microscope images of the scratches performed on 60NiTi/PDA using the diamond tip with normal forces of (a) 25, (b) 50, (c) 100, (d) 200, (e) 500, (f) 1000, (g) 2000, (h) 3000, (i) 4000, (j) 5000, (k) 6000, and (l) 7000 µN. The area containing the scratches is emphasized by the dashed red lines.

The areas containing the scratches are emphasized by the red dashed lines in Figure 4.7. At loads up to 1000 μN, the PDA agglomerates were compressed and appear darker than the surrounding aggregates in the images. At loads of 2000 and 3000 μN, fewer compressed aggregates appear inside the scratch area; at loads greater than 3000 μN, the PDA aggregates are almost completely removed from the center of the scratch area. The removal of the PDA aggregates occurs at loads that coincide with the ploughing of the PDA/PTFE coating and exposure of the 60NiTi substrate. Therefore, the ploughing of PDA/PTFE is likely related to the removal of PDA aggregates from the substrate.

4.4 Conclusions

The nanoindentation behavior of 60NiTi indented by a spheroconical diamond tip with a tip radius of 5 μm showed Hertzian contact behavior at indentation loads up to 1000 μN, which corresponds to a Hertzian contact pressure of 4.07 GPa. Scratch tests under a range of applied normal load using this indenter on 60NiTi, 60NiTi/PDA/PTFE, and 60NiTi/PDA revealed the COF, deformation, and failure mechanisms of the various samples. For all the samples, COF was the highest at the lowest load scratch (25 μN) due to the adhesive forces dominating. At this load, 60NiTi/PDA had the highest COF, which indicated that the PDA layer effectively modified the 60NiTi surface to have greater adhesion. Scratches on 60NiTi/PDA showed that the PDA aggregates are compressed during lower loads and are removed from the substrate surface by scratch loads greater than 3000 μN. The COF of the 60NiTi/PDA/PTFE sample varied with the scratch load due to different deformation mechanisms. The COF increased as the amount of plastic deformation of the coating increased, but it decreased after the coating failed due to

ploughing and tensile failure. The load at which the 60NiTi/PDA/PTFE experienced coating failure corresponds to the load that caused the removal of the PDA aggregates.

This study provided insights to the scratch behavior of 60NiTi/PDA/PTFE coatings. Scratches with lower loads caused the coating to deform plastically to form a more uniform and compressed layer. A threshold load of 2000 μN was identified at which the PDA/PTFE coating began to tear during scratch. At scratch loads greater than 2000 μN, the coating tore, the substrate was exposed, and large amounts of build-up occurred at the end of the scratch. Additionally, repetitive scratches at a 1000 μN load showed that the compression of the coating into a uniform and solid layer reduced subsequent deformation and the COF during scratching. This study revealed that the large initial wear depth in previous macro-tribology studies could be due to the coating compaction rather than being plowed away.

4.5 Acknowledgements

We thank the National Aeronautics and Space Administration (NASA) for the support under NASA Award No: 80NSSC17M0020 and Dr. Adam Howard at the NASA Glenn Research Center (GRC) for serving as our NASA Technical Monitor and Technical Contact. We also thank Dr. Christopher DellaCorte at the NASA GRC for serving as our Technical Contact and providing the 60NiTi samples. Additionally, we thank the Arkansas Biosciences Institute and the University of Arkansas for major equipment funding support.

4.6 References

[1] C. DellaCorte, Novel super-elastic materials for advanced bearing applications, Advances in Science and Technology 89 (2014) 1-9.

[2] C. DellaCorte, W. Wozniak, Design and Manufacturing Considerations for Shockproof and Corrosion-Immune Superelastic Nickel-Titanium Bearings for a Space Station Application, NASA Technical Report, NASA/TM-2012-216015, 2012.

[3] M.K. Stanford, Preliminary investigation of surface treatments to enhance the wear resistance of 60-nitinol, NASA Technical Report, NASA/TM-2016-219121, 2016.

[4] S. Pepper, Nitinol 60 as a Material for Spacecraft Triboelements, 13th European Space Mechanisms and Tribology Symposium - ESMATS 13 Conference, Vienna, Austria, September 25-27, 2009.

[5] C. DellaCorte, F. Thomas, O. Leak, Tribological Evaluation of Candidate Gear Materials Operating under Light Loads in Highly Humid Conditions, NASA Technical Report, NASA/TM-2015-218896, 2015.

[6] C. DellaCorte, M. Jefferson, 60NiTi Intermetallic Material Evaluation for Lightweight and Corrosion Resistant Spherical Sliding Bearings for Aerospace Applications (Report on NASA-Kamatics SAA3–1288), NASA Technical Report, NASA/TM-2015-218723, 2015.

[7] C. DellaCorte, R. Noebe, M. Stanford, S. Padula, Resilient and Corrosion-Proof Rolling Element Bearings Made From Superelastic Ni-Ti Alloys for Aerospace Mechanism Applications, NASA Technical Report, NASA/TM-2011-217105, 2011.

[8] S. Beckford, M. Zou, Wear Resistant PTFE Thin Film Enabled by a Polydopamine Adhesive Layer, Applied Surface Science 292 (2014) 350-356.

[9] C. Miller, D. Choudhury, M. Zou, The Effects of Surface Roughness on the Durability of Polydopamine/PTFE Solid Lubricant Coatings on NiTiNOL 60, Tribology Transactions 62 (5) (2019) 919-929.

[10] D. Choudhury, C. Miller, M. Zou, Tribological performance of PDA/PTFE+ Graphite particle coatings on 60NiTi, Applied Surface Science 527 (2020) 146731.

[11] D. Choudhury, C. Miller, N. Harris, M. Zou, The Effect of Coating Thickness on the Tribological Properties of Polydopamine/PTFE + Graphite Particle Coatings on 60NiTi, Surface Coatings and Technology 420 (2021) 127320.

[12] S. Beckford, M. Zou, The Effects of Graphite Filler on the Tribological Properties of Polydopamine/PTFE Coatings, Tribology Letters 64 (3) (2016) 42-53.

[13] S. Beckford, Y. Wang, M. Zou, Wear-Resistant PTFE/SiO_2 Nanoparticle Composite Films, Tribology Transactions 54 (6) (2011) 849-858.

[14] S. Beckford, J. Cai, J. Chen, M. Zou, Use of Au Nanoparticle-Filled PTFE Films to Produce Low-Friction and Low-Wear Surface Coatings, Tribology Letters 56 (2) (2014) 223-230.

[15] S. Beckford, L. Mathurin, J. Chen, M. Zou, The Influence of Cu Nanoparticles on the Tribological Properties of Polydopamine/PTFE + Cu Films, Tribology Letters 59 (1) (2015) 1-9.

[16] Z. Yang, M. Zou, Experimental investigation of the wear mechanisms of thin PDA/PTFE coatings, Progress in Organic Coatings 137 (2019) 105341.

[17] S. Ghosh, C. Miller, D. Choudhury, J. Goss, M. Zou, The Effects of PTFE Thickness on the Tribological Behavior of Thick PDA/PTFE Coatings, Tribology Transactions 63 (3) (2020) 575-584.

[18] F. Soltani-Kordshuli, D. Okyere, J. Chen, C. Miller, N. Harris, M. Afshar-Mohajer, S. Ghosh, M. Zou, Tribological Behavior of the PDA/PTFE+ Cu-SiO_2 Nanoparticle Thin Coatings, Surface and Coatings Technology 409 (2021) 126852.

[19] B. Hornbuckle, R. Noebe, G. Thompson, Influence of Hf solute additions on the precipitation and hardenability in Ni-rich NiTi alloys, J. Alloys Compd. 640 (2015) 449-454.

[20] SPECIFICATIONS FOR 60Ni-40Ti BILLETS, NASA Technical Standard, MSFC-SPEC-3706, 2016.

[21] Bhushan, B., Introduction to Tribology, second ed., John Wiley & Sons, Hoboken, New Jersey, 2013.

[22] C. Miller, C. DellaCorte, M. Zou, Nanomechanical properties of hardened 60NiTi, Materials Science and Engineering: A 800 (2021) 140284.

[23] C. DellaCorte, L. Moore, J. Clifton, Static Indentation Load Capacity of the Superelastic 60NiTi for Rolling Element Bearings, NASA Technical Report, NASA/TM-2012-216016, 2012.

[24] M. Zou, L. Cai, H. Wang, D. Yang, T. Wyrobek, Adhesion and Friction Studies of a Selectively Micro/nano-textured Surface Produced by UV Assisted Crystallization of Amorphous Silicon, Tribology Letters 20 (1) (2005) 43-52.

[25] M. Zou, L. Cai, H. Wang, Adhesion and Friction Studies of a Nano-textured Surface Produced by Spin Coating of Colloidal Silica Nanoparticle Solution, Tribology Letters 21 (1) (2006) 25-30.

[26] M. Zou H. Wang, P. Larson, K. Hobbs, M. Johnson, O. Awitor, Ni Nanodot-patterned Surfaces for Adhesion and Friction Reduction, Tribology Letters 24 (2) (2006) 137-142.

[27] M. Zou, W. Seale, H. Wang, Comparison of Tribological Performances of Nano- and Micro-textured Surfaces, Proceedings of the Institution of Mechanical Engineers, Part N, Journal of Nanoengineering and Nanosystems 219 (3) (2006) 103-110.

CHAPTER 5

REPETITIVE NANOINDENTER SCRATCH TESTING OF POLYDOPAMINE/POLYTETRAFLUOROETHYLENE-BASED THIN COATINGS

Abstract

Repetitive nanoindenter scratch testing and scanning electron microscopy were used to evaluate the scratch resistance, deformation, and mechanisms of failure of polydopamine (PDA)/polytetrafluoroethylene (PTFE)-based coatings deposited on both polished and roughened 60NiTi substrates. PDA was used as an adhesive layer between the substrate and the PTFE top layer with and without 0.25 wt% graphite particles (GPs). The roughened substrate enabled mechanical interlocking with the coatings that prevented global delamination which occurred with the coatings on the polished substrate due to weak adhesion. The inclusion of GPs improved the coating cohesion and enabled the PDA/PTFE coating with GPs on the roughened substrate to compact into a more plowing-resistant layer with stronger interlocking with the substrate roughness. Therefore, the GP-containing coating deposited on a roughened substrate showed far superior performance, and it is a promising solid lubricant for tribological applications that involve repetitious sliding at high contact pressures, such as bearings and gears.

5.1 Introduction

60NiTi has many properties that are desirable for bearing and gear applications [1-4]. However, it has poor tribological performance when it is not properly lubricated [5-6]. Polytetrafluoroethylene (PTFE) has shown promise as a solid lubricant for 60NiTi to improve its tribological performance for bearing and gear applications [7]. However, PTFE, when applied as a coating, has a high wear rate and poor adhesion to the substrate, which causes PTFE coating to

be prone to delamination when subjected to tribological testing at high contact pressures that are often encountered in bearing and gear applications. Various techniques have been used to mitigate PTFE coating delamination such as adding a polydopamine (PDA) adhesive layer [8-19], roughening the substrate [16], and adding micro/nanoparticles to PTFE [10-12,14-15,17].

PDA is a biomimetic polymer that has been found to stick to many different types of materials, including non-stick PTFE [8]. Therefore, PDA has been used as an adhesive underlayer to increase the adhesion of PTFE coatings to substrates such as stainless steel [9-15] and 60NiTi [16-19]. During progressive wear tests on stainless steel substrate coated with PTFE only or coated with a PDA underlayer and then PTFE (PDA/PTFE), most of the coating thickness was shown to be removed during the first cycle [9]. After that, the PTFE only coating failed within 10 cycles. In contrast, the PDA/PTFE coating lasted over 5000 cycles due to the increased adhesion between the PTFE coating and the substrate provided by PDA, which corresponded to over 500 times the durability of PTFE alone [9]. However, the drastic coating thickness decrease during the first cycle was measured using a contact profiler with a large stylus tip, which could not provide details of the coating morphology and thus could not reveal whether the coating thickness decrease was due to coating compaction or wear.

Another approach for improving the adhesion and durability of PTFE thin films is roughening the substrate surface. A roughened substrate surface increases the interface area between the coating and substrate and thus promotes mechanical interlocking that hinders global delamination. For example, PDA/PTFE coating on a 60NiTi substrate with a valley-dominant

roughness was shown to improve coating durability 38 times compared to PDA/PTFE coating on a polished smooth 60NiTi substrate [16].

The additions of various nanoparticles and graphite particles (GPs) to the PTFE layer of PDA/PTFE coatings have also been shown to further improve tribological performance [10-12,14-15,17]. Adding micro/nanoparticles was found to generate a smoother coating with a less porous fibrillary network and thus enhance coating cohesion [10,14]. The micro/nanoparticles were believed to serve as anchoring points on the substrate to prevent coating global delamination [15]. They also served as anchoring points on the counterface to enhance transfer film formation [14]. Although these macro-scale tribometer tests provided insights into the PTFE coating tribological behavior, they cannot elucidate the micro-scale deformation and failure mechanisms since coating thickness and morphology cannot be imaged at a required fine resolution to observe individual PTFE particles.

Nanoindenter scratch tests enable the load and displacement to be controlled and/or measured with very fine resolution, and scanning electron microscopy (SEM) imaging of nanoindenter scratches can elucidate the micro-scale behavior of PTFE coatings. The combination of nanoindenter scratch testing and SEM imaging of scratches was able to reveal that the drastic reduction in the PDA/PTFE coating thickness on a polished 60NiTi substrate during a single scratch was mainly due to coating compaction, rather than the plowing observed in macroscale tribological testing [19]. Repetitive nanoindenter scratches also showed the coating was compacted to a more deformation-resistant layer during subsequent scratches, which explained the improved wear resistance at the coating-substrate interface. Overall, the study

provided a deeper understanding of the thin PDA/PTFE coating deformation and wear mechanisms. However, only pure PDA/PTFE coatings deposited on polished smooth substrates were studied.

Since adding GPs to the PTFE layer and roughening the substrate significantly improved the tribological performance of the PDA/PTFE coating, the objective of this study is to understand the mechanisms of the improvement. To do that, repetitive nanoindenter scratch tests were conducted to compare the deformation and failure mechanisms of PDA/PTFE with and without 0.25 wt% GPs incorporated in the PTFE layer (PDA/PTFE + 0.25 wt% GPs) deposited on both polished and roughened 60NiTi substrates. Understanding the deformation behavior and failure mechanisms of these coatings on 60NiTi when subjected to repetitive sliding loads is critical for applying them to applications using 60NiTi bearings and gears [2-5,7].

5.2 Experimental Methods

5.2.1 Sample Preparation

Hardened plates of 60NiTi were supplied by the National Aeronautics and Space Administration Glenn Research Center. The plates originated from billets that were formed using a hot isostatic press, cut to shape by wire electrical discharge machining, and heat-treated to a hardened state [20]. The 60NiTi surfaces were prepared with a grinder-polisher machine (Buehler EcoMet 300 Polisher, Buehler, Lake Bluff, IL, USA). The two surface finishes used in these experiments are denoted as “polished” and “roughened.” The polished surface is a mirror finish with sub-10 nm of arithmetic mean roughness (R_a), and it was produced using a three-step process. Briefly, the sample was first sanded to flatten the surface. Then, it was polished using

diamond and colloidal silica suspensions. The roughened surface is a unidirectional valley-dominated topography that was produced by taking a flat and polished sample and lightly sanding it and then blunting the surface peaks by light lapping with diamond polishing suspension for a short period. The processes used to produce the polished and roughened 60NiTi surface finishes are described in detail before [16]. The sanding was performed unidirectionally to produce parallel grooves so that the scratch test direction could be made consistently perpendicular to the groove direction.

PDA was deposited on 60NiTi surfaces through submersion in a bath of deionized water. The PDA deposition process is described in greater detail in a previous study [19]. Briefly, the bath was heated to 60 °C and buffered to a pH of 8.5. Dopamine hydrochloride (H8502, Sigma Aldrich, St. Louis, MO, USA) was added, and a rocking shaker was used to rock the bath so that the rate of PDA polymerization increased. The deposition was allowed to take place for 1 h, and then the PDA-coated samples were taken out of the bath, rinsed with water, and blown dry.

PTFE and PTFE + 0.25 wt% GPs were deposited on the PDA-coated 60NiTi surfaces using a dip-coater (KSV DC, KSV NIMA, USA) to insert and remove the samples from aqueous suspensions. The processes used to prepare the PTFE and PTFE + 0.25 wt% GPs suspensions were detailed in a past study [17]. The PTFE coating was deposited on PDA-coated substrates using a dipping speed of 10 mm/min. The dip-coating rate was increased to 20 mm/min for the PTFE + GPs coating because the coating was too thin when a dipping rate of 10 mm/min was used. After dip-coating, all samples were heat-treated using a three-step process to remove water and surfactants from the coating and sinter the PTFE particles [17].

These methods were used to prepare four different sample types, all with a PDA underlayer between the top coating and the 60NiTi substrate: 1) polished substrate with PTFE (polished 60NiTi/PDA/PTFE), 2) polished substrate with PTFE + 0.25 wt% GPs (polished 60NiTi/PDA/PTFE + 0.25 wt% GPs), 3) roughened substrate with PTFE (roughened 60NiTi/PDA/PTFE), and 4) roughened substrate with PTFE + 0.25 wt% GPs (roughened 60NiTi/PDA/PTFE + 0.25wt% GPs).

5.2.2 Sample Characterization

The surfaces of the polished and roughened 60NiTi substrates were imaged using 3D laser-scanning confocal microscopy (VK-X260K, Keyence Corporation of America, USA). The roughness of the substrates and coated surfaces was measured through a contact profilometer (Dektak 150, Veeco, Plainview, NY, USA). The surfaces of the coatings and the nanoindenter scratches were imaged using SEM (VEGA3, Tescan, Brno, Czech Republic). The elastic modulus (E) and hardness (H) of the coatings were measured using a nanoindenter (TriboIndenter, Hysitron, Minneapolis, MN, USA) and a spheroconical diamond-tipped probe with a tip radius of 1μm tip.

5.2.3 Nanoindenter Scratch Testing

Constant load scratches were made on each of the four sample types using a nanoindenter (TriboIndenter, Hysitron, Minneapolis, MN, USA), and all scratches were performed using a diamond-tipped probe with a 5 μm tip radius. Constant normal loads of 1500, 1750, 2000, 2250, 2500, and 2750 μN were applied during scratching, which are equivalent to Hertzian contact pressures of 4.66, 4.90, 5.13, 5.33, 5.52, and 5.70 GPa, respectively, when neglecting the coating

effect. The high contact pressures were selected to understand the coating failure mechanisms for potential ball bearing and gear applications. A schematic for the scratch test is shown in Figure 5.1. To perform a scratch, the tip makes initial contact with the surface (Figure 5.1, location 1). Then, the tip moves laterally (*x*-direction) -4 μm at 1 μN load (location 2). Next, the intended scratch load is applied at a constant loading rate over a 10-second interval (location 3). After the loading period, the tip moves +8 μm laterally at a constant speed over a 30-second interval to perform the constant load scratch (location 4). Then, complete unloading occurs at a constant unloading rate over a 10-second interval (location 5). During unloading, the tip disengages from the surface as it moves to the z-height of initial contact. Lastly, the tip moves -4 μm laterally to the location of initial contact under zero normal load (location 1). At this point, the first scratch has been completed. To perform subsequent scratches, the tip moves laterally -4 μm at zero

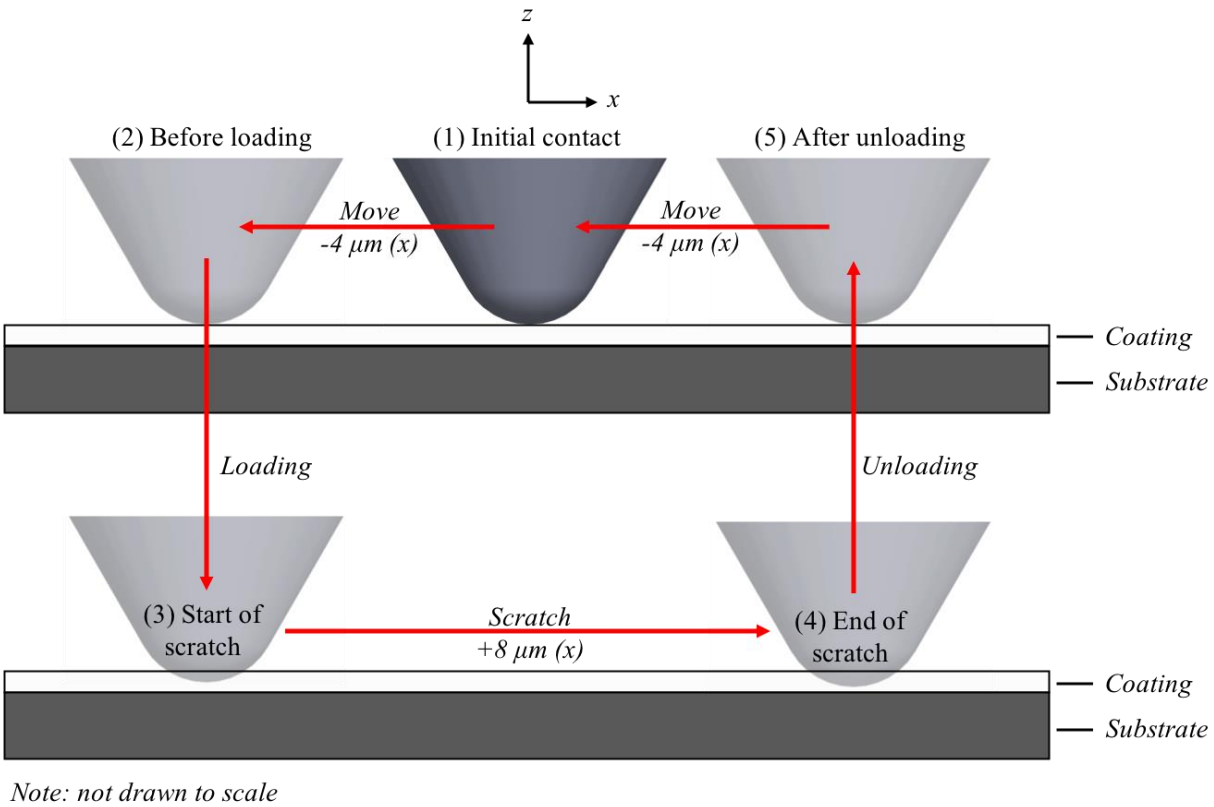

Figure 5.1. Schematic of the scratch method.

normal load to return to location 2. Then, the loading, scratch, unloading, and lateral movement to location 2 are repeated until 10 scratches have been completed. Therefore, the scratches are unidirectional.

5.3 Results

5.3.1 Sample Characterization

3-D maps of the surfaces of the polished and roughened 60NiTi substrates are shown in Figure 5.2. The roughened surface has a valley-dominated topography that has been shown to provide mechanical interlocking between PDA/PTFE coating and 60NiTi substrate during macro-scale tribological testing [16].

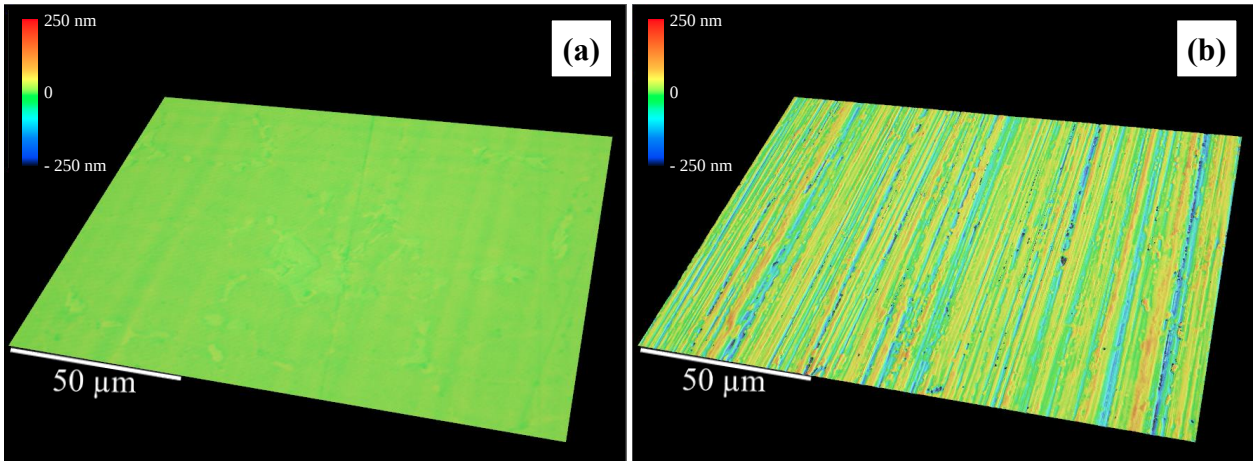

Figure 5.2. 3D images of (a) polished and (b) roughened 60NiTi.

Figure 5.3 shows the line profiles from stylus profilometry scans on polished 60NiTi and roughened 60NiTi along with PDA/PTFE and PDA/PTFE + 0.25 wt% GPs on both polished and roughened 60NiTi, respectively. The scans on samples with roughened substrate were made perpendicular to the groove direction, which is the same orientation used for scratch testing since

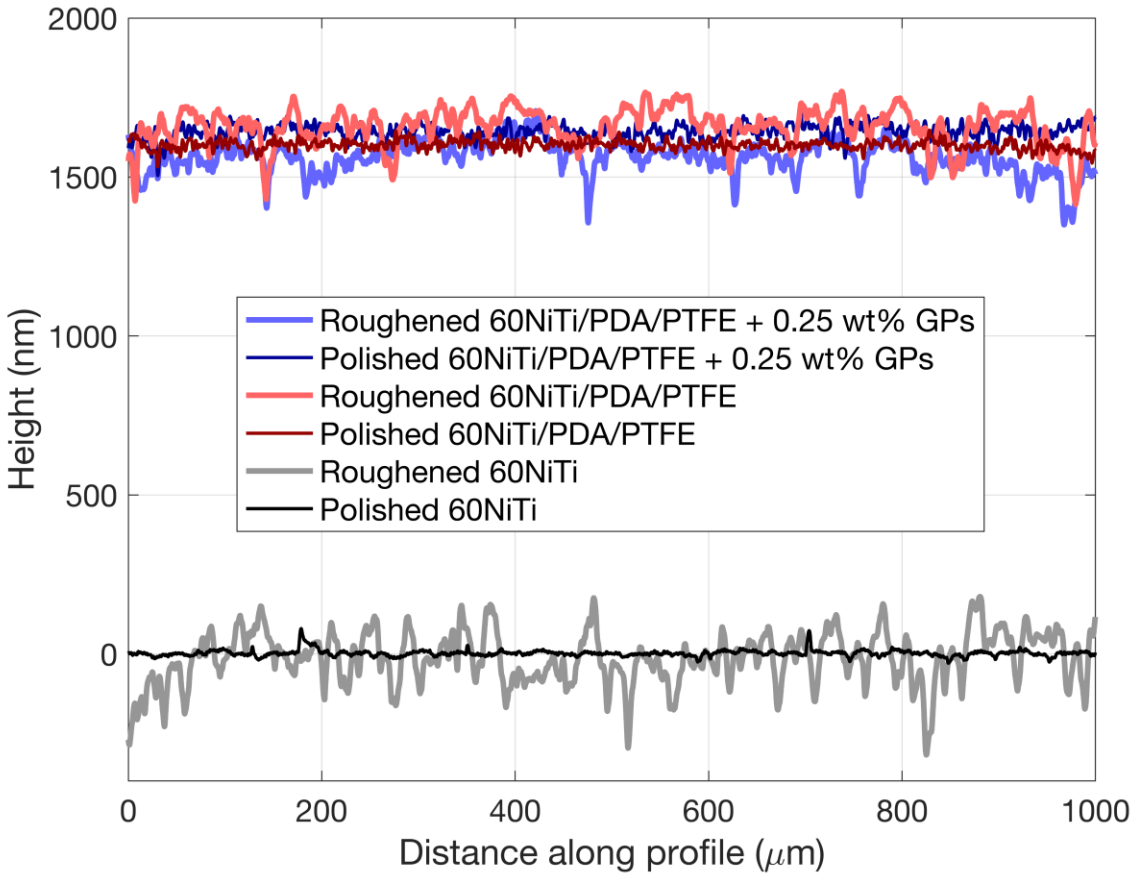

Figure 5.3. Line profiles of polished 60NiTi, roughened 60NiTi, polished 60NiTi/PDA/PTFE, roughened 60NiTi/PDA/PTFE, polished 60NiTi/PDA/PTFE + 0.25 wt% GPs, and roughened 60NiTi/PDA/PTFE + 0.25 wt% GPs.

it will result in the largest roughness effect. The profiles of the coated surfaces are offset by the approximate coating thickness of each sample. The approximate coating thicknesses are shown in Table 5.1 and are derived from the normal displacement of scratches that make contact with the substrate. The arithmetic mean roughness, R_a, root-mean-square roughness, R_q, and skewness, R_{sk}, were measured from the profilometer scans and are also shown in Table 5.1. The polished substrate had a very low average R_a of 5.0 nm, and the roughened substrate had an average R_a of 58.3 nm. Coating PDA/PTFE on polished 60NiTi slightly increased the average R_a (12.9 nm), and coating PDA/PTFE on roughened 60NiTi slightly decreased the average R_a (42.0

nm). Adding GPs to PTFE resulted in a slight increase in roughness in the case of polished substrates and a slight decrease in roughness in the case of roughened substrates. The valley-dominant topography of the roughened substrate is indicated by its negative skewness (-0.2).

Table 5.1. Coating thicknesses and roughness.

	Polished 60NiTi	**Roughened 60NiTi**	**Polished 60NiTi/PDA/ PTFE**	**Polished 60NiTi/ PDA/PTFE + 0.25 wt% GPs**	**Roughened 60NiTi/PDA/ PTFE**	**Roughened 60NiTi/ PDA/PTFE + 0.25 wt% GPs**
Approx. coating thickness (nm)	N/A	N/A	1600	1650	1650	1550
Mean ± SD						
R_a (nm)	5.0 ± 1.3	58.3 ± 5.7	12.9 ± 3.1	17.9 ± 3.4	42.0 ± 2.2	35.1 ± 3.8
R_q (nm)	6.7 ± 1.2	74.9 ± 8.4	15.9 ± 3.5	23.2 ± 3.9	56.4 ± 4.7	45.4 ± 5.0
R_{sk}	0.16 ± 0.33	-0.20 ± 0.12	-0.03 ± 0.19	-0.28 ± 0.34	-0.93 ± 0.37	-0.51 ± 0.30

SEM images of coatings with and without GPs on polished substrates are shown in Figure 5.4. The addition of GPs to the PTFE layer leads to a more even coating with reduced undulations and void sizes. The area percentage of porosity of PDA/PTFE + 0.25 wt% GPs has previously been measured to be 24% less than that of PDA/PTFE [17].

The E and H of polished 60NiTi/PDA/PTFE were measured to be 1.36 ± 0.11 GPa and 49.4 ± 4.9 MPa, respectively. For polished 60NiTi/PDA/PTFE + 0.25 wt% GPs, E and H were 0.97 ± 0.11 GPa and 47.5 ± 5.6 MPa, respectively. The addition of GPs to the PTFE layer reduced the elastic modulus of the coating, but it did not have a significant effect on the hardness. The higher H/E ratio for the coating with GPs is an indicator that it should have improved wear performance [21].

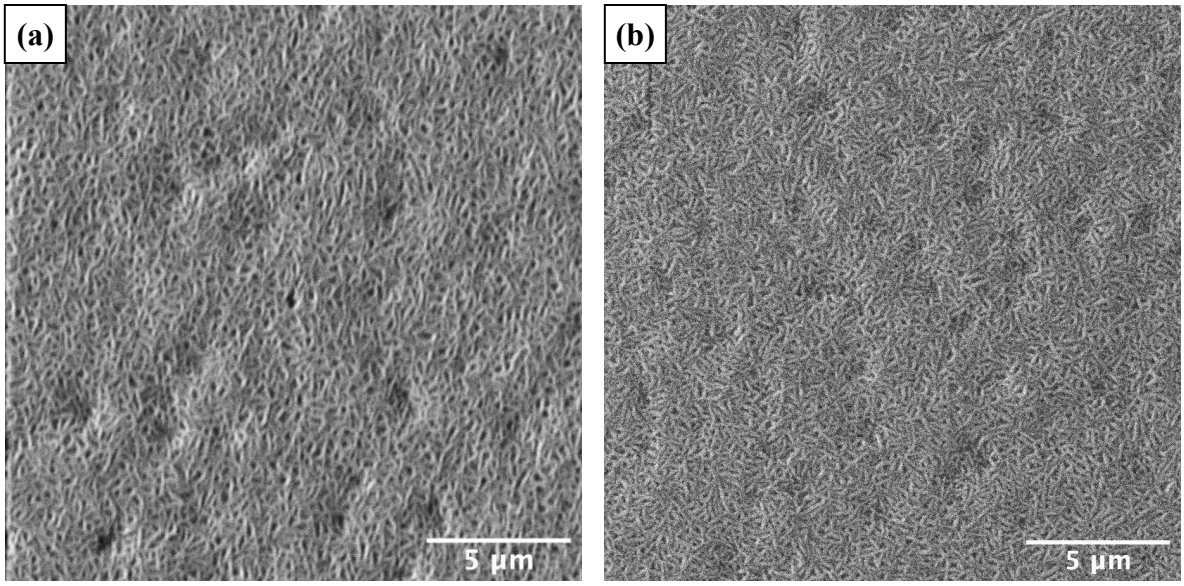

Figure 5.4. SEM images of (a) polished 60NiTi/PDA/PTFE, (b) polished 60NiTi/PDA/PTFE + 0.25 wt% GPs.

5.3.2 Nanoindenter Repetitive Scratch Testing

Figure 5.5 and Figures 5.8-11 show displacement versus time plots and SEM images from ten repetitive scratches on the coatings at various constant normal loads. Figure 5.5 (a) and (c) have additional labels to aid the interpretation of the displacement vs. time plots and their correlation to the SEM images, as well as the scratch direction. In the displacement versus time plots, loading takes place from t = 0 s to t = 10 s. From t = 10 s to t = 40 s, the 8 µm scratch takes place, and from t = 40 s to t = 50 s, unloading occurs. The SEM images below the displacement plots are scaled and oriented so that the length and direction of the scratch align with the plotted scratch (from t = 10 s to t = 40 s). Therefore, all SEM images of scratches are oriented so that the scratches took place from left to right. The plots in Figure 5.5 and Figures 5.8-11 include dashed lines of constant displacement that correspond to the approximate coating thicknesses of the samples. These dashed lines are helpful for visualization, but displacement reaching the approximate coating thickness does not directly correspond to contact between the tip and the

substrate. Instead, a combined analysis of the SEM images and displacement versus time plots was used to determine when the tip makes contact with the substrate.

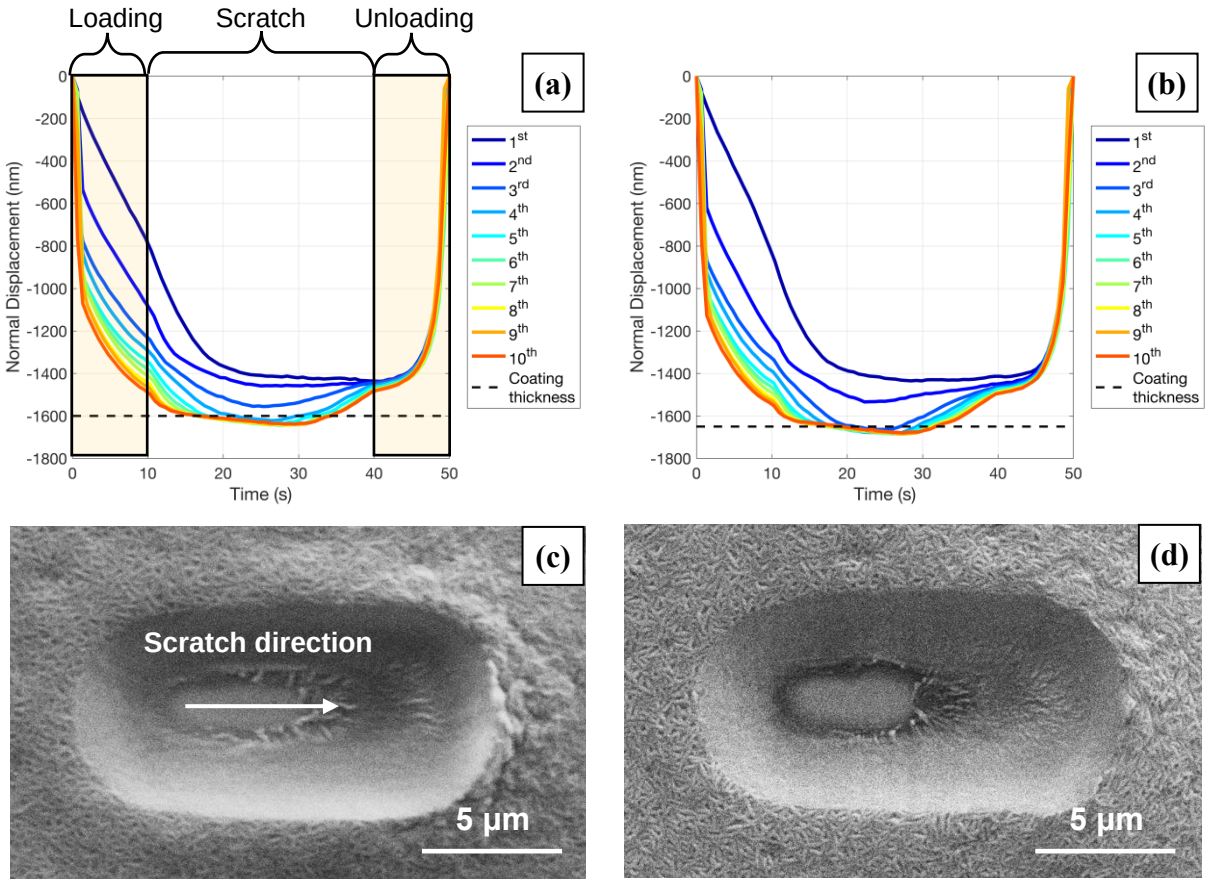

Figure 5.5. Normal displacement vs. time plots for 10 repetitive scratches at 2000 uN load on (a) polished 60NiTi/PDA/PTFE and (b) polished 60NiTi/PDA/PTFE + 0.25 wt% GPs and (c),(d) the corresponding SEM images after 10 scratches, respectively.

Figure 5.5 shows the normal displacement versus time plots and SEM images for the 10 repetitive scratches at 2000 µN load on the PDA/PTFE coatings with and without GPs on the polished substrate. The tip reached the substrate during the 4th scratch on polished 60NiTi/PDA/PTFE (Figure 5.5a) and the 3rd scratch on polished 60NiTi/PDA/PTFE + 0.25 wt% GPs (Figure 5.5b). Upon further scratches, and for both samples, the size of the exposed substrate area grew as can be seen from the widening flat area between t =10 s and t = 30 s in Figures 5.5a and b. However, after ten scratches, the substrate was not exposed for the entire

length of the scratch on either sample. Compacted sections of coating remained towards the end of the scratches (Figures 5.5c and d). Figure 5.6 shows SEM images after ten scratches at 2000, 2250, 2500, and 2750 µN on the coatings with and without GPs on the polished substrate. As the load was increased, the area of substrate exposure grew. At 2750 µN, the substrate was exposed

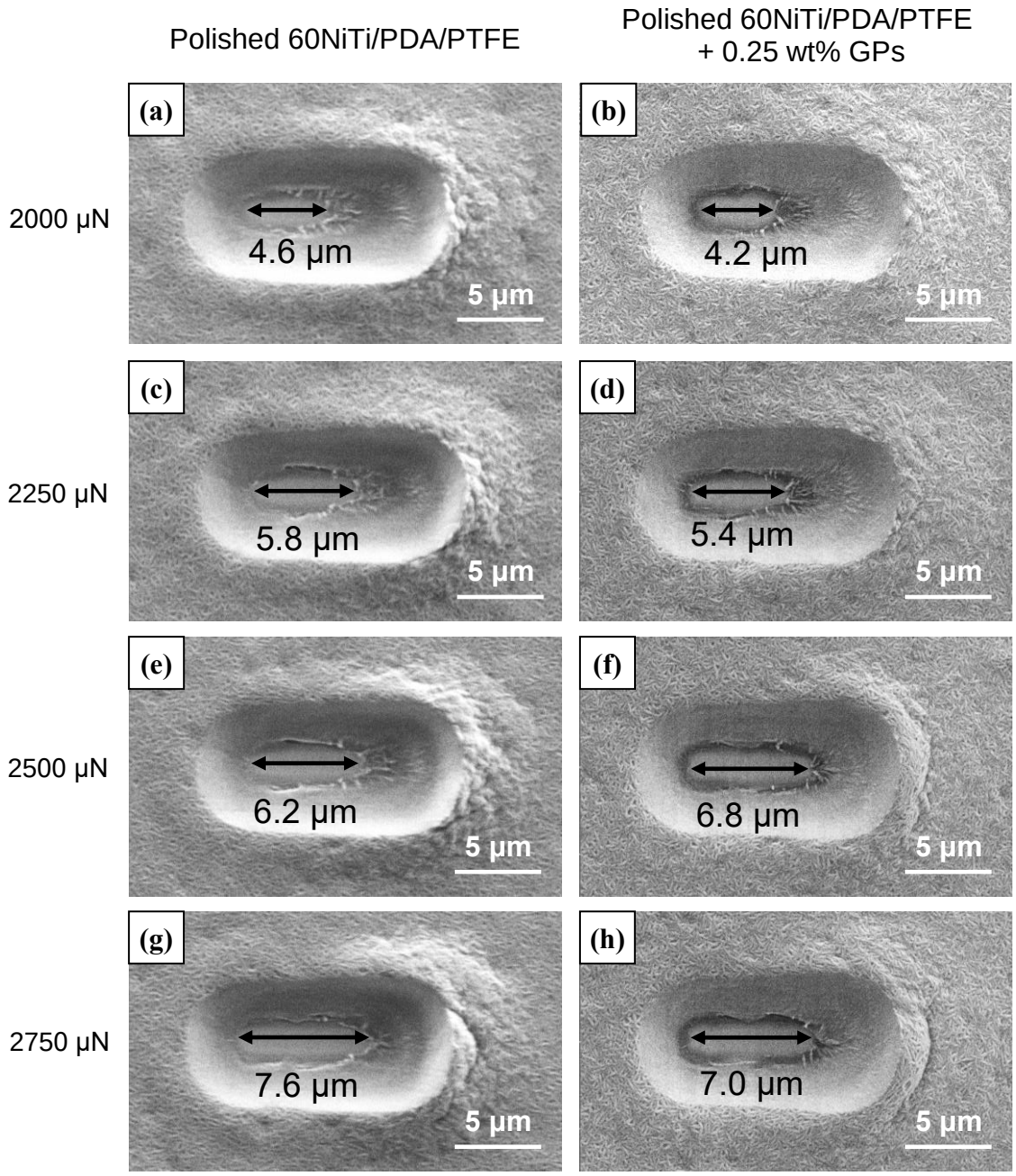

Figure 5.6. SEM images of ten scratches at 2000, 2250, 2500, and 2750 µN load on (a),(c),(e),(g) polished 60NiTi/PDA/PTFE and (b),(d),(f),(h) polished 60NiTi/PDA/PTFE + 0.25 wt% GPs, respectively.

for over 85% of the entire scratch length for both coatings on the polished substrate. From Figure 5.5 and Figure 5.6, it can be seen that the addition of GPs to the PTFE layer did not result in a significant change in scratch behavior when the coatings were applied to the polished 60NiTi substrate.

The failure process for coatings on the polished substrate can be observed from SEM images of 1-4 scratches performed on polished 60NiTi/PDA/PTFE at 2250 μN load in Figure 5.7. When one scratch was made (Figure 5.7a), the coating was compacted, but plowing caused a significant amount of coating to accumulate at the end of the scratch (right side). Small tears in the compacted coating formed around a third of the way into the scratch and are circled in Figure 5.7a. These tears are caused by large tensile stresses that develop behind the tip. After two scratches (Figure 5.7b), two significant tears were formed. In the center of the scratched area, the initial small tears that formed during the first scratch were split and the substrate was exposed. A new and wider tear also formed above and below the path line of the scratch (Figure 5.7b). After three scratches (Figure 5.7c), the tip reached the substrate as it penetrated through the coating in the area of the exposed substrate that formed after the initial tears split. Then, the lateral movement of the tip on the exposed substrate pushed the coating to the right and delaminated the compacted coating that remained inside of the wider tear, causing more of the substrate to be exposed. Upon subsequent scratches, the wide tear gradually lengthens, and the area of the exposed substrate slowly grows as shown in Figure 5.7d. At all loads, for the coatings with and without GPs on the polished substrate, failure occurred through similar mechanisms: large tensile stresses led to tears in the coating that ruptured, widened, and caused delamination of the coating from the substrate upon scratching.

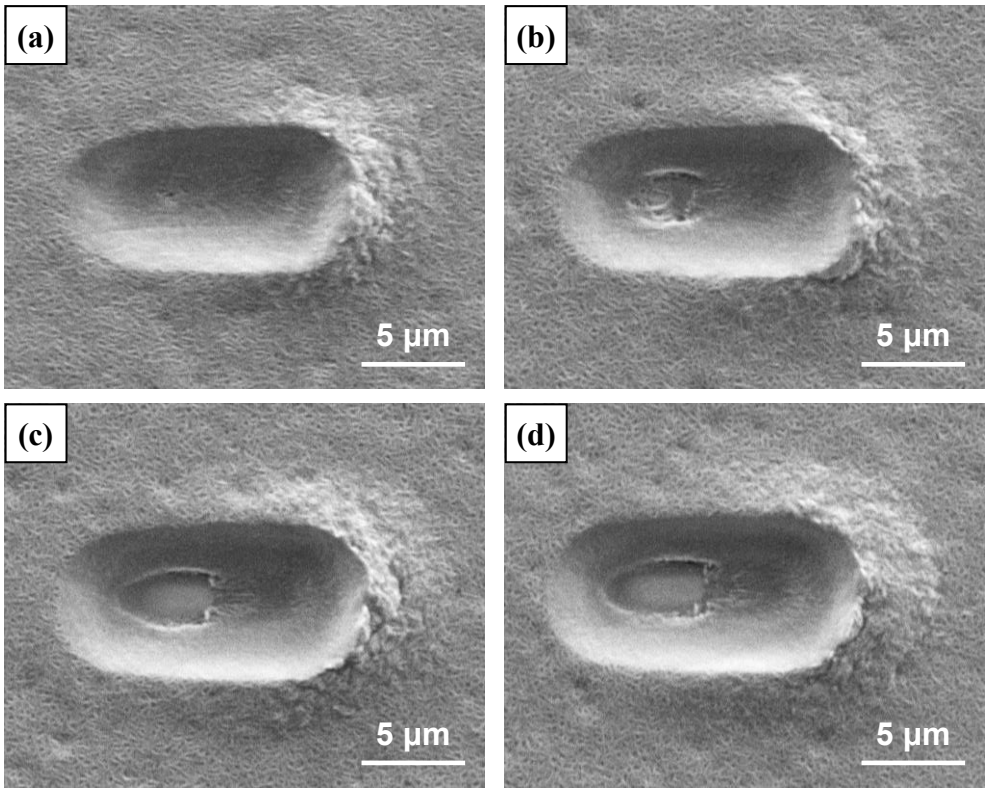

Figure 5.7. SEM images of (a) 1, (b) 2, (c) 3, and (d) 4 scratches at 2250 µN load on 60NiTi/PDA/PTFE.

The coatings on roughened substrates have different behavior than those on polished substrates. Figure 5.8 shows the scratch displacement and SEM images from 10 repetitive scratches at 2000 µN load on PDA/PTFE with and without GPs and on the roughened substrates. For roughened 60NiTi/PDA/PTFE, the displacement plot (Figure 5.8a) shows a gradual increase in displacement from the 2nd to the 7th scratch, and the 8th, 9th, and 10th scratches have displacement near the coating thickness. The gradual increase in displacement from the 2nd to the 7th scratch indicates that tears formed in the coating and led to the slow removal of the compacted coating. However, the gradual nature of the removal indicates that the roughened substrate prevented the coating from tearing, splitting, and delaminating. The mechanical interlocking between the coating and the roughened substrate reduced the tensile stresses in the

coating near the coating/substrate interface and prevented coating delamination. In Figure 5.8c, the SEM image of the scratched area after 10 scratches shows that the coating tore, and a few taller plateaued regions of the 60NiTi surface are exposed in the first half of the scratch. However, there was PDA/PTFE coating in the valleys surrounding these plateaued regions, and a compacted and uniform layer of the coating protected the substrate throughout the second half of the scratches. PDA/PTFE retained inside of the valleys of the 60NiTi surface has been shown to continue to provide sufficient lubrication after the plateaued regions of the substrate surface area are exposed [16].

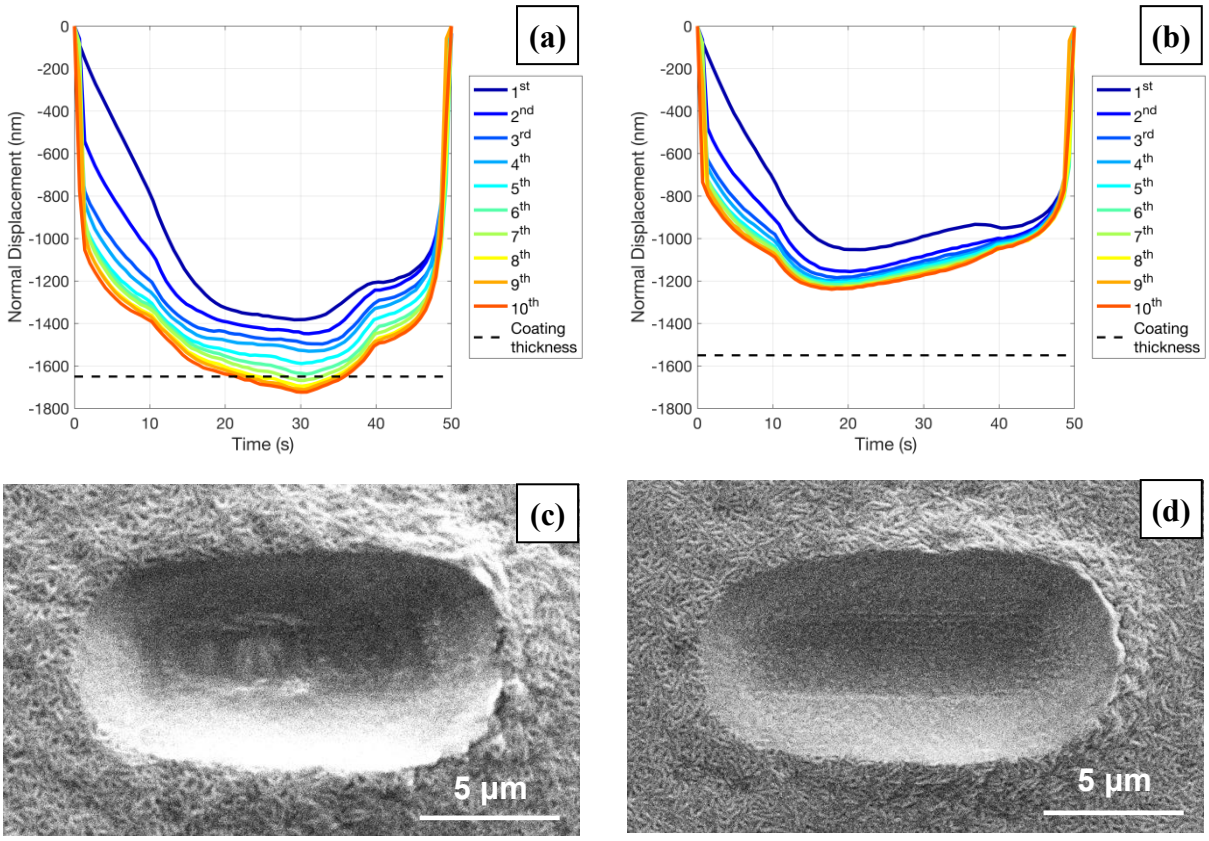

Figure 5.8. Normal displacement vs. time plots for 10 repetitive scratches at 2000 uN load on (a) roughened 60NiTi/PDA/PTFE and (b) roughened 60NiTi/PDA/PTFE + 0.25 wt% GPs and (c),(d) the corresponding SEM images after 10 scratches, respectively.

Different from the results on the polished substrate, the incorporation of GPs in the PTFE coating improved the scratch behavior when these coatings were deposited on a roughened substrate. At 2000 μN load, roughened 60NiTi/PDA/PTFE + 0.25 wt% GPs compacted into a solid and uniform layer of coating with approximately 300 nm of thickness after 10 repetitive scratches (Figures 5.8b and d). Contrary to roughened 60NiTi/PDA/PTFE, roughened 60NiTi/PDA/PTFE + 0.25 wt% GPs did not have a significant tear in the coating, and the 60NiTi substrate was never exposed. The slight increases in displacement from the 2nd to the 7th scratch correspond to further compaction of the coating before the displacement stabilized for the 8th through 10th scratch. This suggests that adding GPs improved the cohesion of the PTFE particles, which leads to better compaction, less tearing of the coating, and improved mechanical interlocking of the coating and the roughened substrate. This improved coating cohesion has also been observed when adding various nanoparticles to the PTFE coating [10,14].

Increasing the scratch load to 2250 μN further differentiated the behavior of the coatings with and without GPs on the roughened substrate. Displacement plots and SEM images from 10 repetitive scratches at this load and on the two roughened samples are shown in Figure 5.9. For roughened 60NiTi/PDA/PTFE, the tip reached the substrate around the 3rd scratch and the SEM image taken after 10 scratches shows a tear in the coating that spans the full scratch length (Figure 5.9c). The tear was narrower than the wide tear that formed on polished 60NiTi/PDA/PTFE at 2250 μN (Figure 5.7) because the roughened substrate resisted coating delamination. The substrate is clearly exposed throughout the entire scratch length; however, there are valleys of the substrate surface that retained PDA/PTFE within the center of the scratched area. On roughened 60NiTi/PDA/PTFE + 0.25 wt% GPs, the coating compacted into a

layer with nearly 200 nm of thickness throughout of entire scratch length. Once again, due to improved PTFE particle cohesion, no significant tear was formed in the GP-containing coating on the roughened substrate, and the substrate was not exposed.

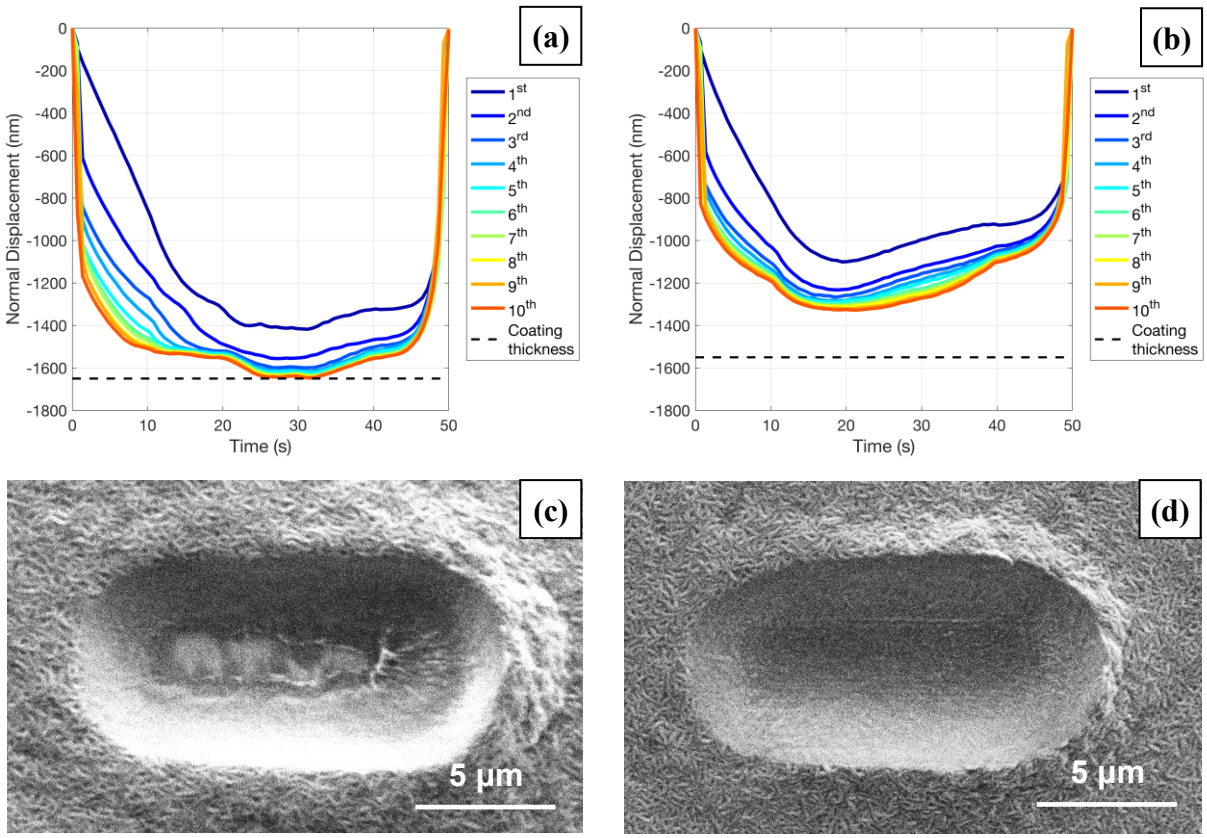

Figure 5.9. Normal displacement vs. time plots for 10 repetitive scratches at 2250 uN load on (a) roughened 60NiTi/PDA/PTFE and (b) roughened 60NiTi/PDA/PTFE + 0.25 wt% GPs and (c),(d) the corresponding SEM images after 10 scratches, respectively.

At the 2500 µN scratch load, the repetitive scratches were finally able to expose the substrate of roughened 60NiTi/PDA/PTFE + 0.25 wt% GPs. The displacement plots and SEM images from 10 repetitive scratches at 2500 µN on the coatings with and without GPs on the roughened substrate are shown in Figure 5.10. In the SEM images, both samples show that over half of the scratch length had exposed substrate after 10 scratches. However, the process of the tip reaching the substrate was much different for the two samples. On roughened

60NiTi/PDA/PTFE, a majority of the coating was displaced during the first scratch. A large amount of build-up to the right of the scratched area shown in the SEM image (Figure 5.10c) indicates that the coating was torn and severely plowed during the first scratch rather than being compacted in place. The lack of additional normal displacement from the 2nd through 10th scratch alongside the clearly exposed substrate in the SEM image after 10 scratches indicates that the tip contacted the substrate on the second scratch. In contrast, roughened 60NiTi/PDA/PTFE + 0.25 wt% GPs retained over 300 nm of the compacted coating during the first scratch. Then, subsequent scratches increased the normal displacement until the substrate was reached on the 6th scratch. The smaller fraction of coating thickness that was deformed by the first scratch and the gradual increase in displacement during subsequent scratches showed that roughened

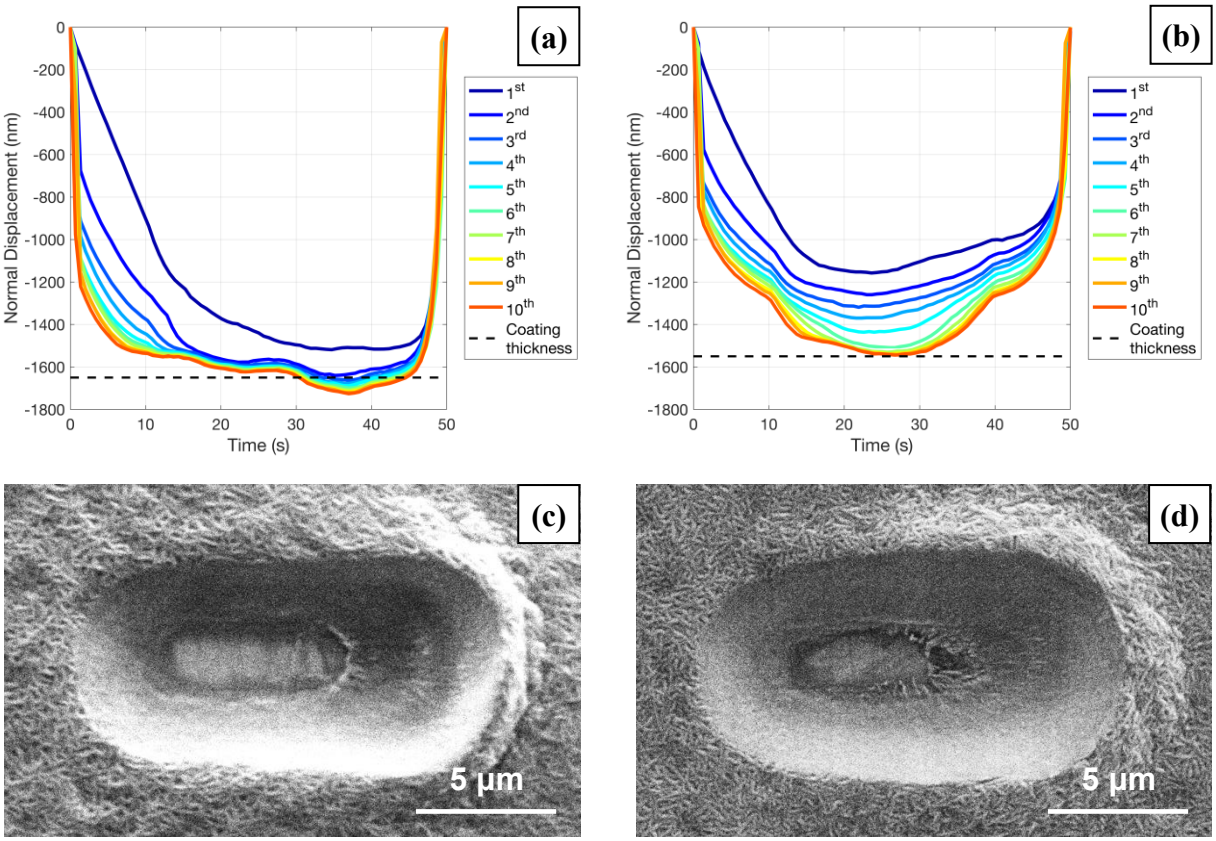

Figure 5.10. Normal displacement vs. time plots for 10 repetitive scratches at 2500 uN load on (a) roughened 60NiTi/PDA/PTFE and (b) roughened 60NiTi/PDA/PTFE + 0.25 wt% GPs and (c),(d) the corresponding SEM images after 10 scratches, respectively.

60NiTi/PDA/PTFE + 0.25 wt% GPs coating was more resistant to plowing and large tears of the coating than roughened 60NiTi/PDA/PTFE, again, owing to the better coating cohesion brought by the addition of the GPs.

Lastly, displacement versus time plots and SEM images from 10 repetitive scratches at 2750 μN on the coatings on the roughened substrate are shown in Figure 5.11. Again, the sample with GPs incorporated in the PTFE layer showed much more favorable performance. The 1st scratch on roughened 60NiTi/PDA/PTFE removed a majority of the coating, and the next two scratches removed the remaining PDA/PTFE except for the coating retained inside of the deeper roughness grooves, as shown in the displacement plot in Figures 5.11a and c. For roughened 60NiTi/PDA/PTFE + 0.25 wt% GPs, the first scratch left over 300 nm of compacted coating, and a low point in the displacement plot is shown in the center of the scratch near t = 23 s (Figure 5.11b). Subsequent scratches showed gradual increases in displacement as the coating was further compacted and partially removed. The tip appeared to reach the substrate for the first time during the 7th scratch and near the end of the scratch. The low point of the first scratch observed in the displacement plot at t = 23 s transitioned to being a high point in the scratch displacement at the 5th scratch and all that followed it. This transition can be understood from the following reasoning. In Figure 5.11d, the SEM image after 10 scratches on the sample containing GPs, the center of the scratch is shown to retain the compacted coating. This portion of retained coating corresponds to the high point observed at t = 23 s on the displacement plot. Because this section of the scratch area deformed the most during the first scratch, it is likely that there is a valley in the substrate at this location. The valley enabled more coating to be compacted in that area, and it secured the compacted coating in place throughout all ten scratches. Although

desirable substrate valleys were observed in the SEM of the scratched area of roughened 60NiTi/PDA/PTFE without GPs, the valleys were not able to retain the compacted coating that bridged across the width of the scratch. This further supports that the addition of GPs in PTFE improves the cohesion of the coating and thus improved the ability of the coating to mechanically interlock with the valleys of the substrate roughness.

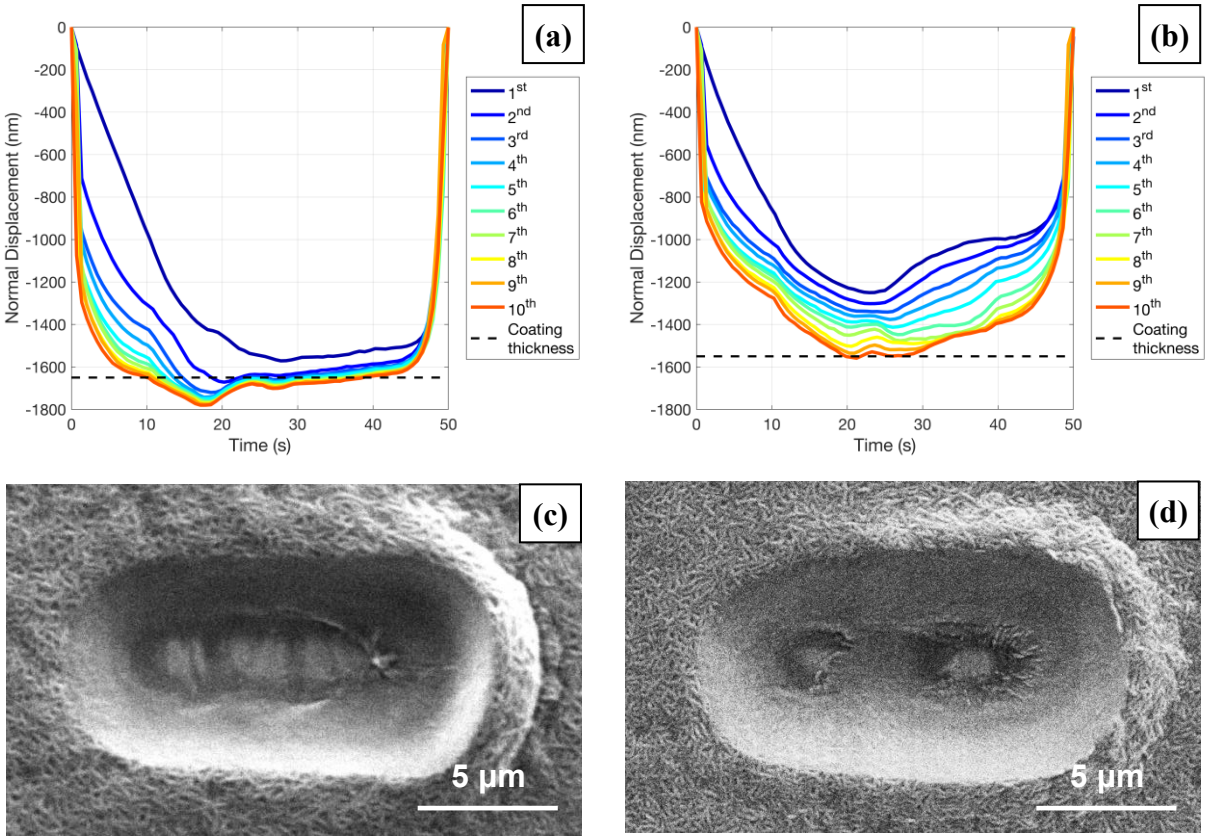

Figure 5.11. Normal displacement vs. time plots for 10 repetitive scratches at 2750 uN load on (a) roughened 60NiTi/PDA/PTFE and (b) roughened 60NiTi/PDA/PTFE + 0.25 wt% GPs and (c),(d) the corresponding SEM images after 10 scratches, respectively.

It is surprising that adding GPs only improved the coating scratch resistance on the roughened substrate but not on the polished substrate. However, this can be explained by the different wear and failure mechanisms of the coatings that can be seen in the SEM images of one scratch at 2750 µN on each coating in Figure 5.12. Polished 60NiTi/PDA/PTFE (Figure 5.12a)

and polished 60NiTi/PDA/PTFE + 0.25 wt% GrP (Figure 5.12b) both failed by coating global delamination from the substrate due to weak adhesion between the coatings and the polished substrate. The global delamination originated from wide tears that form due to large tensile stresses behind the tip as it plows through the coating. The improved cohesion of the coating with GPs did not enhance the coating scratch resistance on the polished substrate because the adhesion to the substrate was the weaker link. However, when a roughened substrate was used, the substrate roughness provided numerous barriers to coating delamination (Figures 5.12c and d). The coating without GPs tore within the PTFE layer due to cohesive failure (Figure 5.12c), and the coating with GPs retained a smooth and compacted layer of coating throughout the scratch due to the improved cohesion provided by the GPs (Figure 5.12d).

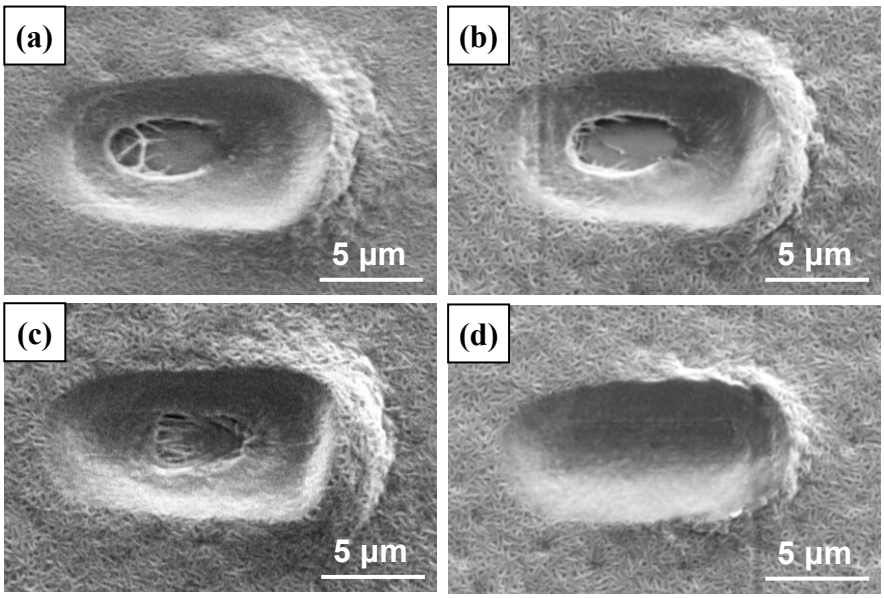

Figure 5.12. SEM images after one scratch at 2750 µN load on (a) polished 60NiTi/PDA/PTFE, (b) polished 60NiTi/PDA/PTFE + 0.25 wt% GPs, (c) roughened 60NiTi/PDA/PTFE, and (d) roughened 60NiTi/PDA/PTFE + 0.25 wt% GPs.

To concisely summarize the large set of data gathered during this study, the 3-D stem plots in Figure 5.13 were created and show the maximum displacement recorded during each of

the ten scratches at each load for each of the four sample types. For all four sample types, the tip did not reach the substrate after ten scratches at loads of 1500 and 1750 µN. At these loads, the coatings were compacted to form a thin layer of compacted and uniform coating. At the 2000 µN scratch load, the tip reached the substrate after a few scratches on polished 60NiTi/PDA/PTFE and polished 60NiTi/PDA/PTFE + 0.25 wt% GPs. The substrate was partially exposed during the final few scratches at 2000 µN on roughened 60NiTi/PDA/PTFE. However, roughened 60NiTi/PDA/PTFE + 0.25 wt% GPs retained nearly 300 nm of the compacted coating after ten scratches at 2000 µN, and this sample didn't experience substrate exposure until the sixth scratch

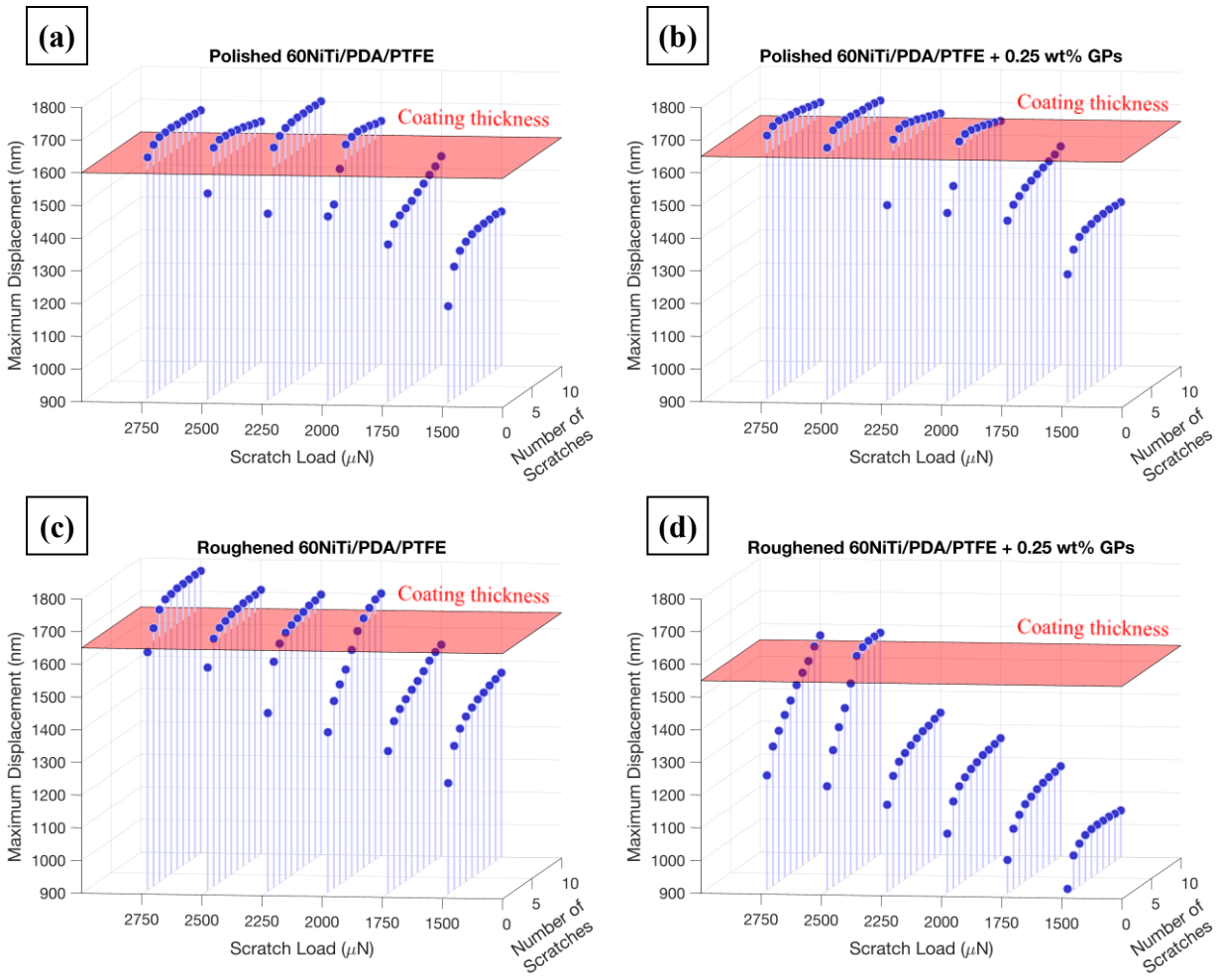

Figure 5.13. Maximum displacement during each of the ten scratches at each load for (a) polished 60NiTi/PDA/PTFE, (b) polished 60NiTi/PDA/PTFE + 0.25 wt% GPs, (c) roughened 60NiTi/PDA/PTFE, and (d) roughened 60NiTi/PDA/PTFE + 0.25 wt% GPs.

at 2500 μN. The data is also summarized in Table 5.2, which shows the number of scratches before the tip reached the substrate and the length of the exposed substrate after ten scratches.

Table 5.2. Number of scratches before the tip reached the substrate and the length of exposed substrate after 10 scratches.

Scratch Load (μN)	Polished 60NiTi/PDA /PTFE	Polished 60NiTi/ PDA/PTFE + 0.25 wt% GPs	Roughened 60NiTi/PDA /PTFE	Roughened 60NiTi/ PDA/PTFE + 0.25 wt% GPs
2000	4 scratches	3 scratches	6-8 scratches	>10 scratches
	4.6 μm	4.2 μm	2.2 μm	0 μm
2250	2 scratches	2 scratches	3 scratches	>10 scratches
	5.8 μm	5.4 μm	6.7 μm	0 μm
2500	2 scratches	1-2 scratches	2 scratches	7-8 scratches
	6.2 μm	6.8 μm	6.0 μm	4.3 μm
2750	1 scratch	1-2 scratches	2 scratches	7 scratches
	7.6 μm	7.0 μm	5.9 μm	3.5 μm

5.4 Discussion

The trends observed in this study mirrored those that were found from macro-scale tribometer scratch testing [17]. In both instances, PDA/PTFE + 0.25 wt% GPs on roughened substrate performed the best and showed plastic deformation and compaction of the coating rather than the delamination and plowing that occurred during failure of PDA/PTFE coating without GPs and on the roughened substrate. However, the nanoindenter scratch tests and SEM imaging performed in this study were able to provide more detailed explanations for the improved behavior and precisely measure the thickness of the compacted layer of the coating during scratching. Additionally, the SEM imaging of the repetitive scratches showed how the morphology of the PTFE layer changed after it was compacted.

This study also provided new insights into the mechanisms that drive the effects of substrate roughness on PDA/PTFE coatings [16]. The previous study explained that mechanical interlocking of the coating with a roughened substrate surface improved the coating's durability [16]. However, this study showed how the mechanical interlocking of the coating with a roughened surface resists the formation and propagation of coating tears near the substrate surface by reducing the tensile stresses in the coating. This study also showed how tears formed, expanded, and led to coating delamination upon scratch when the PDA/PTFE and PDA/PTFE + 0.25 wt% GPs coatings were deposited on polished substrates.

Lastly, this work contributed to the understanding of how adding particles to the PTFE layer of PDA/PTFE coatings improves tribological performance [10-12,14-15,17]. The improved cohesion of coatings with GPs on the roughened substrate made it the most resistant to tearing and plowing, and it did not exhibit global delamination of the coating from the substrate. Furthermore, the enhanced cohesion of the coatings with GPs on the roughened substrate showed an improvement in the mechanical interlocking of coating with the substrate roughness compared to coating without GPs.

5.5 Conclusions

Repetitive nanoindenter scratch testing proved to be a useful method for investigating the scratch behavior of thin PTFE-based coatings and differentiating the effects that substrate roughness and the incorporation of GPs have on the coating performance. Roughening the substrate provided resistance to coating delamination and global removal due to mechanical interlocking between the coating and the grooves of the substrate roughness. This mechanical

interlocking reduced tensile stresses in the coating near the coating/substrate interface and resisted tears from splitting through the coating to the substrate and widening across the substrate. Adding GPs enhanced PTFE particle cohesion which provided stronger interlocking with the roughened substrate and higher resistance to tears and plowing. The combination of a roughened substrate and PDA/PTFE with GPs enabled the coating to compact and stabilize as a 200-300 nm thick layer of durable compacted coating. For these reasons, PDA/PTFE + 0.25 wt% GPs on a substrate with a valley-dominated, roughened surface shows promising potential as a solid lubricant coating for tribological applications where repetitious high-pressure sliding is encountered.

5.6 Acknowledgements

We thank the National Aeronautics and Space Administration (NASA) for the support under NASA Award No: 80NSSC17M0020 and Dr. Adam Howard at the NASA Glenn Research Center (GRC) for serving as our NASA Technical Monitor and Technical Contact. We also thank Dr. Christopher DellaCorte for serving as our Technical Contact and providing the 60NiTi samples. Additionally, we thank the Arkansas Biosciences Institute and the University of Arkansas for major equipment funding support.

5.7 References

[1] R. Neupane, Z. Farhat, Wear Resistance and Indentation Behavior of Equiatomic Superelastic TiNi and 60NiTi, Mater. Sci. Appl. 6 (2015) 694-706. http://dx.doi.org/10.4236/msa.2015.67071.

[2] C. DellaCorte, S.V. Pepper, R.D. Noebe, D.R. Hull, G. Glennon, Intermetallic Nickel-Titanium Alloys for Oil-Lubrication Bearing Applications, NASA/TM—2009-215646, 2009. https://ntrs.nasa.gov/citations/20090019112.

[3] C. DellaCorte, L.E. Moore III, J.S. Clifton, Static Indentation Load Capacity of the Superelastic 60NiTi for Rolling Element Bearings, NASA/TM—2012-216016, 2012. https://ntrs.nasa.gov/citations/20120012907.

[4] C. DellaCorte, W.A. Wozniak, Design and Manufacturing Considerations for Shockproof and Corrosion-Immune Superelastic Nickel-Titanium Bearings for a Space Station Application, NASA/TM-2012-216015, 2012. https://ntrs.nasa.gov/citations/20130001675.

[5] C. DellaCorte, M.K. Stanford, T.R. Jett, Rolling Contact Fatigue of Superelastic Intermetallic Materials (SIM) for Use as Resilient Corrosion Resistant Bearings, Tribol. Lett. 57 (2015). https://doi.org/10.1007/s11249-014-0456-3.

[6] K. Khanlari, M. Ramezani, P. Kelly, P. Cao, T. Neitzert, Reciprocating Sliding Wear Behavior of 60NiTi As Compared to 440C Steel under Lubricated and Unlubricated Conditions, Tribol. Trans. 61 (2018) 991-1002. https://doi.org/10.1080/10402004.2018.1460434.

[7] C. DellaCorte, F. Thomas, O.A. Leak, Tribological Evaluation of Candidate Gear Materials Operating under Light Loads in Highly Humid Conditions, NASA/TM—2015-218896, 2015. https://ntrs.nasa.gov/citations/20150023048.

[8] H. Lee, Bioadhesion of Mussels and Geckos: Molecular Mechanics, Surface Chemistry, and Nanoadhesives, Doctoral Dissertation: Northwestern University, Evanston, Illinois, 2008. https://doi.org/10.21985/N2TT7W.

[9] S. Beckford, M. Zou, Wear Resistant PTFE Thin Film Enabled by a Polydopamine Adhesive Layer, App. Surf. Sci. 292 (2014) 350-356. https://doi.org/10.1016/j.apsusc.2013.11.143.

[10] S. Beckford, M. Zou, The Effects of Graphite Filler on the Tribological Properties of Polydopamine/PTFE Coatings, Tribol. Lett. 64 (2016) 42-53. https://doi.org/10.1007/s11249-016-0777-5.

[11] S. Beckford, J. Cai, J. Chen, M. Zou, Use of Au Nanoparticle-Filled PTFE Films to Produce Low-Friction and Low-Wear Surface Coatings, Tribol. Lett. 56 (2014) 223- 230. https://doi.org/10.1007/s11249-014-0402-4.

[12] S. Beckford, L. Mathurin, J. Chen, M. Zou, The Influence of Cu Nanoparticles on the Tribological Properties of Polydopamine/PTFE + Cu Films, Tribol. Lett., 59 (2015) 1-9. https://doi.org/10.1007/s11249-015-0543-0.

[13] S.K. Ghosh, C. Miller, D. Choudhury, J.A. Goss, M. Zou, The Effects of PTFE Thickness on the Tribological Behavior of Thick PDA/PTFE Coatings, Tribol. Trans. 63 (2020) 575-584. https://doi.org/10.1080/10402004.2020.1728001.

[14] F. Soltani-Kordshuli, D. Okyere, J. Chen, C. Miller, N. Harris, M. Afshar-Mohajer, S. Ghosh, M. Zou, Tribological Behavior of the PDA/PTFE+ Cu-SiO_2 Nanoparticle Thin Coatings, Surf. Coat. Technol. 409 (2021). https://doi.org/10.1016/j.surfcoat.2021.126852.

[15] S. Beckford, L. Mathurin, J. Chen, R. Fleming, M. Zou, The effects of polydopamine coated Cu nanoparticles on the tribological properties of polydopamine/PTFE coatings, Tribol. Int. 103 (2016) 87-94. https://doi.org/10.1016/j.triboint.2016.06.031.

[16] C. Miller, D. Choudhury, M. Zou, The Effects of Surface Roughness on the Durability of Polydopamine/PTFE Solid Lubricant Coatings on NiTiNOL 60, Tribol. Trans. 62 (2019) 919-929. https://doi.org/10.1080/10402004.2019.1641645.

[17] D. Choudhury, C. Miller, M. Zou, Tribological performance of PDA/PTFE+ Graphite particle coatings on 60NiTi, Appl. Surf. Sci. 527 (2020). https://doi.org/10.1016/j.apsusc.2020.146731.

[18] D. Choudhury, C. Miller, N. Harris, M. Zou, The effect of coating thickness on the tribological properties of polydopamine/PTFE+ graphite particle coatings on 60NiTi, Surf. Coat. Technol. 420 (2021). https://doi.org/10.1016/j.surfcoat.2021.127320.

[19] C. Miller, M. Zou, Microscale friction and deformation behavior of polydopamine/polytetrafluoroethylene-coated 60NiTi from nanoscratch tests, Thin Solid Films 743 (2022). https://doi.org/10.1016/j.tsf.2021.139079.

[20] C. Miller, C. DellaCorte, M. Zou, Nanomechanical properties of hardened 60NiTi, Mater. Sci. Eng.: A, 800 (2021). https://doi.org/10.1016/j.msea.2020.140284.

[21] A. Leyland, and A. Matthews, On the significance of the H/E ratio in wear control: a nanocomposite coating approach to optimised tribological behaviour, Wear, 246 (2000). https://doi.org/10.1016/S0043-1648(00)00488-9.

CHAPTER 6

PDA/PTFE-COATED BALL BEARINGS

6.1 Introduction

60NiTi has been proposed as a candidate material for various ball bearing applications on the International Space Station [1–9], and the promising tribological performance of 60NiTi/PDA/PTFE suggests that this coating is a viable solid lubricant option for these applications [10–14]. However, PDA/PTFE has not been applied or tested as a ball bearing lubricant. Therefore, the goal of this chapter is to establish the feasibility of PDA/PTFE as a ball bearing lubricant and to present the promising preliminary results. The material in this chapter plays an important role in the larger scope of this dissertation because it begins bridging the gap between a target 60NiTi/PDA/PTFE application (ball bearings) and developmental tribological testing on 25.4 x 25.4 x 2 mm flat plate test specimens. Additionally, this work lays a foundation for future research, and it is closely tied to the recommendations for future work laid out in Chapter 7.

This chapter is organized using a top-down approach to emphasize the initial results before providing detailed discussion of the coating development and bearing tester design. First, a summary of the results is provided in section 6.2, and a broad overview to the testing methods is given in section 6.3. The detailed results of preliminary bearing tests are presented and discussed in sections 6.4–6.5. The processes developed to coat bearing components with PDA/PTFE and PDA/PTFE+GPs are presented in section 6.6, and a more detailed description of the bearing tester design is in section 6.7.

6.2 Summary of Results

Methods were successfully developed to apply PDA/PTFE and PDA/PTFE+GPs coatings to the balls and races of ball bearings. Furthermore, the coated components were reassembled to produce functioning Si_3N_4/440C hybrid ball bearings with solid lubricant coatings, and the custom bearing tester was able to test bearings with controlled speed and radial load. The vibration data from the accelerometer on the bearing tester was able to detect global failure of a non-lubricated bearing and was useful for comparing the behavior of a PDA/PTFE+GPs coated bearing compared to a greased bearing.

A dry bearing was tested so that bearing failure due to insufficient lubrication could be observed. During a 5-min test at 1140 rpm and 230 lb radial load, the dry bearing experienced severe failure. This failure was easily recognizable by high-amplitude vibrations in the raw accelerometer data, random broadband frequencies across the vibration spectrum, and by post-test imaging of the bearing components. The inner race of the failed bearing showed heat discoloration, cracks, and severe spalling.

The PDA/PTFE-coated bearing was disassembled and imaged after 5 min and 3 h of testing to study the coating behavior on the bearing balls and inner race. Images after the 5-min test showed that the coating was mostly removed from the balls. However, after 3 h of extended testing, a significant amount of transfer film developed on the balls. The inner race had large coating fragments scattered across it after the 5 min test, but the fragments were compacted to form a smoother and more uniform layer on the inner race after 3 h of extended testing. No signs

of failure such as heat discoloration, cracks, or spalling were observed on the inner race of the PDA/PTFE-coated bearing.

A PDA/PTFE+GPs-coated bearing also showed promising performance during a 3 h test. The vibration spectra of the PDA/PTFE+GPs-coated bearing throughout a 15-min test were compared to those of a greased bearing. The greased bearing ran smoother than the coating bearing, and a pronounced difference was observed near the ball pass frequency inner (BPFI). The coated bearing had 2-3 times higher peaks near the BPFI. This was possibly caused by balls rolling over uneven clumps of coating on the inner race of the bearing.

6.3 Experimental Methods

Hybrid R8 deep groove ball bearings (0.5 in bore) with 440C races and Si_3N_4 balls were used for proof-of-concept. The test bearing size (0.5 in bore) and bearing materials were chosen to match the compressor bearings on the International Space Station wastewater purifier, which are a candidate application for 60NiTi [1]. The 440C material was used instead of 60NiTi because the 60NiTi balls are expensive and hard to obtain and it will produce useful test results. PDA/PTFE-based solid lubricant coatings have shown strong performance on stainless steel alloys [15–17], so the coating was expected to function well on the 440C races. A custom bearing tester was designed and built to test the R8 bearings at variable speeds up to 2000 rpm and variable radial loads. The bearing tester is pictured in Figure 6.1. The shaft is coupled to an AC servo motor (EMG-20, Anaheim Automation, USA) that has a rated speed of 2000 rpm and a 2-kW power rating.

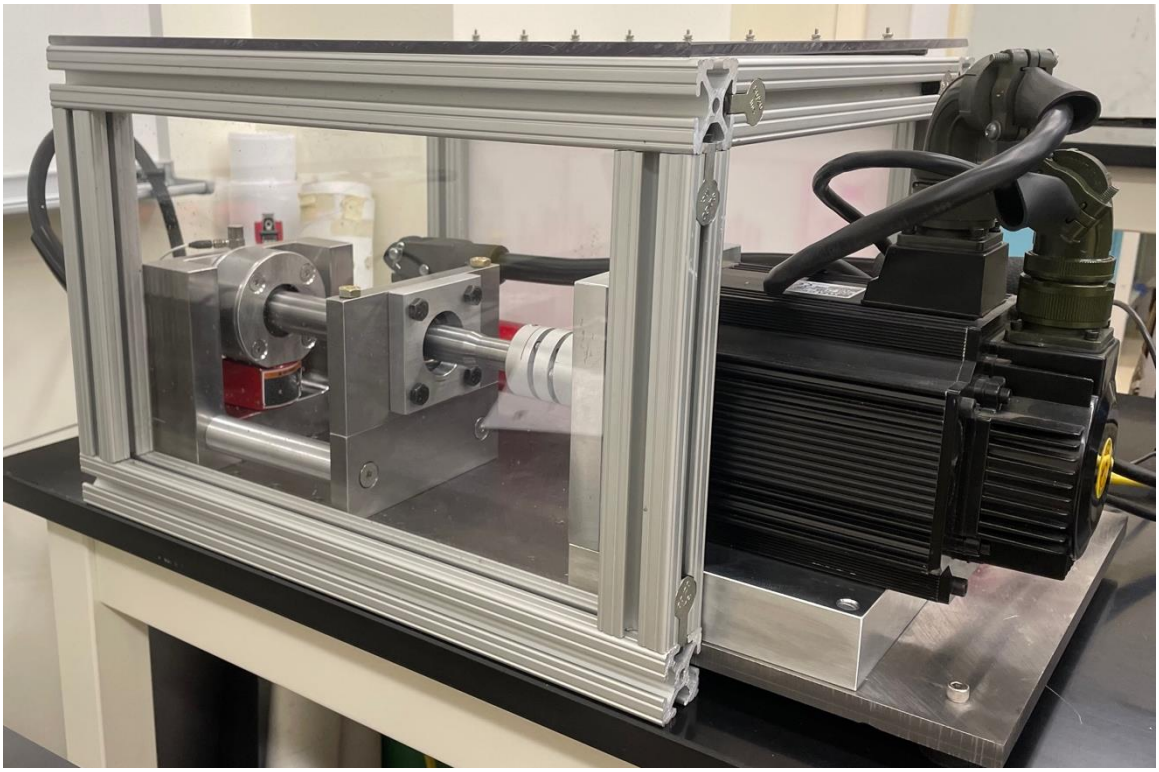

Figure 6.1. Bearing tester.

The bearing balls, inner race, and outer race were coated with PDA/PTFE or PDA/PTFE+GPs to produce solid-lubricated bearings. Additional tests were performed on dry (non-lubricated) and greased bearings for comparison. Bearings were tested at 1140 rpm and a radial load of 200–230 lb, and an accelerometer measured vibration during testing. The vibration data was converted to a frequency domain spectrum for bearing analysis. The tests were periodically stopped, and the bearings were disassembled so that the components could be inspected and imaged.

The bearings and bearing components were imaged using a camera (iPhone 12, Apple, USA) and 3D laser-scanning confocal microscope (VK-X260K, Keyence Corporation of America, USA). The camera was used to image the bearing races and the balls from a familiar

frame of reference. Global failure of the bearings through severe spalling and discoloration were evident through the low-magnification lens. Furthermore, large flakes of displaced coating were shown more clearly by this form of imaging. The 3D laser-scanning confocal microscopy (3DLSCM) provided detailed analysis of the wear mechanisms on the bearing races, the morphology of the intact coating on the bearing races, and the transfer films that developed on the counterface surfaces.

6.4 Results and Discussion

The bearing tester and data acquisition methods were still being developed and improved as the preliminary results were gathered. However, the results show proof-of-concept and should motivate further exploration of ball bearings lubricated with PDA/PTFE-based solid lubricant coatings. Dry (non-lubricated) bearings and a greased bearing were tested to provide points of comparison for the coated bearings. Table 6.1 details the various bearings and the tests that were performed on each of them. The first round of testing (Round 1) included tests on a dry bearing (Bearing 1) and a PDA/PTFE-coated bearing (Bearing 2). Bearing 1 and Bearing 2 were tested for 5 min and the test was stopped so that the bearings could be disassembled and inspected. No damage was observed on the PDA/PTFE-coated bearing (Bearing 2) after 5 min of testing (Test 1), so it was reassembled and tested for an additional 3 h (Test 2). After the first round of testing, modifications were made to the bearing tester to improve the force application system. Then, in a second round of testing, a grease-packed and sealed bearing (Bearing 3) and a PDA/PTFE+GPs-coated bearing (Bearing 4) were tested. Bearing 3 was tested for 15 min at 1140 rpm and 200 lb radial load and Bearing 4 was tested for 3 h at 1140 rpm and 200 lb radial load.

Table 6.1. Bearings used for testing.

	Bearing	Races	Balls	Cage	Lubricant	Test 1	Test 2
Round 1	**Bearing 1**	440C	Si3N4	PEEK	Dry	5 min, 1140 rpm, 230 lb	-
	Bearing 2	440C	Si3N4	PEEK	PDA/PTFE	5 min, 1140 rpm, 230 lb	3 h, 1140 rpm, 230 lb
Round 2	**Bearing 3**	440C	Si3N4	PTFE	Kyodo SRL Grease	15 min, 1140 rpm, 200 lb	-
	Bearing 4	440C	Si3N4	PTFE	PDA/PTFE+GPs	3 h, 1140 rpm, 200 lb	-

6.4.1 Round 1 of Testing

A dry bearing and PDA/PTFE-coated bearing were tested at 1140 rpm and 230 lb radial load for 5 min. After 5 min of testing, data acquisition and the motor were stopped, and the load was removed. The test bearing was removed from the shaft, disassembled, and the balls and inner race were imaged. The raw acceleration data from these tests are shown in Figure 6.2. The rotational speed of the motor was increased from 0 to 1140 rpm at t = 10 s and then the speed was held constant at 1140 rpm for the next 5 min. In Figure 6.2, note the difference in amplitude on the y-axis of each plot. Within the first few minutes of testing, the dry bearing developed high amplitude vibrations that indicated that the bearing was damaged (Figure 6.2 (a)). The increase in noise was audible and pronounced. However, the PDA/PTFE-coated bearing maintained lower amplitude vibration throughout the 5 min of testing (Figure 6.2 (b)).

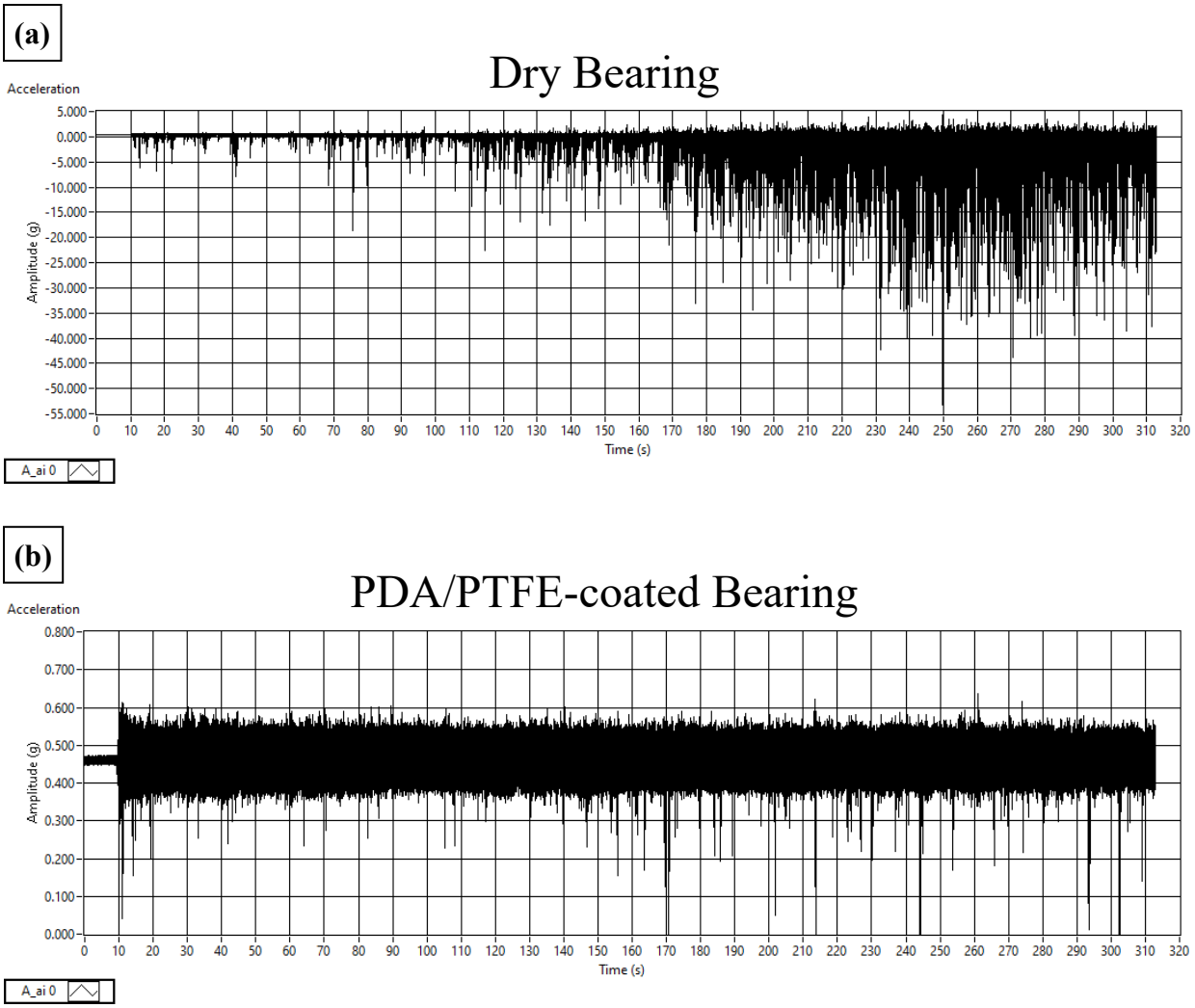

Figure 6.2. Acceleration versus time plots of the raw acceleration data from the 5 min tests of (a) dry and (b) PDA/PTFE-coated bearings at 1140 rpm and 230 lb radial load. The motor speed was 0 at t = 0 s and was increased to 1140 rpm at t = 10 s.

The vibration data during bearing tests was analyzed by converting the acceleration time domain waveform to a frequency domain spectrum using a fast Fourier transform (FFT). The frequency spectra from 0-8000 Hz at 5 min of testing are shown in Figure 6.3. The dry bearing had high-magnitude vibrations that created a random broadband spectrum. This is indicative of severe bearing failure [15]. The coated bearing had lower-magnitude vibrations across the spectrum with peaks or bands of stronger vibration. However, the magnitudes of the peak

vibrations were much lower for the coated bearing than the dry bearing across the entire spectrum.

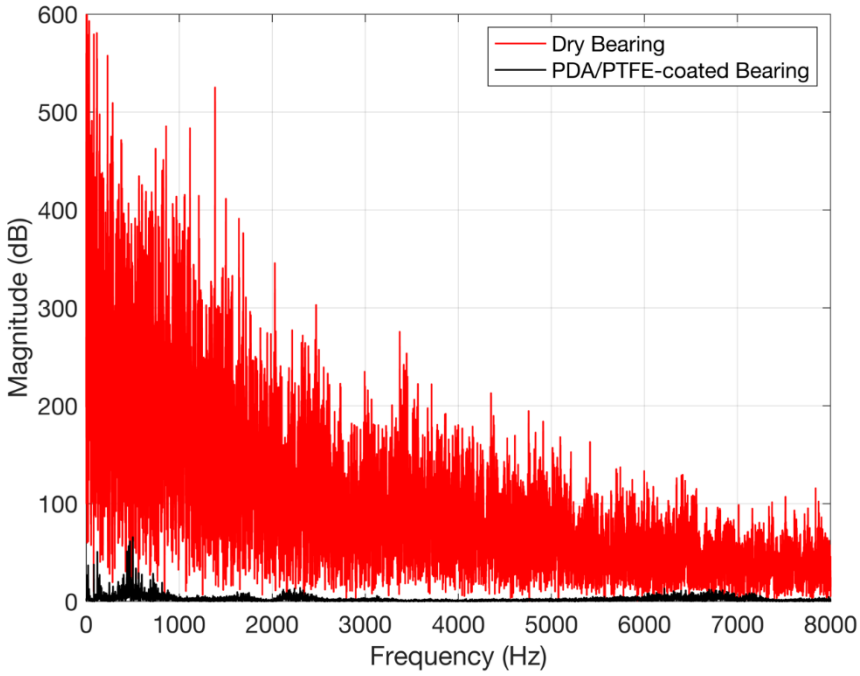

Figure 6.3. Frequency spectra generated from an FFT of the vibration data at the end of the 5 min tests on dry and PDA/PTFE-coated bearings.

The dry bearing was removed from the test rig, disassembled, and the components were imaged after the 5 min test. Images of the inner race before and after testing are shown in Figure 6.4. The inner race of the dry bearing before testing is shown in Figure 6.4 (a) and (c), and the race after testing is shown in Figure 6.4 (b) and (d). The low-magnification image in Figure 6.4 (b) shows discoloration and damage along the center of the race. The discoloration is indicative of high temperatures developing on the inner race, and the optical microscope image in Figure 6.4 (d) shows that the bearing experienced severe spalling. The higher magnification 3D image in Figure 6.5 shows cracks on the inner race and a large void where a spall broke free from the surface.

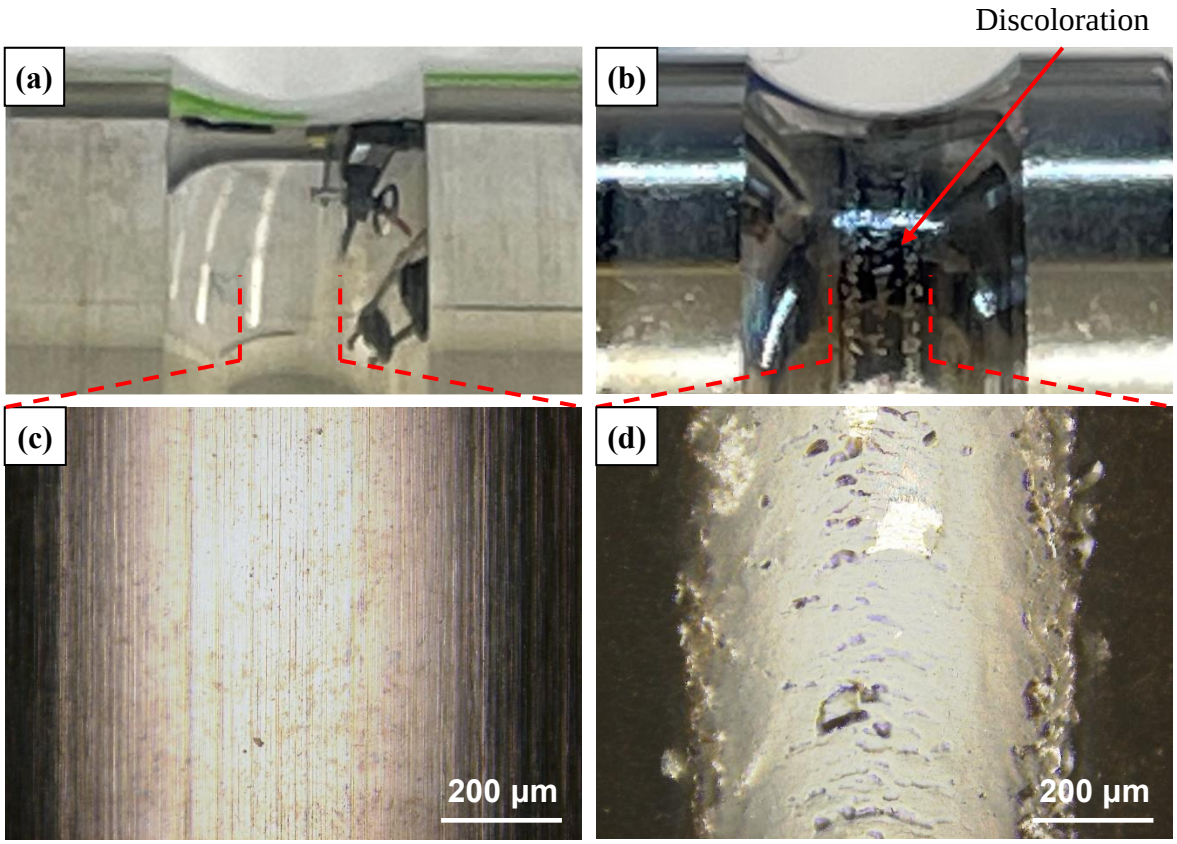

Figure 6.4. Photographs (top) and optical microscope images (bottom) of the inner race of the dry bearing (a)(c) before (left) and (b)(d) after (right) the 5 min test at 1140 rpm and 230 lb.

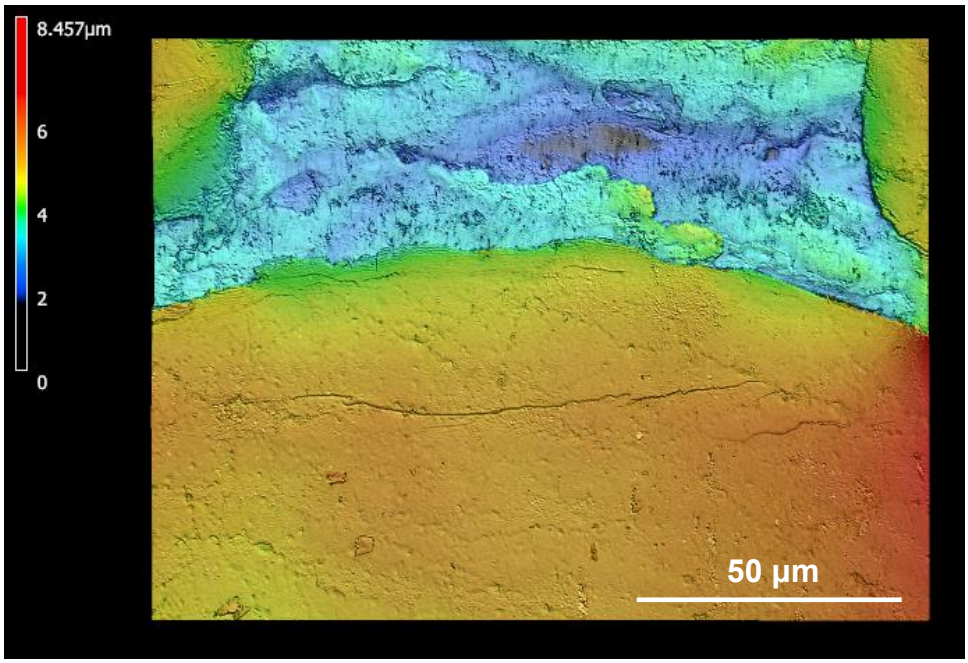

Figure 6.5. 3D image of the center of the inner race of the dry bearing showing cracks and spalling.

The center of the inner race of the coated bearing is shown in Figure 6.6. No discoloration was observed on the inner race and the polishing lines on the race surface are visible beneath the semi-transparent coating. This indicated that the coating provided sufficient lubrication during the brief 5-min test, and that further testing should be performed. The PDA/PTFE-coated bearing was reassembled and installed on the test rig for extended testing.

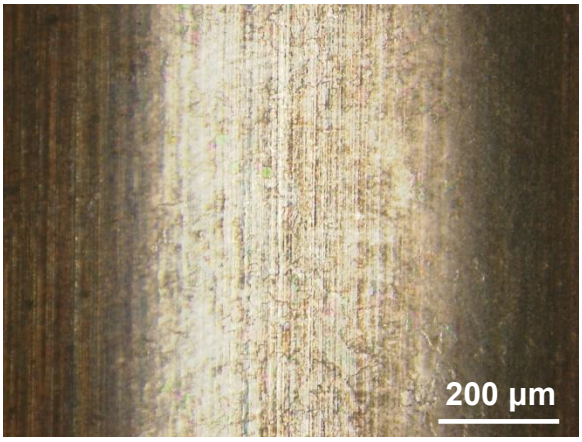

Figure 6.6. Optical image of the center of the inner race of the PDA/PTFE-coated bearing after 5 min test at 1140 rpm and 230 lb radial load.

The reassembled PDA/PTFE-coated bearing was run in the bearing tester for an additional 3 h at 1140 rpm and 230 lb radial load (Bearing 2, Test 2 in Table 6.1). The frequency spectra were monitored throughout testing and remained similar to the spectrum for the PDA/PTFE-coated bearing from Test 1 (Figure 6.3). After 3 h of testing, the motor was stopped, the radial load was released, and the test bearing was removed from the tester and disassembled for further analysis. A photograph and an optical microscope image of the center of the race before any testing and after the two tests (Test 1 and Test 2 in Table 6.1) are shown in Figure 6.7. A lighter-colored strip was visible in the center of the inner race where the balls had compacted and displaced the coating (Figure 6.7 (b)). However, the color of this strip closely resembled the race prior to PDA/PTFE coating and testing (Figure 6.7 (a)). Therefore, there were

no signs of discoloration on the bearing race due to excessive heat generation. The optical microscope image of the center of the inner race after testing (Figure 6.7 (d)) shows that race retained coating material and there are no visible signs of damage to the race itself.

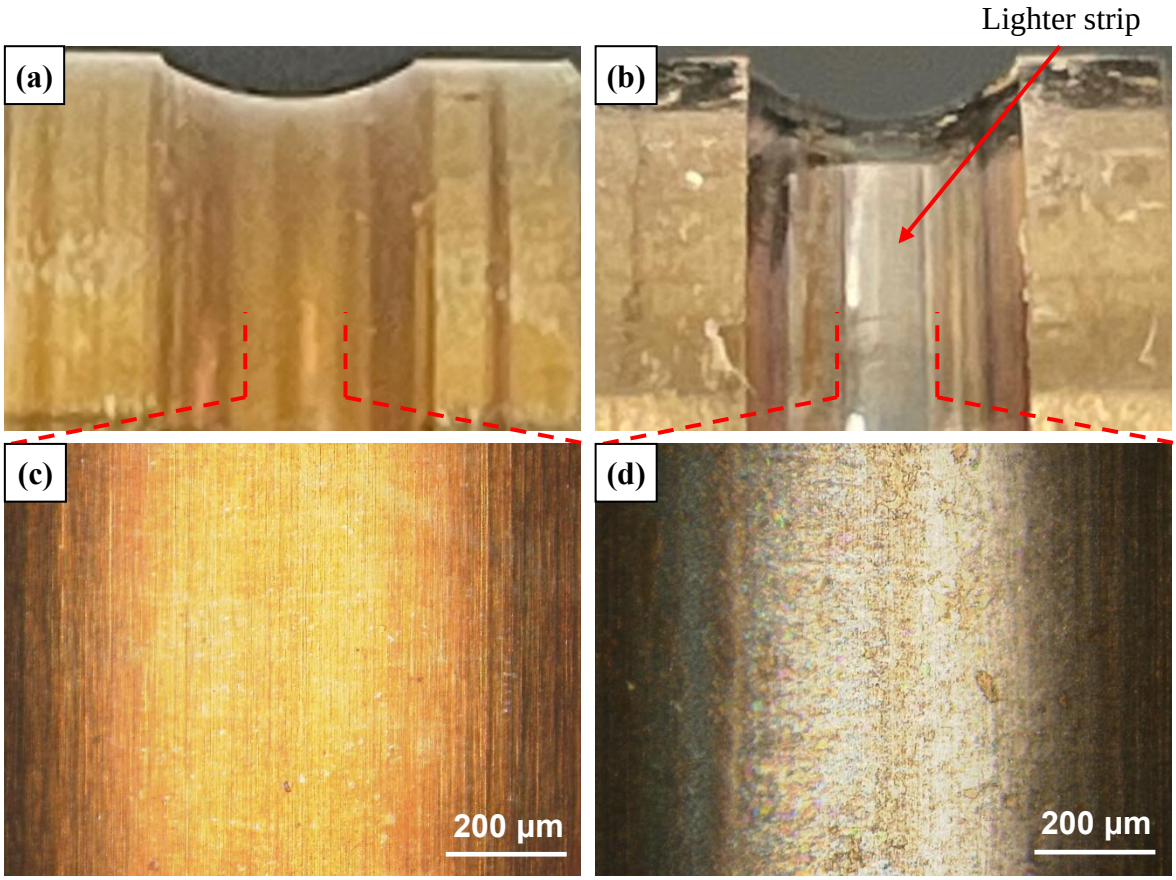

Figure 6.7. Photographs (top) and optical microscope images (bottom) of the inner race of the PDA/PTFE-coated bearing (a)(c) before any testing (left) and (b)(d) after (right) the additional 3 h test at 1140 rpm and 230 lb.

6.4.2 PDA/PTFE Coating Behavior as a Ball Bearing Lubricant

The PDA/PTFE coating did not require rigidity to effectively lubricate the ball bearing. Instead, the deformation of the coating led to a smoother running bearing and dislocated coating fragments were redeposited throughout the bearing races and balls. Therefore, despite deformation and dislocation, favorable PTFE-PTFE sliding occurs between the bearing

components. After the balls and races were coated and the bearing was reassembled, the bearing did not rotate smoothly. The coating introduced an initial negative clearance that resisted rotation. However, the coated bearing was rotated by hand for approximately 100 revolutions and the rotation smoothed. After this manual break-in, the bearing could be spun by hand and would revolve freely for several seconds. The smooth rotation was enabled by compaction and displacement of the coating material lessening the negative clearance in the bearing. In previous studies on flat substrates, PDA/PTFE coatings have been measured to have a higher coefficient of friction (COF) at the start of ball-on-disk tribometer tests before displaying prolonged durability with low COF from a very thin layer of coating near the substrate interface [13]. A similar robust thin layer is believed to have developed on the bearing races during this manual break-in and during the early stages of operation in the bearing testing.

The coating behavior was studied by comparing images of the bearing balls and inner races of the coated bearing after the 5-min test and after an additional 3 h of operation in the bearing tester. 3DLSCM images of balls from the coated bearing before testing, after the 5-min test, and after the additional 3 h test are shown in Figure 6.8 (a), (b), and (c), respectively. Initially, there was a layer of PDA/PTFE coating covering a majority of the surface (Figure 6.8 (a)). The coating largely disappeared after 5 min of testing (Figure 6.8 (b)). Instead, fragments of coating material were distributed across the surface of the ball with large, exposed areas between them. The initial PDA/PTFE coating on the balls likely delaminated from the very smooth Si_3N_4 surface. However, after an additional 3 h of operation in the bearing tester, the balls had substantial amounts of transfer film that was more evenly distributed across the surface (Figure 6.8 (c)). Multiple balls were imaged after each testing interval, and their appearances were very

similar. The initial removal and fragmentation of coating after the 5 min test was followed by favorable transfer films developing on the balls during the additional 3 h test.

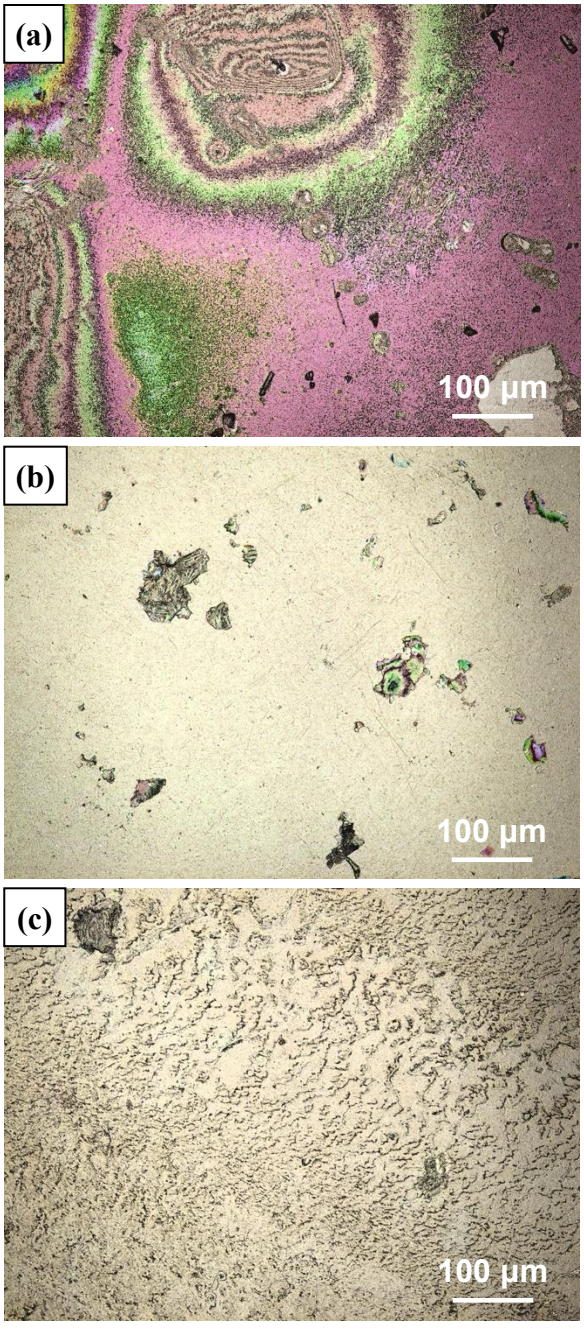

Figure 6.8. Laser-optical images of a bearing ball from the PDA/PTFE-coated bearing (a) before testing, (b) after the 5-min test, and (c) after the additional 3 h test.

Laser-optical, 3-D, and slope-adjusted 3-D images of the inner race of the PDA/PTFE-coated bearing after 5 min and an additional 3 h of testing at 1140 rpm and 230 lb radial load are shown in Figure 6.9. The set of images in Figure 6.9 (a), (c), and (e) are after 5 min of testing, and the set of images in Figure 6.9 (b), (d), and (e) are after an additional 3 h of testing. Each set of images was generated from a measurement taken in the center of the race. The coating behavior on the inner race had parallels to the behavior observed on the balls. After 5 min of testing, large fragments of coating were observed on the inner race. However, the coating fragments are more numerous on the inner race than the ball, and they cover a greater portion of the surface area. Some of the large coating fragments on the inner race likely originate from coating that was removed from the balls. The coating likely adheres to the races better than the balls due to the favorable surface roughness of the inner race promoting improved PDA/PTFE coating adhesion [13]. The different ball (Si_3N_4) and race (440C steel) material could also have affected coating adhesion. However, the performance of PDA/PTFE coatings on Si_3N_4 and 440C substrates has not been systematically studied and compared.

The inner race of the coated bearing after the additional 3 h test (Figure 6.9 (b), (d), and (e)) showed that coating material continued to sufficiently lubricate the inner race. Large fragments of coating were still visible on the inner race, but a compacted and smoother film covered the surface. The polishing lines on the surface of the inner race are easily visible between the coating fragments after the 5 min test (Figure 6.9 (a), (c), and (e)). However, the polishing lines are difficult to distinguish after the additional 3 h test (Figure 6.9 (b), (d), and (f)). It is unclear whether the polishing lines were obscured because they were covered by transfer

film or due to gradual wear of the race. Nonetheless, there were no signs of crack formation, spalling, or other significant damage to the inner race.

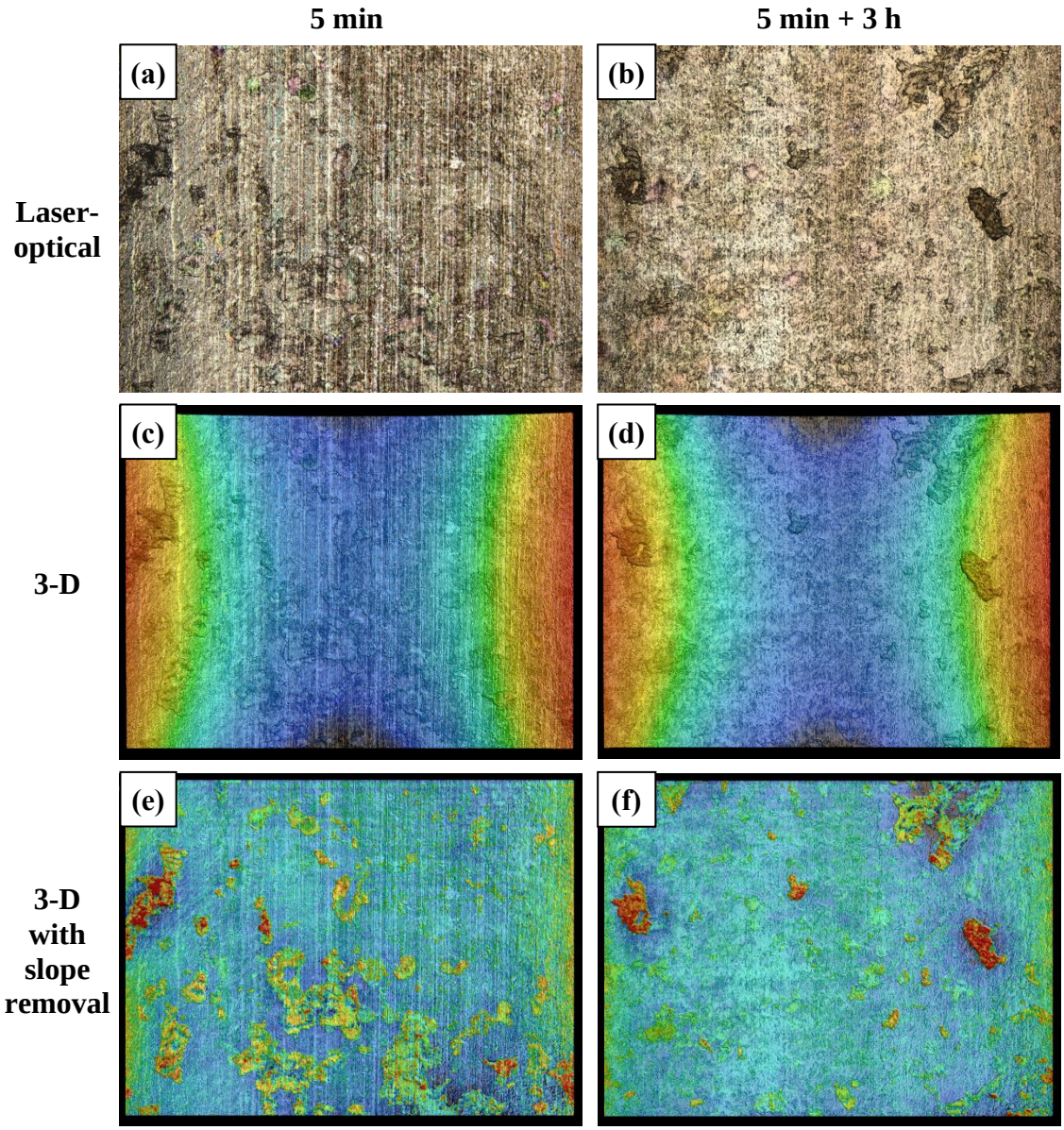

Figure 6.9. Images of the inner race of the PDA/PTFE-coated bearing after testing at 1140 rpm and 230 lb radial load for 5 min (left column) and an additional 3 h (right column). Laser-optical, 3-D, and 3-D with slope removal images are shown in (a) and (b), (c) and (d), and (e) and (f), respectively.

The first round of testing showed promising performance from the PDA/PTFE-coated bearing. However, the bearing tester and data acquisition systems needed to be refined. The

hydraulic jack did not allow radial load to be applied to the bearing with much precision, and the vibration data needed to be sampled and recorded incrementally throughout testing. Improvements were made to the bearing tester and the data acquisition software to address these shortcomings before a second round of testing was performed. Additionally, a bearing was coated with PDA/PTFE+0.25 wt% GPs for the second round of testing because this coating has been shown to have enhanced performance compared to PDA/PTFE coating [10,12,14,16].

6.4.3 Round 2 of Testing

In the second round of testing, a greased bearing and a PDA/PTFE+GPs-coated bearing were run in the bearing tester at 1140 rpm and 200 lb radial load. Waterfall plots of the vibration spectra at 1-min intervals are shown in Figure 6.10. The spectra are plotted from 1-8000 Hz for the greased bearing and PDA/PTFE+GPs-coated bearing in Figure 6.10 (a) and (b), respectively, and from 1-200 Hz for the greased and PDA/PTFE+GPs-coated bearing in Figure 6.10 (c) and (d), respectively. The 1-8000 Hz plots show that the greased bearing ran smoother than the PDA/PTFE+GPs-coated bearing throughout the 15 min tests. For both bearings, the high frequency vibrations in the 6000-8000 Hz range increased during the first 5 min of the test before normalizing.

The lower frequency vibrations (1-200 Hz) of the greased and PDA/PTFE+GPs-coated bearings are shown in Figure 6.15 (a) and (b), respectively. Harmonics of the rotation speed are visible at intervals of 19 Hz (19, 38, 57, 76, 95,…, Hz). The peaks at the second (38 Hz) and third (57 Hz) harmonic frequencies were greater for the coated bearing than the greased bearing,

which supports the general observation from Figure 6.10 that the greased bearing runs smoother than the coated bearing.

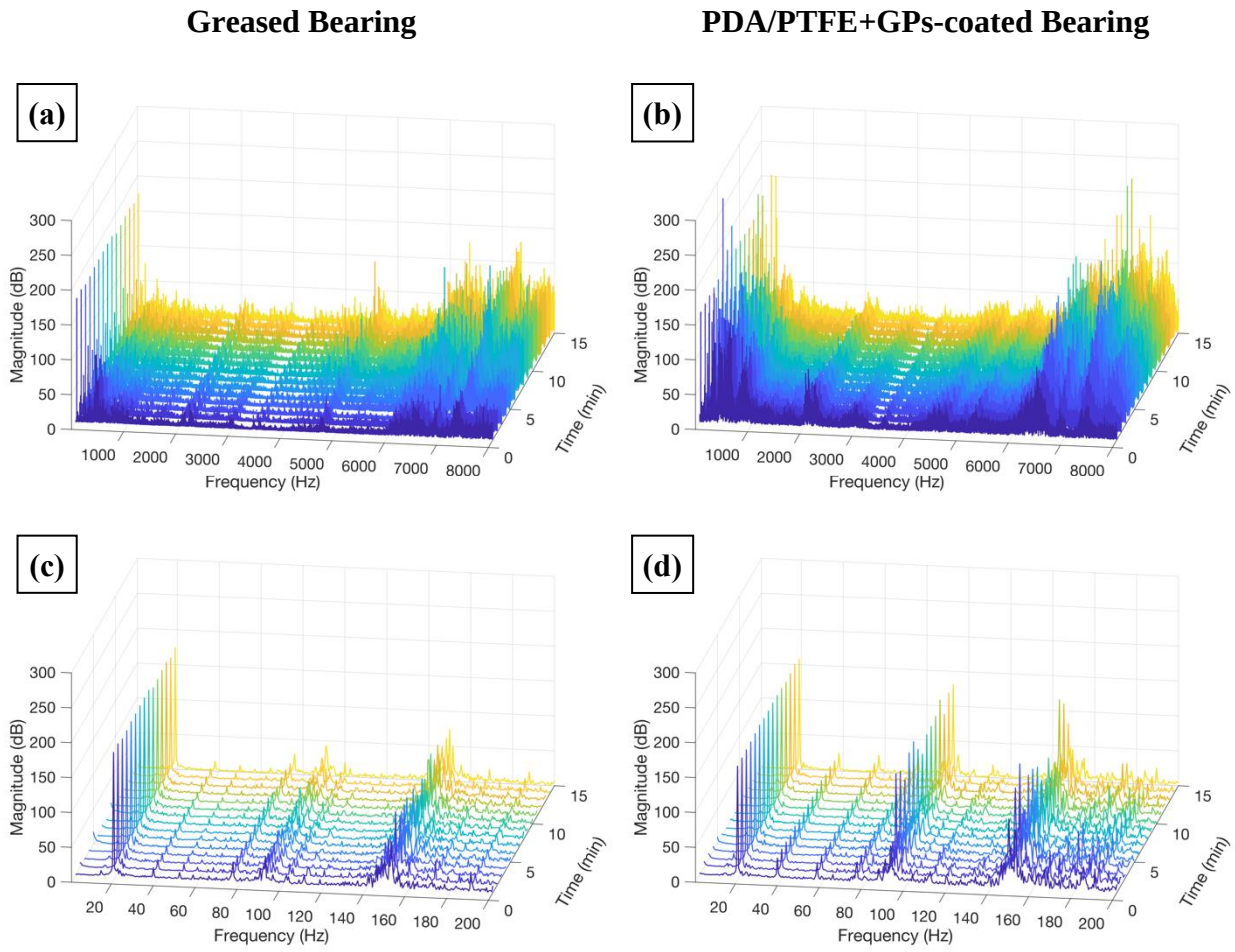

Figure 6.10. Waterfall plots of the vibration spectra during 15-min tests with the greased bearing from (a) 1-8000 Hz and (c) 1-200 Hz and the PDA/PTFE+GPs-coated bearing from (b) 1-8000 Hz and (d) 1-200 Hz.

The bearing defect characteristic frequencies were calculated based on the bearing geometry and are shown in Table 2. Unfortunately, many of the characteristic frequencies are very close to the harmonic frequencies from the rotation speed. Therefore, it is difficult to differentiate peaks corresponding to bearing faults from the rotational speed harmonic frequencies. However, the most drastic difference between the spectra for the two bearings was

between 90-95 Hz, which contains the calculated BPFI of 93.66 Hz. The BPFI physically corresponds to the frequency that a ball passes a given point of the inner race. The PDA/PTFE+GPs-coated bearing recorded a 48.0 dB peak at 92.5 Hz in the first measurement, but it increased to 142.5 dB at 2 min. This peak remained between 100-150 dB for the remainder of the test. The greased bearing showed small peaks at 91, 93, and 95 Hz, but the magnitude of the vibrations between 90-95 Hz remained below 50 dB for the entire test. The elevated peak for the coated bearing was likely caused by the balls rolling over larger fragments of coating on the inner race of the bearing.

Table 6.2. Bearings defect characteristic frequencies.

Characteristic Frequency	Value (Hz)
Speed of rotation of the inner ring - n	19
Ball Pass Frequency Outer - BPFO	58.34
Ball Pass Frequency Inner - BPFI	93.66
Ball Spin Frequency - BSF	77.36
Fundamental Train Frequency - FTF	7.29

Although the PDA/PTFE+GPs-coated bearing did not run as smoothly as the greased bearing, the coating provided sufficient lubrication throughout the test duration. In fact, the coated bearing test continued for 3 h and the vibration spectra did not show signs of coating failure or bearing damage. This is evidenced by the plots in Figure 6.11 that shows the vibration spectra for the PDA/PTFE+GPs-coated bearing after 1 min and then every 15 min for 3 h of testing. There were no significant changes to the vibration spectra throughout the 3 h test. The bearing was not disassembled for imaging so that lengthier tests can be performed on it without the risk of damaging the bearing or coating in the disassemble and reassemble process.

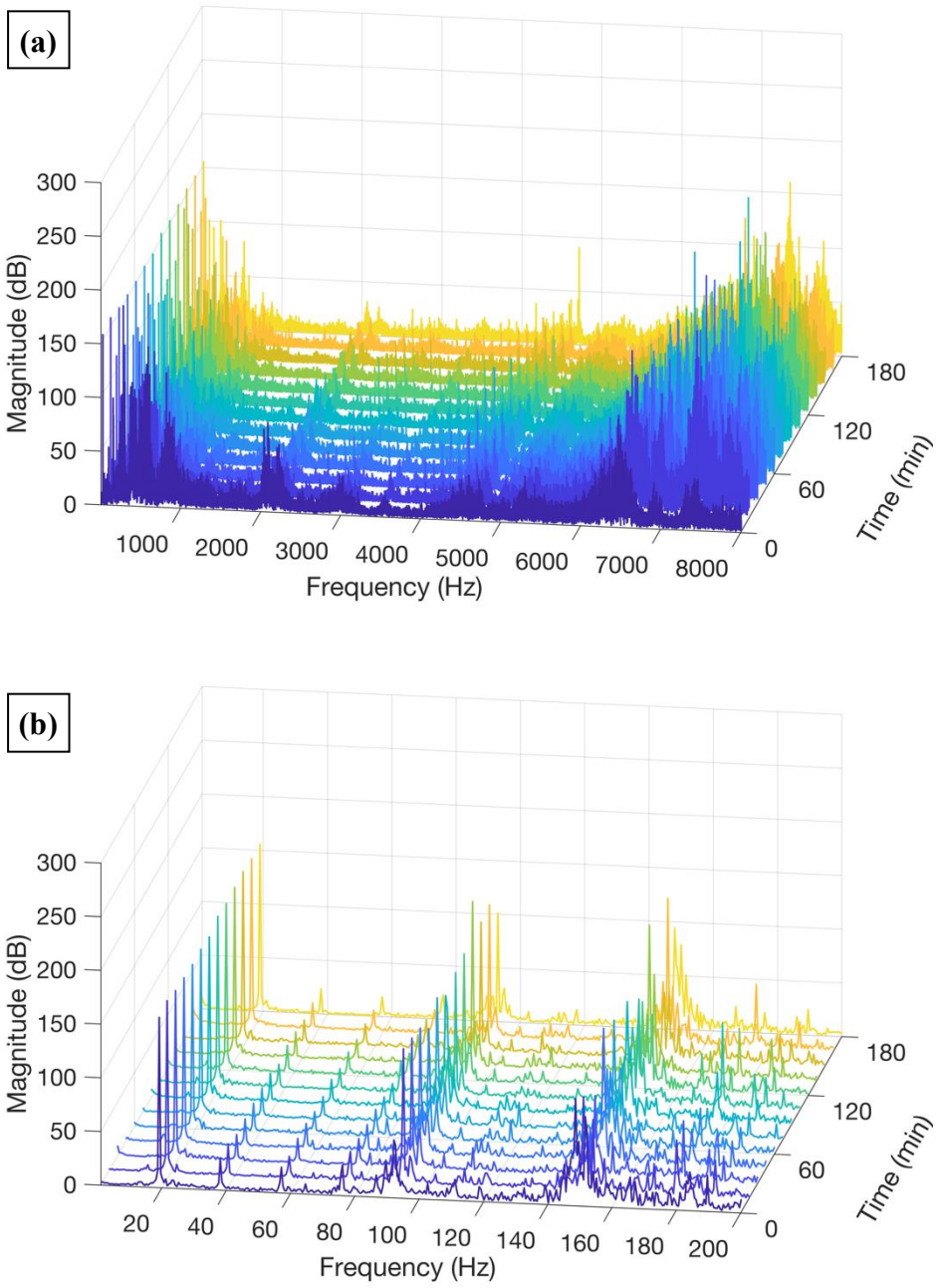

Figure 6.11. Waterfall plots of the vibration spectra during a 3-h test of the PDA/PTFE+GPs-coated bearing. Spectra are plotted from (a) 1-8000 Hz and (b) 1-200 Hz.

6.5 Sample Fabrication

R8 Hybrid 440C/Si_3N_4 bearings with polymer snap-in cages (R8 Hybrid Ceramic Bearings, Ortech Advanced Ceramics, Sacramento, CA, USA) were used for this study. The bearing material was 440C stainless steel, the rolling elements were Si_3N_4, the snap-in cages were PEEK or PTFE, and the bearings were manufactured to meet the ABEC 7 rating. The static load capacity of these bearings was 260 lb [1]. The as-received bearings were dry (no lubricant) or were packed with Kyodo SRL grease and enclosed by a rubber seal. Dry bearings with polymer snap-in cages were disassembled, the balls and races were coated with PDA/PTFE or PDA/PTFE+GPs, and then the bearings were reassembled. In this work, the term "coated bearing" refers to a bearing with PDA/PTFE- or PDA/PTFE+GPs-coated balls and races. Dry (non-lubricated), coated, and greased bearings are shown in Figure 6.2.

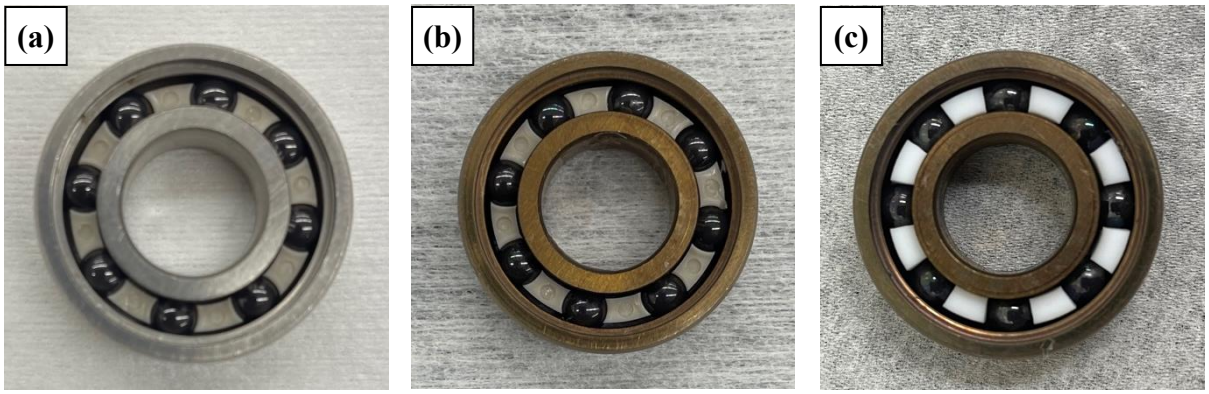

Figure 6.12. Hybrid 440C/Si_3N_4 bearings that are (a) non-lubricated (b) PDA/PTFE-coated, and (c) PDA/PTFE+GPs-coated.

6.5.1 Coating Bearings with PDA/PTFE

The bearing disassembling and reassembling processes are pictured in Figure 6.13. To disassemble the bearings, first, the snap-in cage was removed. Then, the eight balls were rolled to one side of the bearing and the bearing was placed in a vise. The outer race was compressed

radially until the elastic deformation of the outer race enabled the inner race to be removed without scratching against the balls. The separated components (inner race, outer race, and balls) were cleaned prior to coating by sonicating in baths of IPA and acetone for 10 minutes, each, and then dried with nitrogen gas.

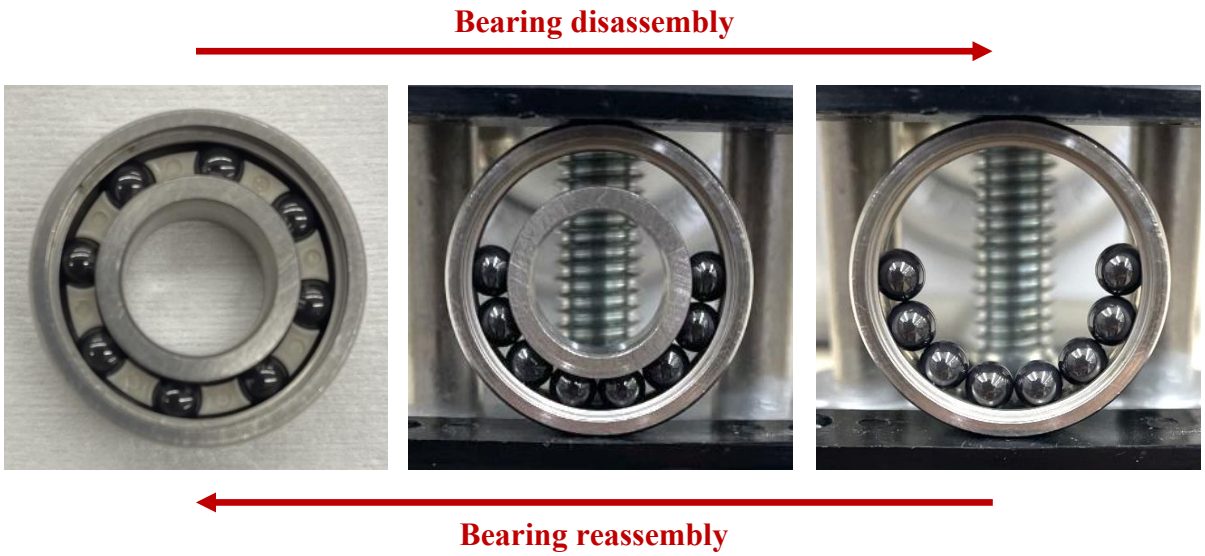

Figure 6.13. Bearing assembly and disassembly processes.

PDA was deposited on the balls and races using a heated solution of DI water in a 100 mL cylindrical glass beaker. The beaker was filled with 70 mL of DI water, which was heated to 60°C using a hotplate stirrer, buffered to a pH of 8.5 by the addition of 0.085 g of Tris base (T1503, Sigma Aldrich, St. Louis, MO, USA), and then 0.14 g of dopamine hydrochloride (H8502, Sigma Aldrich, St. Louis, MO, USA) was added. The solution was stirred using a magnetic stir bar to speed up the rate of PDA deposition, and deposition was allowed to take place for 45 minutes. During the deposition process, the inner and outer race were suspended

horizontally, concentric to the walls of the beaker, and centered over the axis of rotation of the magnetic stir bar. The balls revolved freely along the bottom edge of the beaker.

After PDA was deposited on the bearing components, they were dip-coated in an aqueous dispersion of PTFE nanoparticles (Teflon Dispersion DISP30, Fuel Cell Earth, MA, USA) or PTFE+GPs. The PTFE+GPs dispersion was produced by adding 0.25 wt% of GPs (AMLUBE 235, AML Industries, Inc., USA) to the PTFE dispersion and mixing using a planetary centrifugal mixer (Thinky Mixer AR-100, USA). The fixtures used for dip-coating the inner race, outer race, and balls are shown in Figure 6.14 (a), (b), and (c), respectively. Dip-coating was performed with an insertion and withdrawal speed of 10 mm/min and a hold time of 20 s. After dip-coating, the coated components were heat treated using a three-step process: 3 min in an oven at 120°C, 4 min in an oven at 300°C, and 4 min in a furnace at 372°C. This heat treatment process removes water and surfactant from the coating and sinters the PTFE particles.

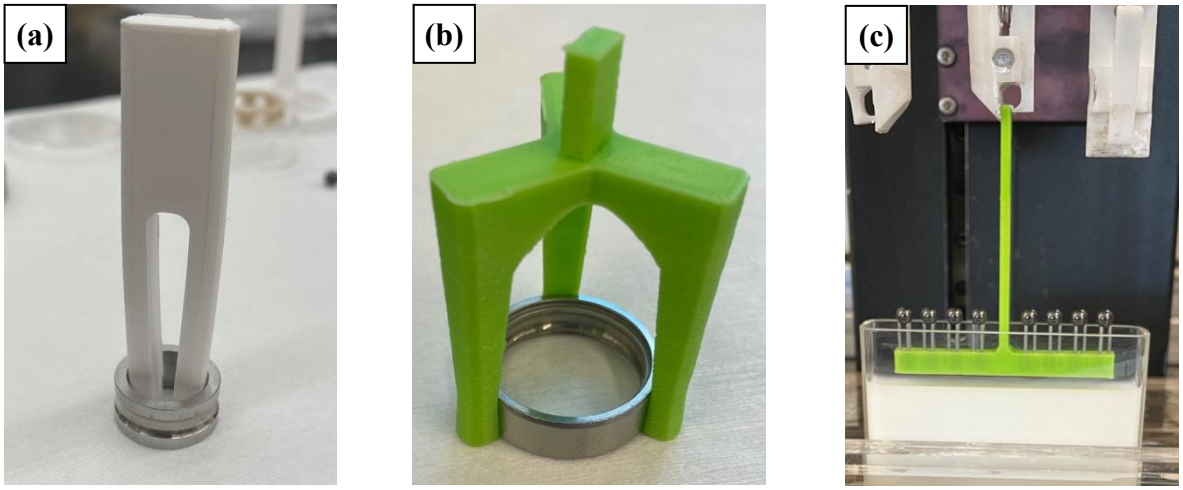

Figure 6.14. Dip-coating fixtures for the (a) inner race (b) outer race, and (c) balls.

Once the coated components cooled, the bearings were reassembled. The reassembly process is also pictured in Figure 6.13, and coated and reassembled bearings are shown in Figure 6.12 (b) and (c). The outer race was placed vertically in the vice and was compressed. Then, the balls were placed inside of the race and the inner race was dropped into position. Next, the compressive load was removed from the vise, the balls were distributed around the races by manually spacing them with the handle end of a cleaning swab, and the cage was snapped into place.

6.6 Bearing Tester Design

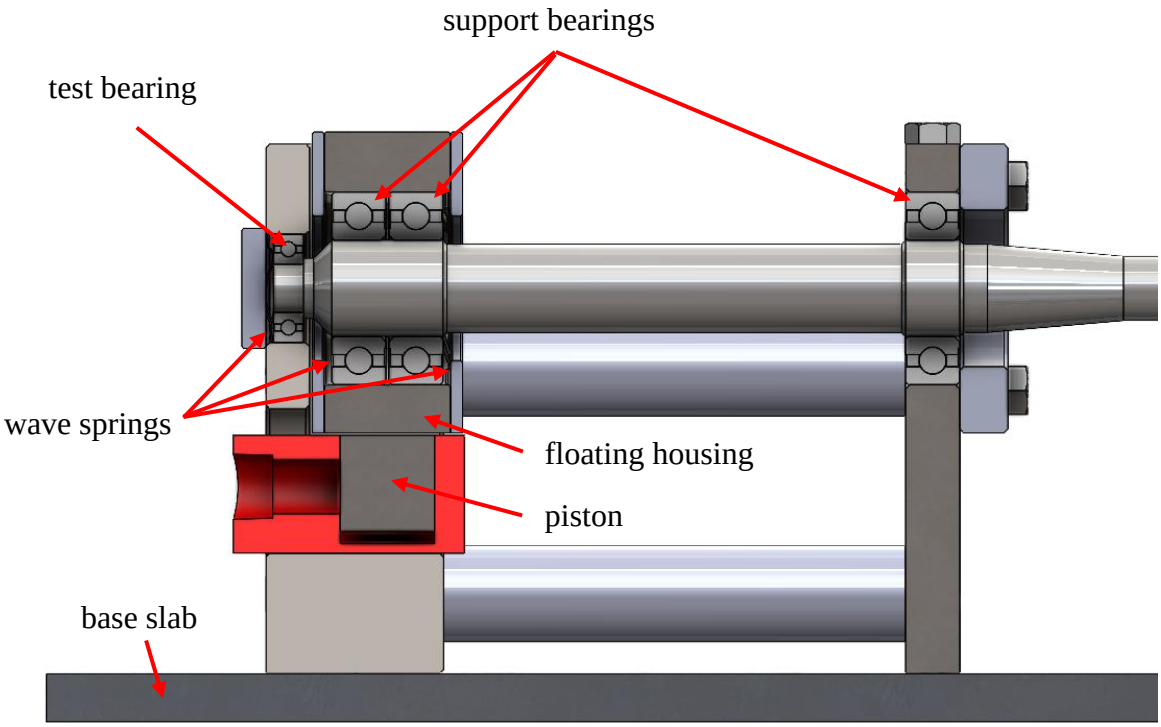

Figure 6.15. Cross-section view of the bearings on the shaft.

The shaft is supported by the test bearing and three additional support bearings as shown in Figure 6.15. The test bearing (leftmost) and the rightmost support bearing are fit into housings

that are bolted to the base slab, and the two interior support bearings are contained in a floating housing. The support bearings are 25-mm (0.984 in) bore precision ball bearings (6305-2RS, McMaster-Carr, USA) that are grease-packed and sealed. The support bearings, which are much larger than the test bearing, have a radial load capacity that is an order of magnitude greater than the radial load capacity of the R8 test bearing. A small axial preload is also applied to the test and support bearings by wave springs.

Radial load is applied to the floating housing through a flat body cylinder (HF0503, BVA Hydraulics, USA) that is connected to a hand pump (P601S, BVA Hydraulics, USA) by a hydraulic hose. A hydraulic pressure gauge displays the manually applied pressure, P, in psi. The force F, in lbf, applied by the flat body cylinder to the floating bearing housing is determined by multiplying the applied pressure by the cylinder effective area (A_{eff} =1.10 in^2).

$$F = P \times A_{eff} \quad \text{(Eq. 6.1)}$$

The force, F, was used to load the shaft and bearings. However, the radial load on the test bearing, R_1, is the load of greatest interest, so the relationship between F and R_1 was determined. The force applied by the piston of the flat body cylinder to the floating housing, F, was applied to the shaft through the support bearings in the floating housing. A free-body diagram of the shaft is shown in Figure 6.16. The location of the applied load was approximated as the center of the floating housing. There were two vertical reaction forces on the shaft: R_1, the reaction force from the test bearing, and R_2, the reaction force from the rightmost support bearing. The

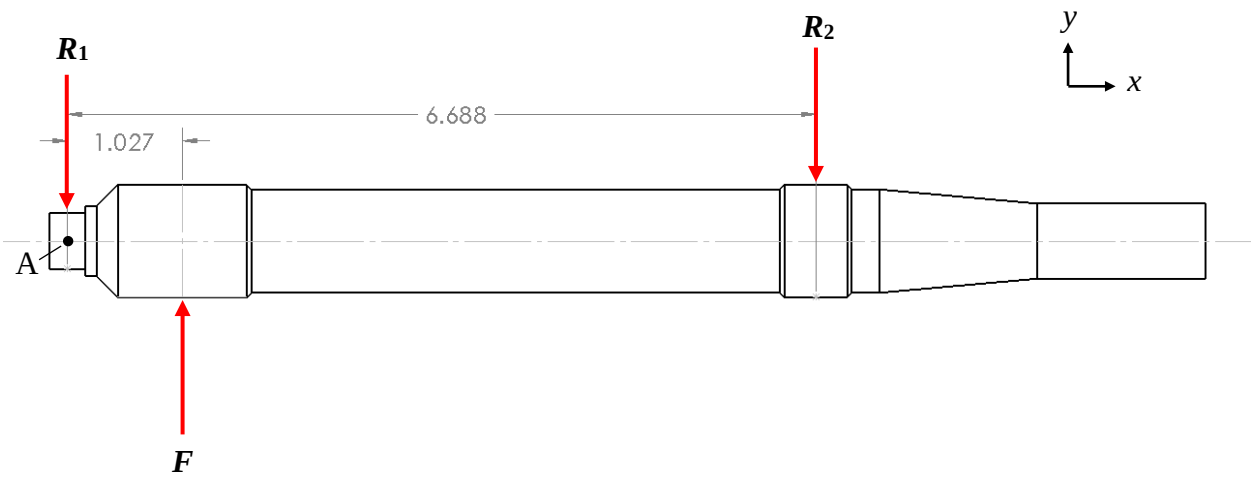

Figure 6.16. Free body diagram of the shaft with applied load *F*, reaction forces R_1 and R_2, and point A. All dimensions are in inches.

locations of R_1 and R_2 were approximated as the center of the test bearing and rightmost support bearing, respectively.

R_1 was determined from static analysis of the shaft based on the free-body diagram shown in Figure 6.16. A linear system of equations was developed from the summation of forces in the *y*-direction and the summation of moments about point A.

$$\sum F_y = 0 = -R_1 + F - R_2 \qquad \text{(Eq. 6.2)}$$

$$\sum M_A = 0 = 1.027F - 6.688R_2 \qquad \text{(Eq. 6.3)}$$

Solving Eq. 6.2 and 6.3 simultaneously for a unit applied load of $F = 1$ yields $R_1 = 0.84644$ and $R_2 = 0.15356$. Therefore, the relationship between *F* and R_1 is

$$F = \frac{R_1}{0.84644} \qquad \text{(Eq. 6.3)}$$

and substituting Eq. 6.3 into Eq. 6.1 yields a relationship between the pressure applied by the hand pump, *P* (psi), and the radial load on the test bearing, R_1 (lbf).

$$R_1 = 0.931084P \qquad \text{(Eq. 6.4)}$$

Therefore, a pressure of 250 psi applied to the flat body cylinder corresponds to a radial load on the test bearing of approximately 230 lb.

The force application system was redesigned before the second round of testing so that the radial load applied to the test bearing could be controlled with greater precision. The redesigned system replaces the hand pump and pressure gauge, but still uses the flat body cylinder to apply load to the bearings. The new system is shown in Figure 6.17. It uses an air-over-hydraulic conversion to convert applied air pressure to the pressure in the hydraulic hose of the flat body cylinder. Figure 6.17a shows an annotated photograph of the air-over-hydraulic conversion, and Figure 6.17b shows a cross-sectioned view of the system model. The air cylinder

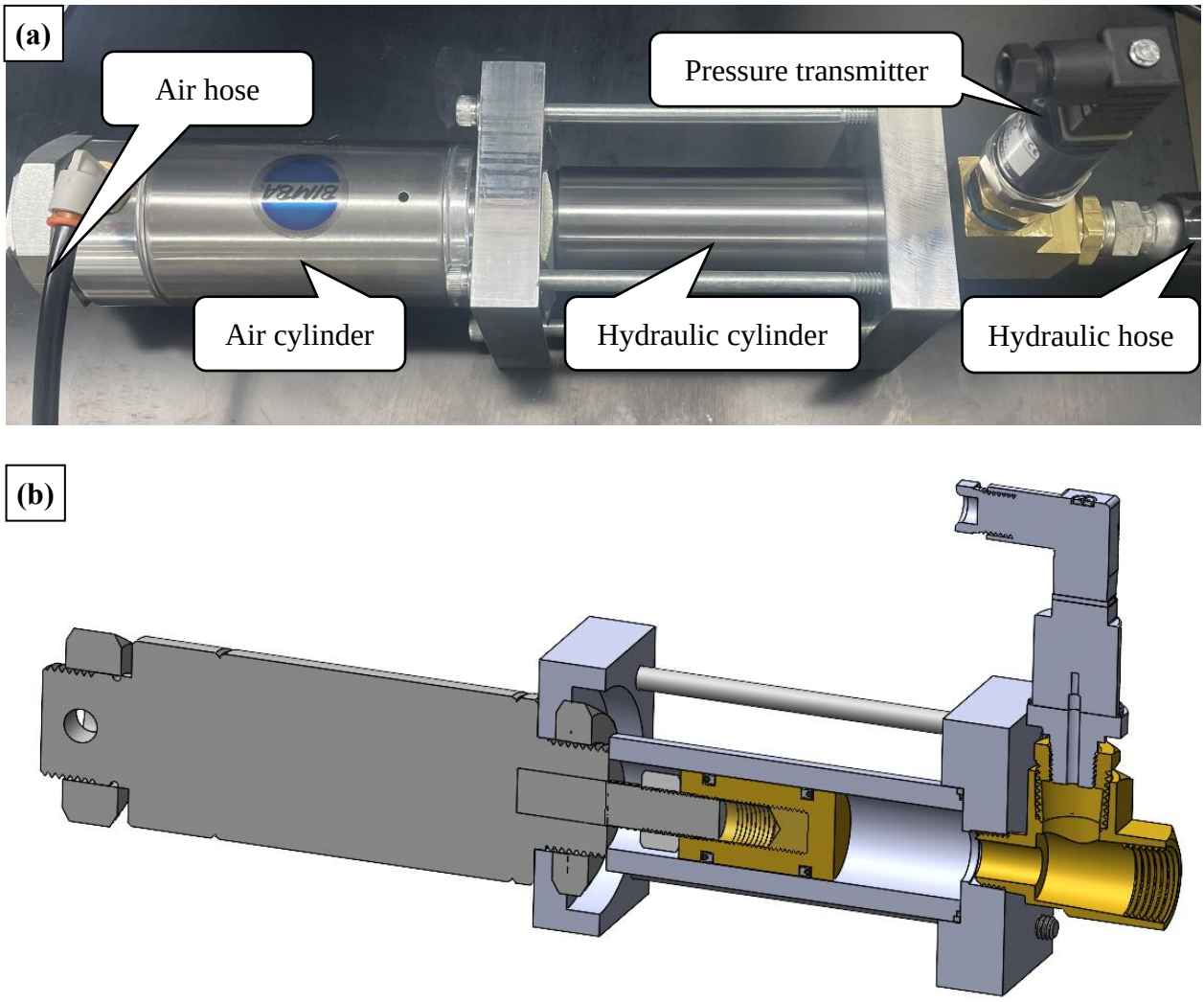

Figure 6.17. (a) Annotated photograph of the air-over-hydraulic conversion system and (b) cross-sectioned view of the CAD model.

converts the air pressure to a linear force in a piston rod. The hydraulic cylinder converts the force from the piston rod to hydraulic pressure.

The force applied to the bearings is adjusted by controlling the air pressure using a precision pressure regulator. The air pressure can be controlled by the regulator at ±0.1% accuracy, so it provides substantially better control of the applied load compared to the hand pump and pressure gauge used in the first design. Additionally, the pressure in the hydraulic line (pressure applied to the flat body cylinder) is measured by a pressure transmitter. This enables the pressure (and resulting force on the bearings) to be monitored remotely and recorded throughout testing.

An accelerometer was mounted on the top of the test bearing housing (Figure 6.18) and was used to measure vibration during testing. The vibration data was processed and recorded using LabView software. The vibrations were sampled for 2 s at a frequency of 16384 Hz, or 2^{14} Hz, to facilitate FFT analysis. The acceleration waveform in the time domain was transformed to

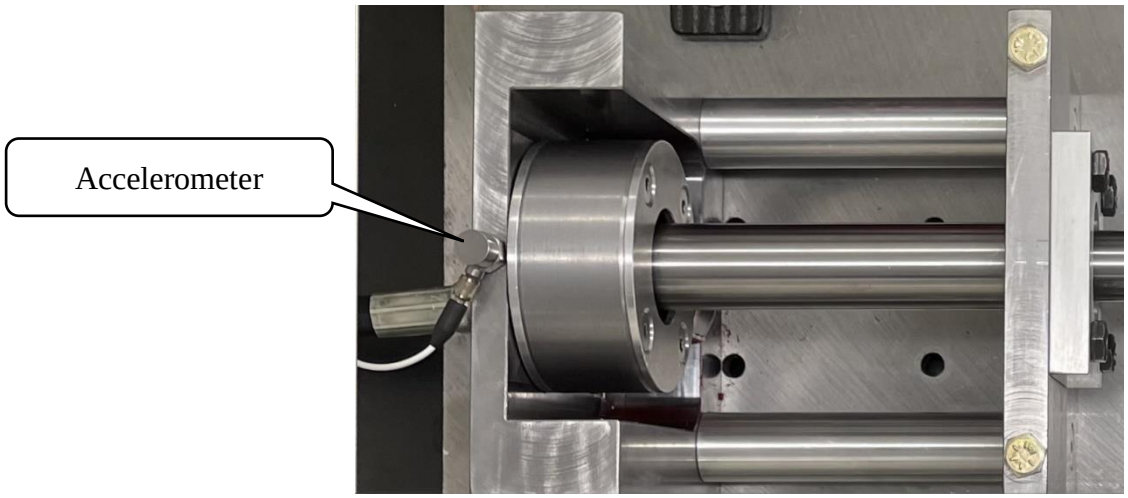

Figure 6.18. The accelerometer mounted on top of the test bearing housing.

a frequency domain spectrum using FFT with first and last frequency lines of 0 and 8191.5 Hz, respectively, and a frequency resolution of 0.5 Hz.

6.7 Conclusions

This study showed that PDA/PTFE and PDA/PTFE+GPs coatings have the potential to be applied as ball bearing lubricants for applications that are not suited for oil or grease lubrication. The coatings rely on transfer film formation to lubricate the contact between bearing components. The coatings can be deformed, worn, and displaced during bearing operation, but it continues to provide lubrication by developing transfer films and redepositing at different contact points in the bearing. This is distinct from the behavior of hard solid lubricant coatings where coating damage leads to lubrication failure. Additionally, hard solid lubricant coatings require special care for their effect on the dimensions and tolerances in a bearing. The soft PDA/PTFE coatings do not require as careful attention because the coatings accommodate the changes by deforming, compacting, and utilizing a very thin layer at the coating/substrate interface to lubricate contact. When bearings are lubricated with grease, they require shields or seals to contain the grease and protect it from outside contaminants. However, the PDA/PTFE coatings are self-containing, the non-stick nature of PTFE hinders debris accumulation, and its hydrophobicity repels moisture. Additionally, if coating fragments are ejected from the bearing, they are not as harmful of contaminants to the surroundings as grease or oil.

The promising initial results presented here suggest that PDA/PTFE-coated ball bearings should be studied further. The present work did not explore the life and limitations of the coated bearings. This is a crucial next step if PDA/PTFE-coated bearings are to be implemented in real

applications. Furthermore, if PDA/PTFE-coated 440C/Si_3N_4 hybrid bearings are shown to have sufficient lubrication life, then similar tests should be performed on hybrid 60NiTi/Si_3N_4 bearings for 60NiTi space applications [1-2,4,17].

6.8 References

[1] C. DellaCorte and S. A. Howard, "Performance of Small Bore 60NiTi Hybrid Ball Bearings: Preliminary Life Test Results," in *2016 STLE Tribology Frontiers Conference*, 2016, no. GRC-E-DAA-TN34975.

[2] C. DellaCorte, "Ni-Ti Next Generation Bearings for Space Applications," in *Schaeffler International Bearing Meeting*, 2018, no. GRC-E-DAA-TN45947.

[3] C. DellaCorte, "Novel super-elastic materials for advanced bearing applications," in *Advances in Science and Technology*, 2014, vol. 89, pp. 1–9.

[4] C. DellaCorte, "NiTi Alloys: New Materials that enable Shockproof, Corrosion Immune Bearings," in *Society of Tribologists and Lubrication Engineers (STLE) Section Meeting*, 2017, no. GRC-E-DAA-TN38532.

[5] C. DellaCorte, L. E. , I. Moore, J. S. Clifton, L. E. , I. Moore, and J. S. Clifton, "Static Indentation Load Capacity of the Superelastic 60NiTi for Rolling Element Bearings." 2012.

[6] C. DellaCorte, M. K. Stanford, and T. R. Jett, "Rolling contact fatigue of superelastic intermetallic materials (SIM) for use as resilient corrosion resistant bearings," *Tribol Lett*, vol. 57, no. 3, pp. 1–10, 2015.

[7] C. DellaCorte, S. A. Howard, F. Thomas, and M. K. Stanford, "Microstructural and material quality effects on rolling contact fatigue of highly elastic intermetallic NiTi Ball bearings," 2017.

[8] C. DellaCorte and W. A. Wozniak, "Design and Manufacturing Considerations for Shockproof and Corrosion-Immune Superelastic Nickel-Titanium Bearings for a Space Station Application," 2012.

[9] C. DellaCorte and M. Jefferson, "60NiTi Intermetallic Material Evaluation for Lightweight and Corrosion Resistant Spherical Sliding Bearings for Aerospace Applications, Report on NASA-Kamatics SAA3-1288," in *Tribology Frontiers Conference*, 2015, no. E-19059.

[10] C. Miller and M. Zou, "Repetitive nanoindenter scratch testing of polydopamine/polytetrafluoroethylene-based thin coatings," *Surf Coat Technol*, vol. 451, p. 129042, 2022.

[11] C. Miller and M. Zou, “Microscale friction and deformation behavior of polydopamine/polytetrafluoroethylene-coated 60NiTi from nanoscratch tests,” *Thin Solid Films*, vol. 743, p. 139079, 2022.

[12] D. Choudhury, C. Miller, and M. Zou, “Tribological performance of PDA/PTFE+ graphite particle coatings on 60NiTi,” *Appl Surf Sci*, vol. 527, p. 146731, 2020.

[13] C. Miller, D. Choudhury, and M. Zou, “The Effects of surface roughness on the durability of polydopamine/PTFE solid lubricant coatings on NiTiNOL 60,” *Tribology Transactions*, vol. 62, no. 5, pp. 919–929, 2019.

[14] D. Choudhury, C. Miller, N. Harris, and M. Zou, “The effect of coating thickness on the tribological properties of polydopamine/PTFE+ graphite particle coatings on 60NiTi,” *Surf Coat Technol*, vol. 420, p. 127320, 2021.

[15] L. C. K. Reuben and D. Mba, “Bearing time-to-failure estimation using spectral analysis features,” *Struct Health Monit*, vol. 13, no. 2, pp. 219–230, 2014.

[16] S. Beckford, J. Cai, R. A. Fleming, and M. Zou, “The effects of graphite filler on the tribological properties of polydopamine/PTFE coatings,” *Tribol Lett*, vol. 64, no. 3, pp. 1–10, 2016.

[17] C. DellaCorte, R. D. Noebe, M. Stanford, and S. A. Padula, “Resilient and corrosion-proof rolling element bearings made from superelastic Ni-Ti alloys for aerospace mechanism applications,” 2011.

CHAPTER 7

CONCLUSIONS AND RECOMMENDATIONS

7.1 Conclusions

The overall objective of this dissertation was to further the understanding of the tribological behavior and mechanical properties of 60NiTi and to develop PTFE-based solid lubricant coatings for use with 60NiTi in bearing and gear applications. This objective was accomplished through the various studies contained in this work, and the results are summarized as follows.

The mechanical properties of 60NiTi and its microconstituents were studied by nanoindentation. The elastic modulus and hardness of hardened 60NiTi were measured to be 89.7 ± 3.9 GPa and 8.1 ± 0.4 GPa, respectively. Low-load and selective nanoindentations on the NiTi + Ni_4Ti_3 region and globular Ni_3Ti precipitates revealed significant differences in the mechanical properties of these microconstituents. The NiTi + Ni_4Ti_3 region was found to have an elastic modulus of 99.9 ± 8.3 GPa and a hardness of 8.3 ± 0.9 GPa, while the Ni_3Ti precipitates were measured to have a much higher elastic modulus of 262 ± 33 GPa and hardness of 13.1 ± 1.7 GPa. These results showed that the elastic modulus and hardness of bulk 60NiTi resembles the properties of the NiTi + Ni_4Ti_3 regions in its microstructure. The hardness of 60NiTi drops when Ni_4Ti_3 precipitates decompose into Ni-rich precipitates. This drop in hardness occurs despite the Ni_3Ti phase being significantly harder than bulk 60NiTi. Instead, the bulk hardness is reduced because the formation of Ni-rich phases degrades the hardening effect provided by the nanoscale Ni_4Ti_3 precipitates in the NiTi + Ni_4Ti_3 region.

The tribological behavior of 60NiTi and 60NiTi coated with PDA/PTFE were studied by linear reciprocating ball-on-disk tribometer tests with a Si_3N_4 ball. Tests on polished bare 60NiTi measured a COF of 0.731. Coating 60NiTi with PDA/PTFE was found to reduce the COF by over 85% and slowed down the wear of 60NiTi for thousands of cycles during accelerated tests. Rougher substrate surface finishes were found to increase coating durability over 30 times compared to a polished substrate, and valley-dominant roughness resulted in further improvement to the coating durability. This study demonstrated the effectiveness of PDA/PTFE solid lubricant coatings on 60NiTi.

Nanoindenter scratch tests were performed on 60NiTi, 60NiTi/PDA, and 60NiTi/PDA/PTFE to further investigate the coating behavior. The COF, deformation, and failure mechanisms were studied by nanoindenter scratches with a spheroconical diamond tip and at various constant normal loads. Scratches at loads up to 1000 μN caused the coating to deform plastically and form a more uniform and compressed layer. Therefore, the large initial wear depth reported in previous macro-tribology studies could partially be due to coating compaction rather than plowing and global removal. The PDA/PTFE coating formed tears during scratches at 2000 μN, and at scratch loads of 3000 μN and greater, the coating tore, the substrate was exposed along a majority of the scratch length, and large amounts of build-up occurred at the end of the scratches. This severe PDA/PTFE coating failure occurred at the same scratch loads that caused the removal of the PDA aggregates during scratches on 60NiTi/PDA.

The SEM images of the nanoindenter scratches on 60NiTi/PDA/PTFE showed interesting changes in the coating microstructure. The originally porous coating was compacted by the

scratches and formed a more uniform layer. Repetitive nanoindenter scratch tests were used to investigate the mechanical and tribological behavior of this compacted layer. The study showed that the compacted coating had lower COF and was more resistant to deformation than the originally porous coating. Ten repetitive scratches were performed on PDA/PTFE coating at various loads so that the progression of coating failure could be observed. Failure of the compacted coating during repetitive scratches originated from tears that formed behind the indenter tip due to large tensile stresses in the coating. However, this mechanism was mitigated by increasing the substrate roughness and incorporating GPs in the PTFE layer.

Roughening the substrate provided resistance to coating delamination and global removal due to mechanical interlocking between the coating and the grooves of the substrate roughness. The mechanical interlocking reduced the tensile stresses in the coating, and adding GPs enhanced PTFE particle cohesion. The improved coating cohesion strengthened the interlocking effect with the substrate roughened and provided higher resistance to tears within the PTFE layer. When PDA/PTFE with GPs was deposited on a rough substrate, it enabled the coating to compact and stabilize as a 200-300 nm thick durable layer. Therefore, PDA/PTFE + 0.25 wt% GPs on a substrate with a valley-dominated, roughened surface shows promising potential as a solid lubricant coating for 60NiTi in applications where repetitious high-pressure sliding is encountered.

A feasibility study was performed to evaluate PDA/PTFE-based coatings as a ball-bearing lubricant. Methods were developed to apply PDA/PTFE and PDA/PTFE+GPs coatings to the balls and races of hybrid deep groove ball bearings. A custom bearing tester was designed,

built, and used to test the solid-lubricated bearings with controlled speed and radial load. The initial results showed promising potential for PDA/PTFE- and PDA/PTFE+GPs-coated ball bearings, and further study is warranted.

7.2 Recommendations for Future Work

The results from the nanomechanical property characterizations of 60NiTi and observations from tribological tests have sparked potential explanations for the high wear rate of 60NiTi in dry sliding conditions. These theories could be explored in future studies. First, if displaced, the large hard Ni_3Ti precipitates may act as abrasive particles that accelerate the wear of 60NiTi. Also, significant amounts of Ni-rich transfer materials have been observed on the chrome steel counterface balls after ball-on-disk testing on 60NiTi plates. During unlubricated sliding of 60NiTi, the metastable nanoscale Ni_4Ti_3 precipitates may decompose into Ni-rich phases, and the hardness of 60NiTi could be locally reduced. Therefore, the wear rate is higher than expected. This hypothesis could be tested by elemental analysis of the 60NiTi wear tracks and the Ni-rich transfer material. Additionally, nanoindentations could be performed inside of the wear tracks of 60NiTi to measure if the mechanical properties change after unlubricated sliding.

PTFE coatings show creep during nanoindentation tests and demonstrates viscoelastic behavior. Therefore, new nanoindentation studies could be performed to characterize the dynamic mechanical behavior of the coatings. This could be done using the nanoscale dynamic mechanical analysis (nanoDMA) mode of the nanoindenter instead of the quasi-static measurement mode. The nanoDMA tests could provide measurements for the stiffness, damping,

and storage/loss modulus of the PTFE coatings. This data would be useful for developing an accurate mathematical model for the behavior PTFE coatings.

PDA/PTFE-based coatings have been developed, characterized, and incrementally improved extensively over the last decade. Therefore, the remaining recommendations for future work focus on evaluating and improving these coatings for ball bearing applications.

The PDA/PTFE- and PDA/PTFE+GPs-coated ball bearings showed promising behavior during initial tests using the bearing tester, and further tests should be performed. Bearing temperature and bearing torque measurements would provide more insight into the effectiveness of the solid lubricant coatings. The bearing tester is currently outfitted with three K-type thermocouples that can measure and record temperature data. The temperature of the test bearing is monitored by inserting one of these thermocouples into a small hole in the housing of the test bearing. The mounting of the thermocouple near the test bearing could be improved. Coated bearings could also be tested for longer durations to determine the lubricant life. However, the bearing tester should be improved if this type of testing is performed.

The radial load applied to the test bearing needs to be controlled with greater accuracy and precision. The force application system was changed from the hand pump to a pneumatic system that uses an air cylinder to achieve an air-over-hydraulic conversion. The force on the bearing is controlled by adjusting the air pressure regulator upstream of the air cylinder. A pressure transmitter was installed on the hydraulic line so that the pressure in the hydraulic fluid can be measured with greater precision than the original pressure gauge, and the applied pressure

can be recorded using the data acquisition system. Force is still applied to the bearings through the flat body cylinder. The pressure in the hydraulic fluid varies during testing despite the air pressure remaining constant. Friction in the seal of the flat body cylinder may be the primary cause of this issue. This design should be modified to improve control of the radial load applied to the test bearing.

The data acquisition system of the bearing test rig also needs to be improved before longer-duration bearing tests are performed. The LabView software periodically crashes, and data acquisition is stopped. Therefore, the tests must be frequently monitored to ensure that the data is logged.

The durability of PDA/PTFE-based coatings on ball bearings could also be improved by modifying the surfaces of the races. The inner and outer races of the bearings that were coated and tested in this study have polished surfaces with polishing lines parallel to the rolling direction. The coating would likely be more durable if the surfaces of the bearing races were polished so that the balls roll perpendicular to the polishing lines. Also, the PDA/PTFE coating does not adhere well to the highly polished Si_3N_4 balls. Although the coating is quickly removed from the balls, transfer films develop on the balls as the bearing runs. Therefore, it may not be necessary to coat the bearing balls. Bearings could be tested that only have coated races. The transfer films still might develop on the balls, and the coated bearing may run with less vibration due to fewer coating fragments creating bumps on the races. Furthermore, this would simplify the procedures for lubricating a ball bearing with PDA/PTFE-based solid lubricant coatings.

PDA/PTFE-coated ball bearings may be applicable in ambient conditions. However, traditional oil or grease lubrication is likely the favorable approach because it is easier to apply, and it is a more cost-effective approach. PDA/PTFE-coated ball bearings should be developed for challenging design conditions that exclude the use of oil or grease lubrication. Therefore, it would be useful to test PDA/PTFE-coated bearings in various conditions such as vacuum, high humidity, high temperature, or in the presence of severe contaminants.